Politecnico di Milano

School of Industrial and Information Engineering

Master of Science in Mathematical Engineering

Mixed Finite Element Method and Preconditioning for 3D-1D Problems

Advisor:

Prof. Paolo ZUNINO

Co-Advisor:

Dr. Daniele CERRONI

Master Thesis of:

Fannie Maria Gerosa

Matr. 858881

Academic Year 2016-2017

A mia nonna
Virginia.

Sommario

Questo lavoro presenta un modello multi-fisica per la microcircolazione che descrive l'interazione del plasma con i globuli rossi. Il modello tiene conto degli effetti fondamentali che caratterizzano la microcircolazione, come l'effetto Fahraeus-Lindqvist ed il plasma skimming. I capillari sono considerati come una sorgente monodimensionale concentrata sull'asse del vaso con configurazione arbitraria, possibilmente curva. Questo modello descrive la variazione di portata e velocità come formulazione differenziale locale della conservazione della massa e del momento lungo l'asse del capillare. La seconda parte di questo lavoro mira a trovare una nuova strategia per risolvere il sistema derivante dalla discretizzazione ad elementi finiti, utilizzando un metodo GMRES. Il risolutore iterativo viene accelerato da un precondizionatore a blocchi basato sul complemento di Schur del problema in pressione. Pertanto, vengono derivati diversi precondizionatori per il problema nel solo vaso, nel tessuto e per quello globale non accoppiato. Vengono considerate due opzioni per precondizionare i residui: una fattorizzazione LU incompleta ed un metodo Multigrid Algebrico. Il secondo approccio richiede l'uso di una libreria, chiamata SAMG, sviluppata presso il Fraunhofer Institute for Algorithms and Scientific Computing (SCAI), che contiene i risolutori Multigrid Algebrici utilizzati.

Abstract

This work presents a multi-physics model for microcirculation that describes the interaction of plasma with red blood cells. The model takes into account of fundamental effects characterizing the microcirculation, such as the Fahraeus-Lindqvist effect and plasma skimming. The capillaries are considered as one-dimensional concentrated source with arbitrary configuration, possibly curved. This model describes the variation of flow rate and velocity as local differential formulation of mass and momentum conservation along the capillary axis. The second part of this work aims to find a new iterative strategy to solve the system arising from the finite element discretization, using a GMRES method. The iterative solver is accelerated by a block preconditioner based on the Schur complements of the pressure problems. Therefore, different preconditioners for the stand alone vessel, tissue and uncoupled problem are derived. Two options are considered to solve the residual system: an Incomplete LU factorization and an Algebraic Multigrid Method. The second approach required the use of a library, called SAMG, developed at the Fraunhofer Institute for Algorithms and Scientific Computing (SCAI), which contains the Algebraic Multigrid solver used.

Contents

List of Figures

List of Tables

Introduction

The objective of this thesis was to reinforce an already existing multi-physics model for microcirculation that describes the interaction of plasma with red blood cells.

We consider a domain Ω that is composed by two parts, Ω_v and Ω_t, the capillary bed and the tissue interstitium, respectively. Assuming that the capillaries can be described as cylindrical vessels, we denote with Γ the outer surface of Ω_v, with R its radius and with Λ the centerline of the capillary network, as showed in figure 1. The vessel radius R is generally changing in the network. The innovation in the model is that the capillaries, already represented as one-dimensional channels with rectilinear configuration, now are considered with arbitrary, possibly curved configuration.

The model takes into account of fundamental effects characterizing the microcirculation, such as the Fahraeus-Lindqvist effect and plasma skimming. Besides these features, the model describes the interaction of capillaries with the surrounding tissue, and in particular the interaction of capillary transmural flow with the surrounding interstitial pressure.

The latter two features rely on the unique ability of the model to account for variations of flow rate and velocity along the axis of the capillary, according to a local (differential) formulation of mass and momentum conservation. Indeed, the

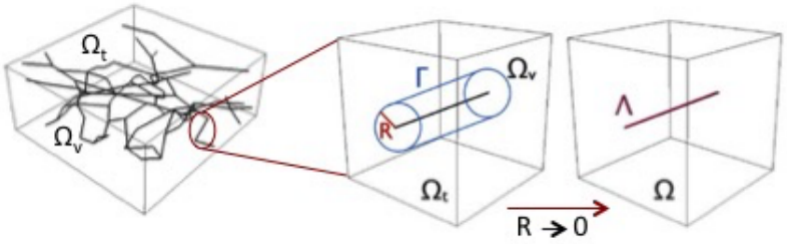

Figure 1

model stands on a solid mathematical foundation, which is also addressed in this work. In particular, we present the model derivation in a mixed form, variational formulation and approximation using Mixed Finite Element Method.

The second part of this work is focused on improve the computational effort, introducing a preconditioned iterative method for the resolution of the system obtained from the finite element discretization. This system has the classical form of a saddle-point problem that we are going to use to provide an efficient solution strategy. Some difficulties arise from the coupling term between the 3D-1D geometry, which is going to increase the complexity of the problem, extending the number of non-null term of our discrete approximation.

Figure 2 contains a compact description of all the strategies considered. Until this moment the method used to find the solution was a direct solver, namely *SuperLU*, which is based on the LU decomposition.
Our objective is to find a faster method to solve the algebraic problem.

We implemented a block-diagonal preconditioner, using the theory described in [3] and [13], based on Jacoby method, for the A-block part, and Schur discretization. Even if we can show that the Schur complement S is symmetric positive definite, the inverse is still computationally onerous to compute. The two approaches studied are Incomplete LU and Algebraic Multigrid Method. The explanation of what they are and how they will be used, is discussed in Chapter 3.

Since we know that multigrid methods work well for elliptic-type problem and we have available an Algebraic Multigrid Methods library, called SAMG, Multigrid Methods are the natural direction to take after the discretization of the Schur complement.

As we will see, the preconditioner is constructed differently with respect to every situation analyzed. Different preconditioners for the stand alone vessel, tissue and uncoupled problem are derived. For the coupled problem, however, a different strategy has to be described.

Finally, we conclude this work with a comparative study on the importance of the Fahraeus-Lindqvist, plasma skimming and capillary leakage effect on the distribution of flow in a microvascular network. Exploring the effects of both curvature and variation of radius on simple geometry. Subsequently, we have assessed the performance of our new preconditioner, both on trivial and more complex geometries.

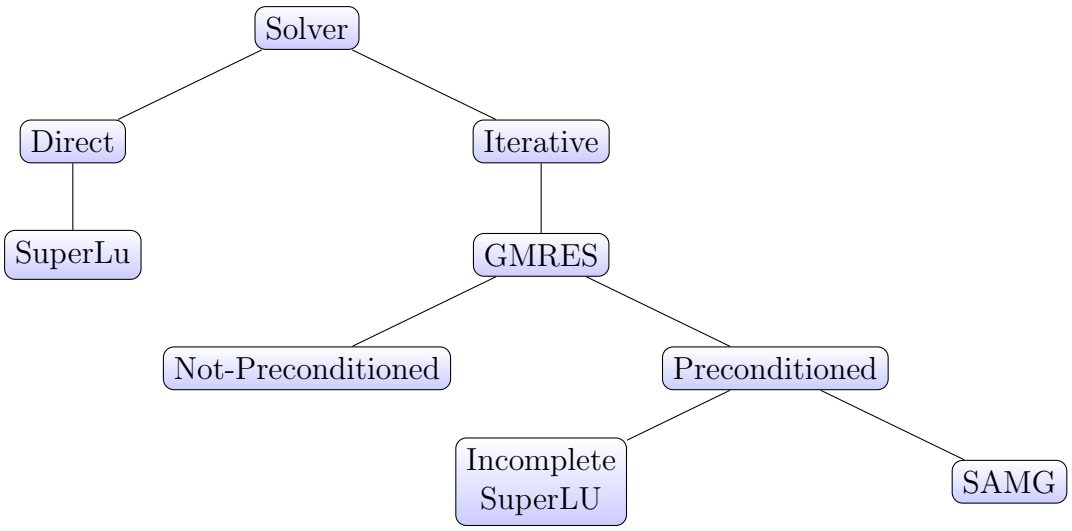

Figure 2

The outline of this work is the following. Chapter 1 contains the derivation of our model for fluid exchange between interstitium and vessel, and the hematocrit variation, respectively.

In Chapter 2 we remind some of the fundamental aspects of Saddle-point problem and algebraic multigrid method, which as already introduce, it will be used as preconditioner for the GMRES method.

Then, in Chapter 3 we will describe in detail how we construct our preconditioner, distinguishing between coupled and uncoupled cases, since as we will see, we are going to adopt two different strategies. For the uncoupled case a monolithic diagonal preconditioner will be derived, while for the coupled case an external Gauss-Seidel cycle it is used.

Chapter 4 and 5 contain the results of our simulations. The first one will be focused on discussing the effect of curvature and the application of our model to a realistic complex network of capillaries. Chapter 5 will discuss about the performance of our different solution strategies. Finally, details about the code are given in Appendix A.

Chapter 1

Mathematical Model for Fluid Dynamics and Hematocrit Transport

1.1 Fluid dynamics Model set up

We define a mathematical model for fluid transport in a permeable biological tissue perfused by a capillary network. We consider a domain Ω that is composed by two parts, Ω_v and Ω_t, the capillary bed and the tissue interstitium, respectively. Assuming that the capillaries can be described as cylindrical vessels, we denote with Γ the outer surface of Ω_v, with R its radius and with Λ the centerline of the capillary network, as showed in figure 1.1. The vessel radius R is generally changing in the network. Any physical quantity of interest, such as the blood pressure p and the blood velocity u, is a function of space (being $\mathbf{x} \in \Omega$ the spatial coordinates). We consider steady-state flow conditions, as a result all variables are independent of time. We can state this hypothesis because, since we are working on micro circulation, fluctuations of the blood pressure due to the heartbeat are negligible, namely the Womersley numbers at the level of capillary circulation are negligible. We consider the interstitial volume Ω_t as an isotropic porous medium, where the relation between velocity and pressure can be described by the Darcy's law.

Ignoring the inertial and body forces we have:

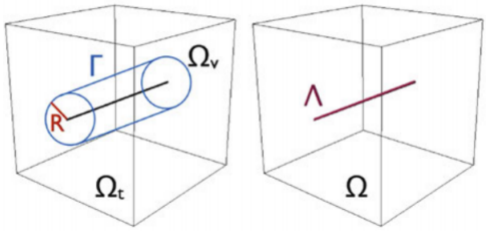

Figure 1.1: On the left, the interstitial tissue slab with one embedded capillary; on the right, the reduction from 3D to 1D description of the capillary vessel.

$$\mathbf{u}_t = -\frac{1}{\mu_t} K \nabla p_t \tag{1.1}$$

where $\mathbf{u}_t$, μ_t, p_t denote the averaged filtration velocity, the fluid viscosity and the fluid pressure, respectively, and K represent the hydraulic permeability tensor. , μ_t is the fluid viscosity in the tissue. We recall that in the simple isotropic case the permeability tensor is given bu $K = k\,\mathbb{I}$, where k is the scalar permeability and $\mathbb{I}$ the identity tensor, this will be our case. We assume that the fluid in the interstitial space is equivalent to blood plasma, such that the viscosity μ_t is set equivalent to the plasma one at body temperature, which will be later denoted by μ_{ref}. Regarding the vessels, we start assuming a steady incompressible Navier-Stokes model for blood flow, namely:

$$\rho(\mathbf{u}_v \cdot \nabla)\mathbf{u}_v - \mu_v \Delta \mathbf{u}_v + \nabla p_v = 0 \tag{1.2}$$

where $\mathbf{u}_v$, μ_v, p_v, ρ are respectively velocity, viscosity, pressure and density of the fluid in the vessels.
This model assumption, together with the imposition of mass conservation in both tissue and vessels, lead to the following problem:

$$\begin{cases} \mathbf{u}_t + \dfrac{\mathrm{K}}{\mu_t} \nabla p_t = 0 & \text{in } \Omega_t \\ \nabla \cdot \mathbf{u}_t = 0 & \text{in } \Omega_t \\ \rho(\mathbf{u}_v \cdot \nabla)\mathbf{u}_v - \mu_v \Delta \mathbf{u}_v + \nabla p_v = 0 & \text{in } \Omega_v \\ \nabla \cdot \mathbf{u}_v = 0 & \text{in } \Omega_v \end{cases} \tag{1.3}$$

At this step the tissue and the vessels are still completely uncorrelated. To coupled the problem we have to introduce a certain imposed continuity of the flow at the interface $\Gamma = \partial\Omega_t \cup \partial\Omega_v$ namely:

$$\mathbf{u}_v \cdot \mathbf{n} = \mathbf{u}_t \cdot \mathbf{n} = f(p_t, p_v) \text{ with } f(p_t, p_v) = L_p((p_v - p_t) - \sigma R_g T(c_v - c_t)), \quad (1.4a)$$

$$\mathbf{u}_t \cdot \boldsymbol{\tau} = 0, \quad \text{on } \Gamma \quad (1.4b)$$

where $\mathbf{n}$ and $\boldsymbol{\tau}$ are the outward unit normal vector and the unit tangent vector on the capillary surface.

The fluid flux across the capillary wall can be obtained on the basis of linear non-equilibrium thermodynamic arguments, originally developed by Kedem and Katchalsky. In particular L_p is the hydraulic conductivity of the vessel wall, R_g is the universal gas constant and T is the absolute temperature. In (1.4) c_v and c_t represent the effect of proteins, mostly albumin, on the osmotic (or oncotic) pressure gradient. Namely, $-\sigma R_g T(c_v - c_t)$ is the net osmotic pressure gradient across the capillary wall. Because of osmosis, the pressure drop across the capillary wall is affected by the difference in the concentration of chemicals, namely $c_v - c_t$, where c_v and c_t denote the concentration in the capillaries and in the interstitium, respectively. The osmotic pressure is modulated by the reflection coefficient σ that quantifies the departure of a semi-permeable membrane from the ideal permeability (where any molecule is able to travel across the membrane without resistance). We assume that c_v and c_t are given and are independent of r, s, θ.

The previous model allows us to capture the phenomena that we are interested in, but there are some technical difficulties that arise in the numerical approximation of the coupling between a complex network with the surrounding volume, a multiscale approach based on the Immersed Boundary Method (IBM) can be exploited. To avoid resolving the complex 3D geometry of the vascular network, the combination of the IBM and the assumption of large aspect ratio between vessel radius and capillary axial length can be convenient. Precisely, with this approach, a suitable rescaling of the equations is applied and the capillary radius is let going to zero ($\mathrm{R} \to 0$). In this way, the 3D description of the vessels is reduced to a simplified 1D representation and the immersed interface and the related interface conditions are replaced by an equivalent mass source. As we will see this will bring some

difficulty to prove the well-posedness of this first approach, and it will be necessary to deduce another formulation in order to prove it. We will refer to [18] for this prove.

1.2 Flow equation with arbitrary geometry

In order to derive a governing flow equation for the vessel on arbitrary geometry we can proceed as follows. Since we are dealing with cylindrical geometries let us define a local cylindrical coordinate system (r, θ, s) at each point of the centerline Γ of the capillaries. We indicate with $\mathbf{e}_r$,$\mathbf{e}_\theta$,$\mathbf{e}_s$ the radial,circumferential and axial unit vectors. We will deduce our one dimensional multiscale model starting from the one for large arteries introduce in [29].These reduced models are obtained after integrating the Navier-Stokes equation over a vessel section, supposed to be circular, and assuming an algebraic wall law to describe the relationship between pressure and wall deformation. This model is based on the following geometric, kinematic and dynamic assumptions:

Circular section For each value of the arc length s along a network branch, the intersection between the orthogonal plan to $\mathbf{e}_s$ and the vessel is circular.

Dominance of axial velocity The radial and circumferential velocity components are negligible compared to the axial component, namely $\mathbf{u}_v = [0, 0, u_v(r, \theta, s)]^T$.

Body forces We neglect the effect of gravity and other possible types of body forces (inertia, Coriolis).

Steady flow We neglect transient phenomena since we are modeling phenomena in microcirculation, where the Womersley numbers at the level of capillary circulation are negligible. For this reasons, we just aim to determine the steady flow conditions.

Dominance of viscous forces Microcirculation is also characterized by the dominance of viscous forces over inertial forces acting on infinitesimal fluid particles, namely the Reynolds number characterizing the flow is low.

Viscosity We assume that the apparent viscosity of blood, μ_v is independent of the local deformation rate conditions. However, the viscosity is not a constant parameter but it depends on the hematocrit.

The neglect Coriolis affect and transient phenomena, this is the main difference between microcirculation and large arteries approach, where they introduce a momentum-flux correction coefficient α also called as Coriolis coefficient that will appear from the momentum equation as described in [29].
Considering this first assumptions we now deduce the new form of the mass balance and momentum equation governing an incompressible flow, such as blood, to the following form:

$$\text{from} \quad \nabla \cdot \mathbf{u}_v = 0 \qquad \text{to} \qquad u_r = u_\theta = 0, \quad \partial_s u_v = 0 \tag{1.5a}$$

$$\begin{aligned} \text{from} \quad & \rho(\mathbf{u}_v \cdot \nabla)\mathbf{u}_v - \mu_v \Delta \mathbf{u}_v + \nabla p_v = 0 \\ \text{to} \quad & -\mu_v \Delta u_v + \partial_s p_v = 0, \quad \partial_\theta p_v = 0, \quad \partial_r p_v = 0 \end{aligned} \tag{1.5b}$$

for any $(r, \theta, s) \in \Omega_v$ where Δ denotes the Laplace operator with respect to cylindrical coordinates

$$\Delta u = \frac{1}{r}\partial_r(r\partial_r u) + \frac{1}{r^2}\partial_\theta^2 u + \partial_s^2 u.$$

We now aim to transform this equation into a simpler one that is defined on the centerline of the capillary, solely, in case of curvilinear axis. To this purpose, we need to introduce first a parametrization of each curvilinear branch and from that other parameter. Let $\mathbf{\Psi} : \mathrm{R} \to \mathrm{R}^3$ be the parametric arg length, such that

$$\begin{aligned} \mathbf{\Psi} &\in C^3(\mathrm{R}), \\ \|d_z \mathbf{\Psi}(z)\| &= 1, \qquad \forall z \in [0, L] \end{aligned}$$

being L the length of a generic branch of the capillary network. Note that $s = \int_0^z \|d_\zeta \mathbf{\Psi}(\zeta)\| d\zeta = z$, due to the definition of arc length. Then, for starters, $d_\zeta \mathbf{\Psi}(\zeta)$ is the unit tangent vector to the curve, which we denote by $\mathbf{T}(s)$. Since $\mathbf{T}$ has constant length, $\mathbf{T}'(s)$ will be orthogonal to T(s). Assuming $\mathbf{T}'(s) \neq 0$, define the

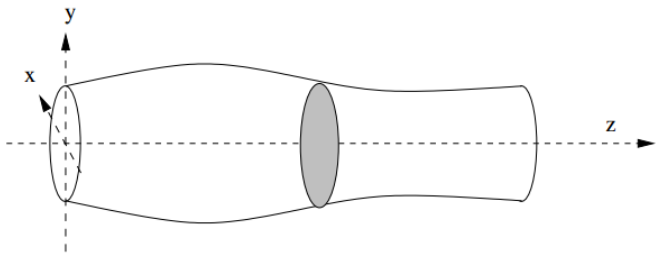

Figure 1.2: The cylindrical domain. The cylinder axis is aligned with the coordinate z.

principal normal vector $\mathbf{N}(s) = \mathbf{T}'(z)/\|\mathbf{T}'(z)\|$ and the curvature $\kappa(z) = \|\mathbf{T}'(z)\|$. So far, we have

$$\mathbf{T}'(z) = \kappa(z)\mathbf{N}(z) = d_{zz}\mathbf{\Psi}(z). \tag{1.6}$$

Therefore, given the curvature κ and the centripetal unitary direction $\mathbf{N}$, we have that the center of the osculating circle C_0 is the point in direction $\mathbf{N}(z)$ whose distance from $\mathbf{\Psi}(z)$ is $1/\kappa$, where $1/\kappa$ is the curvature radius.

In order to proceed with the one-dimensional model derivation, we will impose the following assumption: the axial velocity profile can be decomposed as

$$u_v(r, \theta, s) = \bar{u}_v(s)\Phi(r, \theta) \tag{1.7}$$

where $\bar{u}_v$ represents the mean or bulk velocity of the blood stream on each cross section identified by the arc length s, denoted by $\Sigma(s)$, and $\Phi : \mathrm{R}^3 \to \mathrm{R}$ is the velocity profile on the curvilinear vessel. The fact that the velocity profile doesn't vary in space is in contrast with experimental observation, but it is a necessary assumption in order to deduce a receded model. This profile in both linear or curve configuration, can be seen as an average flow configuration.

There are many different possibilities to choose the form of this shape factor $\Phi(r, \theta)$, but in this work we are going to use the following second order approximation:

$$\Phi(r, \theta) = \phi(r/R)(1 + ar\cos\theta + br\sin\theta + cr^2\cos\theta\sin\theta + dr^2\cos^2\theta + er^2\sin^2\theta).$$

where a,b,c,d and e are constant depending on the curvature and other assumption, while $\phi(r/R)$ is the radially symmetric part of the velocity profile in the linear

case, usually modeled as:

$$\phi(\rho) = \frac{\gamma+2}{\gamma}\left(1-\rho^{\gamma}\right).$$

which coincides with the classic Poiseuille parabolic flow profile (observed in straight cylindrical channels) for $\gamma = 2$.

We aim to find a suitable expression for the parameters a, b, c, d, e in terms of the geometry of the arc, namely $\mathbf{\Psi}$, such that the shape factor coincides with the classic parabolic Poiseuille profile when the arc is rectilinear, while it deviates from this pattern when the arc is curved. For different curvature values, we can see as the profile assume a not symmetric shape around the centerline due to the external movement. To this purpose, we set the following additional assumptions:

Set up notation In order to simplify our equation, we will use the following notation for the mean pressure and velocity on a section Σ and on its boundary for the pressure term regarding the tissue:

$$\bar{u}_v(s) = \frac{1}{\pi R^2}\int_{\Sigma(s)} u_v \, d\sigma\,, \quad \bar{p}_v(s) = \frac{1}{\pi R^2}\int_{\Sigma(s)} p_v \, d\sigma\,, \quad \bar{\bar{p}}_t(s) = \frac{1}{2\pi R}\int_{\partial\Sigma(s)} p_t \, d\sigma.$$

Choice of θ To simplify our calculation we assume that on each cross section the axis $\theta = 0$ is collinear with the vector $\mathbf{N}$, this means that on each section all the vectors with $\theta = 0$ are in $\mathbf{N}$ direction.

Symmetry of the profile We require that the velocity profile in each section is such that $\Phi(r,\theta,\psi) = \Phi(r,-\theta,\psi) \quad \forall r,\theta,\psi$. As a result of that the coefficient b, c must vanish, namely $b = c = 0$.

Linear dependence We assume that the correction factor to the velocity profile at any point s, namely $(1 + ar\cos\theta + br\sin\theta + cr^2\cos\theta\sin\theta + dr^2\cos^2\theta + er^2\sin^2\theta)$ is linearly dependent of the distance from the center of the osculating circle relative to this point.

We are now able to determine the coefficients a, d, e which satisfy these assumptions. For the linear dependence of the velocity with the distance from the center of the osculating circle, our profile must be zero in $C_0 = (r = 1/\kappa, \theta = 0, \psi)$, that is $(1 + a/\kappa + d/\kappa^2) = 0 \rightarrow d = -a\kappa - \kappa^2$. Furthermore, since the velocity

profile is linear dependent to the distance from the center of the osculating circle we have that all the points with distance $1/\kappa$ from it must have the same velocity. The set of points of each cross section with distance $1/\kappa$ from the point C_0 are:

$$\varphi = \{(r,\theta): \quad r = \frac{2\cos\theta}{\kappa}, \quad \theta \in [-\frac{\pi}{2}; +\frac{\pi}{2}]\}.$$

Moreover we have that $\Phi(r=0,\theta,\psi) = \phi(0)$ and so $\forall (r,\theta) \in \phi$ then $\Phi(r,\theta,\psi) = \phi(r/R)$. It follows that $\forall (r,\theta) \in \varphi$:

$$0 = ar\cos\theta + dr^2\cos^2\theta + er^2\sin^2\theta = 2\frac{a}{\kappa}\cos^2\theta + 4\frac{d}{\kappa^2}\cos^4\theta + 4\frac{e}{\kappa^2}\cos^2\theta\sin^2\theta.$$

Now for $\theta = \pm\frac{\pi}{2}$ the equation is verified. In the other cases we can divide all by $2\cos^2\theta/\kappa^2$, to obtain:

$$0 = a\kappa + 2d\cos^2\theta + 2e\sin^2\theta \qquad \forall\theta \in (-\frac{\pi}{2}; +\frac{\pi}{2}).$$

To find the value of the parameters we need two more equations. Thus, we test it on two particular cases: $\theta = \pi/4, \theta = \pi/3$. For $\theta = \pi/4$, using $d = -a\kappa - \kappa^2$ we obtain:

$$0 = a\kappa + 2d(\frac{1}{2}) + 2e(\frac{1}{2}) = a\kappa + d + e = a\kappa - \kappa^2 - a\kappa + e = e - \kappa^2.$$

For that $e = \kappa^2$. Finally for $\theta = \pi/3$, using the previous result we have:

$$0 = a\kappa + 2d(\frac{1}{4}) + 2e(\frac{3}{4}) = a\kappa + \frac{d}{2} + \frac{3e}{2} = a\kappa - \frac{\kappa^2}{2} - \frac{a\kappa}{2} + \frac{3\kappa^2}{2} = \frac{a\kappa}{2} + \kappa^2$$

So we obtain $a = -2\kappa$ and $d = \kappa^2$. In a general configuration the curvature is dependent on the arc length $\kappa = \kappa(s)$.

In conclusion, the velocity profile is of the form:

$$\Phi(r,\theta,\psi) = \phi(rR^{-1})(1 + r^2\kappa^2(\psi) - 2\kappa(\psi)r\cos\theta). \tag{1.8}$$

A visualization of such profile is provided in Figure 1.3.

Now we derive the reduced model for flow in curved vessels by replacing the velocity profile (1.8) into the mass and momentum balance equations (1.5a) and we integrate these equations on a portion of vessel, P delimited by two cross sections

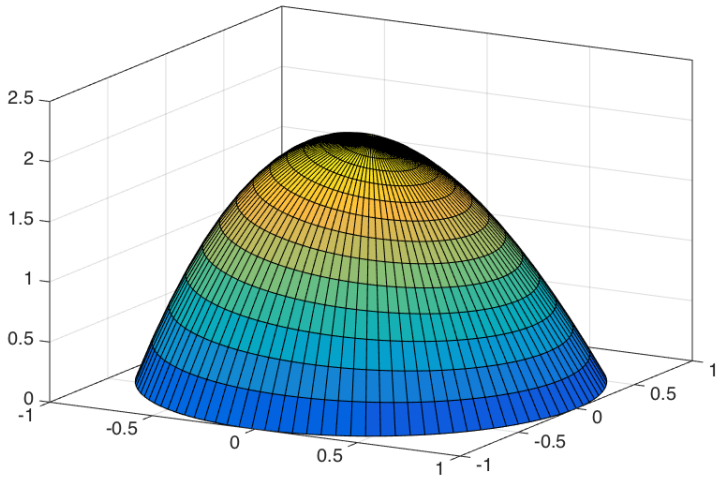

Figure 1.3: Visualization of the velocity profile for a curved pipe. The curvature is such that $\kappa R = 0.11$ as in the numerical simulations.

$\Sigma(s_1), \Sigma(s_2),\ s_2 > s_1$. In this way, we obtain simplified equations that depend only on the arc length s. We start first from the continuity equation, using the fact that $\mathbf{n} = \mathbf{e}_s$ on $\Sigma(s_1)$ and $\Sigma(s_2)$ we obtain:

$$
\begin{aligned}
0 &= \int_P \nabla \cdot \mathbf{u}_v d\Omega = \int_{\partial P} \mathbf{u}_v \cdot \mathbf{n}\, d\sigma \\
&= \int_{\Sigma(s_1)} \mathbf{u}_v \cdot \mathbf{n} d\sigma + \int_{\Sigma(s_2)} \mathbf{u}_v \cdot \mathbf{n}\, d\sigma + \int_{\Gamma} \mathbf{u}_v \cdot \mathbf{n}\, d\sigma \\
&= -\int_{\Sigma(s_1)} u_v\, d\sigma + \int_{\Sigma(s_2)} u_v\, d\sigma + \int_{\Gamma} f(p_t, p_v)\, d\sigma \\
&\simeq -\bar{u}_v(s_1)\pi R^2(s_1) + \bar{u}_v(s_2)\pi R^2(s_2) + \int_{s_1}^{s_2} f(\bar{p}_t, p_v) dz \\
&= \int_{s_1}^{s_2} [f(\bar{\bar{p}}_t, \bar{p}_v) + \partial_s(\pi R^2 \bar{u}_v)] dz\,.
\end{aligned}
\tag{1.9}
$$

According to (1.5a), in particular $\partial_r p_v = \partial_\theta p_v = 0$, we notice that $p_v(r, s, \theta) = \bar{p}_v(s)$. Furthermore, in equation (1.9) we have adopted the assumption that the radius of the capillary is small if compared to the domain Ω. More precisely, we have set

that

$$\int_\Gamma f(p_t,p_v)\,d\sigma = \int_{s_1}^{s_2}\int_0^{2\pi} f(p_t,p_v)R(s)d\theta\,ds = \\ = \int_{s_1}^{s_2}\int_0^{2\pi} f(p_t,\bar{p}_v)R(s)d\theta\,ds \simeq \int_{s_1}^{s_2} 2\pi R(s) f(\bar{\bar{p}}_t,\bar{p}_v)\,ds\,,$$

where the last approximation becomes exact when $R\to 0$ because,

$$\lim_{R\to 0}\int_0^{2\pi} f(p_t(R(s),s,\theta),\bar{p}_v)d\theta = \lim_{R\to 0} f(\bar{\bar{p}}_t(s),\bar{p}_v)\,.$$

Since the cross sections $\Sigma(s_1)$, $\Sigma(s_2)$ are arbitrarily chosen, we conclude that the equation holds pointwise, namely

$$\partial_s(\pi R^2\bar{u}_v) + 2\pi R(s) f(\bar{\bar{p}}_t,\bar{p}_v) = 0. \tag{1.10}$$

Let us now apply the averaging technique to the momentum balance equation, that is the last of (1.5a). We have:

$$\int_P \Delta u_v\,d\Omega = \int_{\partial_P}\nabla u_v\cdot\mathbf{n}\,d\sigma = -\int_{\Sigma(s_1)}[\partial_s u_v\,d\sigma + \int_{\Sigma(s_2)}\partial_s u_v\,d\sigma + \int_\Gamma \nabla u_v\cdot\mathbf{n}\,d\sigma = \\ = \int_\Gamma \nabla u_v\cdot\mathbf{e}_r\,d\sigma = \int_\Gamma \partial_r u_v d\sigma = \int_\Gamma \bar{u}_v(s)\partial_r\Phi(r,\theta)d\sigma = \\ = \int_\Gamma \bar{u}_v(s)R^{-1}\phi'(rR^{-1})(1-2\kappa r\cos\theta+\kappa^2r^2) + \phi(rR^{-1})(2\kappa^2 r - 2\kappa\cos\theta)\,d\sigma \\ = \int_{s_1}^{s_2}\int_0^{2\pi}\bar{u}_v(s)R\big(R^{-1}\phi'(1)(1-\kappa\cos\theta+\kappa^2R^2) + \phi(1)(2\kappa^2R-2\kappa\cos\theta)\big)d\theta ds. \tag{1.11}$$

Now using the fact that $\phi(1)=0$, the periodicity of $\cos\theta$ we obtain:

$$\int_P \Delta u_v\,d\Omega = \int_{s_1}^{s_2} 2\pi\phi'(1)(1+\kappa^2R^2)\bar{u}_v(s)\,ds, \tag{1.12}$$

such that the averaged/one-dimensional form of the momentum equation becomes

$$-2\pi\mu_v(s)\phi'(1)\big(1+\kappa^2(s)R^2\big)\bar{u}_v(s) + \pi R^2\partial_s\bar{p}_v(s) = 0. \tag{1.13}$$

1.3 Generalization to a network of vessels

Now that we deduce the equation for the reduce model based on multiscale approach in the vessel, we have to extend this results to a general and more complex configuration. Since we are working under the hypothesis of microcirculation a quasi-statics approximation is acceptable.
To do this we decompose the network Λ into single branches namely $\Lambda_i, i = 1, ..., N$. Every branch is parametrized by the arc length s_i and a tangent unit vector λ_i is defined over each branch, that can vary based to the branch orientation. Differentiation over the branches is defined using the tangent unit vector, namely $\partial_{s_i} := \boldsymbol{\lambda}_i \cdot \nabla$ on Λ_i, i.e. ∂_{s_i} represents the projection of ∇ along $\lambda_{\mathbf{i}}$.
After we define this first assessment we can impose the coupled of the problem on all the network enforcing some constrains at the junctions. Fist of all, we add other notation to clarify the description of the network. Junctions are defined as the point $\mathbf{y}$ such that

$$\mathbf{y}_j = \boldsymbol{\Psi}_i(s_i^*) = \boldsymbol{\Psi}_{\hat{i}}(s_{\hat{i}}^*), s_i^* \in \{0, L_i\} \, \forall i, \hat{i} = 1, ..., N$$

Let gather together the junctions with index $j = 1, ..., M$ and for every junction j we denote with $\mathcal{K}_j$ the set of the branch that begin or end with this junction j, such that $\boldsymbol{\Psi}_i(s_i^*) = \mathcal{K}_j$.
In addition to junctions there are branches that end inside or at the boundary of the domain Ω. Therefore we can combine the indexes of the branches that end inside the tissue, called *dead ends*, in $\mathcal{E}$ and we identify them with the symbol $\mathbf{z}$. The latter points are called *boundary ends* and are denoted with the symbol $\mathbf{x}$. The set of branches intersecting the outer boundary is $i \in \mathcal{B}$.
Let now define two different notation for the index of the branches at every junction, they will be useful later on. Given a branch with orientation λ_i, let $\mathbf{e}_s$ be the outgoing tangential unit vector on both extreme; we define *ingoing endpoints* the node where $\boldsymbol{\lambda}_i \cdot \mathbf{e}_s(s) < 0$ and *outgoing endpoints* the one where $\boldsymbol{\lambda}_i \cdot \mathbf{e}_s(s) > 0$. Considering every junction j we classify as $\mathcal{K}_j^-$ the index i of the branches where the j-junction represent an ingoing-node, and with $\mathcal{K}_j^+$ the index of the outgoing branches.
If we consider the direction of the flow instead, we classify as inflow endpoints the branches' index where $\bar{u}_v(s)\boldsymbol{\lambda}_i \cdot \mathbf{e}_s(s) < 0$ for $s = 0$ and $s = L$. The *outflow* points

are instead the ones such that $\bar{u}_v(s)\boldsymbol{\lambda}_i \cdot \mathbf{e}_s(s) > 0$. We collect the following index in $\mathcal{K}_j^{in}$, $\mathcal{K}_j^{out}$, respectively.
As we did for the indexes of the branches at every junction, we subdividing under the same condition the *boundary ends* into ingoing or outgoing, namely $\mathbf{x}^-, \mathbf{x}^+$, or into inflow and outflow $\mathbf{x}^{in}, \mathbf{x}^{out}$. We clarify that the definition of ingoing/outgoing or inflow/outflow is always refereed to the role of the junction with respect to the neighboring branches.

Let postpone the discussion about the boundary condition for the moment and let us consider the fact that specify the only value at the boundary is necessary but not sufficient to find the solution of the problem. First of all, we need to specify some compatibility condition on the velocity and pressure in the vessel. We enforce two different condition at every junction:

- continuity of pressure

- balance of flow rate

imposing the following condition:

$$\bar{p}_{v,i} = \bar{p}_{v,\bar{i}}, \quad i, \bar{i} \in \mathcal{K}_j, j = 1, 2, ..., M \tag{1.14a}$$

$$\sum_{i \in \mathcal{K}_j} \pi \mathrm{R}_k^2 \bar{u}_{v,i} = 0, \quad j = 1, 2, ..., M. \tag{1.14b}$$

This means that the sum of the volumetric flow rate on all the ingoing branches as to be equal to the one in all the outgoing branches. We will specify later on that in our model the only configuration admissible are bifurcation or anastomosis. At dead ends of the network we impose the no-flow condition setting $\pi \mathrm{R}_k^2 \bar{u}_v|_{\mathbf{z}_i} = 0, i \in \mathcal{E}$, where $|_{\mathbf{z}_i}$ means that we are evaluating this term at the point $\mathbf{z}_i$. Another assumption that we are doing on this point is that we consider that branch extreme as an outgoing point, that satisfy $\boldsymbol{\lambda}_i \cdot \mathbf{e}_s(s = L) > 0$.

In conclusion, the coupled model that describes the mean velocity and pressure

of blood flow in the network is the following,

$$\begin{cases} \partial_s\big(\pi R_i^2(s)\bar{u}_{v,i}(s)\big) + 2\pi R_i(s) f(\bar{\bar{p}}_t(s), \bar{p}_v(s)) = 0 & \text{on } \Lambda_i,\ i = 1, \dots, N\,, \\ -2\pi\mu_{v,i}(s)\phi'(1)\big(1 + \kappa_i^2(s)R_i^2(s)\big)\bar{u}_{v,i}(s) + \partial_s\bar{p}_{v,i}(s) = 0 & \text{on } \Lambda_i,\ i = 1, \dots, N\,, \\ \sum_{i\in\mathcal{K}_j} \pi R_k^2 \bar{u}_{v,i}|_{\mathcal{K}_j} = 0, & j = 1, 2, \dots, M\,, \\ \bar{p}_{v,i}|_{\mathcal{K}_j} = \bar{p}_{v,\hat{i}}|_{\mathcal{K}_j} & i, \hat{i} \in \mathcal{K}_j,\ j = 1, 2, \dots, M\,. \end{cases} \tag{1.15}$$

1.4 Coupled problem between tissue and vessel

The previous model is able to capture the phenomena in the vessel, considering possible curve network configuration, we aim now to modify the coupled term introduced in paragraph 1.1 following the already introduced idea of the Immerse Boundary Method. We can represent the effect of $f(\bar{\bar{p}}_t(s), \bar{p}_v(s))$ on Λ as a mass source term F distributed on the entire domain Ω,

$$F(\bar{\bar{p}}_t(s), \bar{p}_v(s)) = f(\bar{\bar{p}}_t(s), \bar{p}_v(s))\delta_{\Lambda_i}, \tag{1.16}$$

where $\delta_{\Lambda i}$ denote the distribution of Dirac masses along the manifold Λ_i. More precisely, F is the Dirac measure concentrated on Λ_i, having density f, defined by:

$$\int_{\Omega_t} F(\bar{\bar{p}}_t(s), \bar{p}_v(s)) v d\mathbf{x} = \int_{\Lambda} f(\bar{\bar{p}}_t(s), \bar{p}_v(s)) v d\sigma \qquad \forall v \in C^\infty(\Omega_t).$$

Note that f is an integral operator, in fact it includes the computation of the mean velocity and pressure on a section of the vessel and on its boundary, respectively.

As presented in [9] when R goes to 0, the mass flux per unit area becomes an equivalent mass flux per unit length, on the centerline Λ_i. Considering now a plane orthogonal to $\Lambda = \cup_{i=1}^N \Lambda_i$ locates at s, let $\gamma(s)$ be the intersection of Γ with it, and let (s, θ) be the local axial and angular coordinates on the cylindrical surface generated by Γ with radius R. Using the mean value theorem we can represent the action of F on v in this way:

$$\begin{aligned} & & \exists \quad \tilde{\theta} \in [0, 2\pi] \quad \text{s.t.} \\ \int_{\Omega_t} F(\bar{\bar{p}}_t(s), \bar{p}_v(s)) v d\mathbf{x} \quad &= \quad \int_\Lambda \int_{\gamma(s)} f(\bar{\bar{p}}_t(s), \bar{p}_v(s)) v(s,\theta) \mathrm{R} d\theta ds \quad = \\ & \int_\Lambda |\gamma(s)| f(\bar{\bar{p}}_t(s), \bar{p}_v(s)) v(s) ds, \qquad\qquad \forall v \in C^\infty(\Omega_t) \end{aligned} \tag{1.17}$$

under the assumption of linearity of function f in s and small radii, that is $\mathrm{R} \ll |\Omega_t|^{\frac{1}{d}}$.
Then, thanks to equation (1.17) we can express the continuity equation in the tissue in differential form using Dirac density function on Λ, considering that this term should be oppposite to $f(\bar{\bar{p}}_t(s), \bar{p}_v(s))$, it becomes:

$$\nabla \cdot \mathbf{u}_t - 2\pi \mathrm{R}(s) f(\bar{\bar{p}}_t(s), \bar{p}_v(s)) \delta_\Lambda = 0. \tag{1.18}$$

We can now identify Ω_t with all Ω. Replacing now this equation and the previous in this section inside the problem (1.3) we obtain the coupled model that descibe the flow model in a 3D tissue with one-dimensional channels as follows:

$$\begin{cases} \nabla \cdot \mathbf{u}_t - 2\pi R(s) f(\bar{\bar{p}}_t(s), \bar{p}_v(s)) \delta_\Lambda = 0 & \text{in } \Omega \\ \mathbf{u}_t + \frac{\mathrm{K}}{\mu_t} \nabla p_t = 0 & \text{in } \Omega \\ \partial_s \big(\pi R_i^2(s) \bar{u}_{v,i}(s) \big) + 2\pi R_i(s) f(\bar{\bar{p}}_t(s), \bar{p}_v(s)) = 0 & \text{on } \Lambda_i, \ i = 1, \dots, N, \\ -2\pi \mu_{v,i}(s) \phi'(1) \big(1 + \kappa_i^2(s) R_i^2(s) \big) \bar{u}_{v,i}(s) + \partial_s \bar{p}_{v,i}(s) = 0 & \text{on } \Lambda_i, \ i = 1, \dots, N, \\ \sum_{i \in \mathcal{K}_j} \pi R_k^2 \bar{u}_{v,i}|_{\mathcal{K}_j} = 0, & j = 1, 2, \dots, M, \\ \bar{p}_{v,i}|_{\mathcal{K}_j} = \bar{p}_{v,\hat{i}}|_{\mathcal{K}_j} & i, \hat{i} \in \mathcal{K}_j, \ j = 1, 2, \dots, M. \end{cases} \tag{1.19}$$

1.5 Boundary conditions

In order to provide a well-posed problem we need to impose suitable boundary condition on both tissue boundary $\partial\Omega$ and vessel network boundary $\partial\Lambda$. Regarding the interstitial domain Ω we can decompose the extreme in:

$$\partial\Omega = \Gamma_p \cup \Gamma_u, \qquad \text{s.t.} \qquad \mathring{\Gamma}_p \cap \mathring{\Gamma}_u \neq 0. \tag{1.20}$$

Concerning the vessel boundary, we already discuss about the definition of dead ends, boundary extreme and the treatment of junction. We are presenting in this section a better explanation introducing another simplified notation.
Let $\partial\Lambda$ be the set of the inflow Λ^{in} and outflow Λ^{out} points of the network vessel, that not consider junctions points. As previous define this set include points inside the tissue and on its boundary, set out respectively in $\mathcal{E}$ and $\mathcal{B}$. The partition of the vessel boundary is clarify as follows:

$$\partial\Lambda = \Lambda^{in} \cup \Lambda^{out}, \qquad \mathcal{E} = \mathcal{E}_u = \partial\Lambda \cap \partial\Omega, \qquad \mathcal{B} = \mathcal{B}_p = \partial\Lambda \cap \mathring{\Omega}. \tag{1.21}$$

We introduced the notation with subscripts p and v, they characterize the subset where we impose a boundary condition for pressure or velocity respectively. Regarding the pressure, we impose Dirichlet condition on both domain:

$$\begin{aligned} p_t &= g_t && on \quad \Gamma_p \\ p_v &= g_v && on \quad \mathcal{B} \end{aligned}$$

for the velocity instead Neumann conditions can be treated as essential conditions using Robin (mixed) methods, imposing a fixed value for the normal flux, namely:

$$\begin{aligned} \mathbf{u}_t \cdot \mathbf{n} &= -\kappa_t \nabla p_t \cdot \mathbf{n} = \beta_t(p_t - p_0) && on \quad \Gamma_u \\ \pi \mathrm{R}^2 u_v &= -\kappa_v \nabla p_v \cdot \mathbf{n} = \beta_v(p_v - p_0) && on \quad \mathcal{E} \end{aligned}$$

where p_0 represents far field pressure, while β_t and β_v can be interpreted as an

effective conductivity accounting for layers of tissue surrounding the considered sample. For the pressure datum we required the usual regularity for boundary function, namely $g_t \in L^2(\Gamma_p)$ for the tissue and $g_v \in L^2(\mathcal{B})$ for the vessel. Observe that we can enforce Neumann, the imposition of null normal velocity, at the boundary by choosing $\beta_t \simeq 0$ and $\beta_v \simeq 0$ with Robin-Type condition, respectively.

1.6 Dimensional Analysis

Writing the equations in dimensionless form is essential to highlight the most significant mechanisms governing the fluid dynamics between the tissue and the microcirculation. We first identify the characteristic dimensions for our problem in terms of length d,the average radius of the capillary network, velocity U,average velocity in the capillary bed and pressure P, average pressure in the interstitial space. From this choice of primary parameters we can deduce the corresponding derived one as follows:

$$\mathrm{R}' = \frac{\mathrm{R}}{d} \qquad \text{dimensionless radius}$$

$$\kappa' = \frac{\kappa}{d} \qquad \text{dimensionless curvature}$$

$$k_t = \frac{kP}{\mu U d} \qquad \text{dimensionless interstitial permeability}$$

$$Q = 2\pi \mathrm{R}' L_p \frac{P}{U} \qquad \text{dimensionless wall permeability}$$

$$k_v = \frac{\pi \mathrm{R}'^4}{2\mu(\gamma+2)} \frac{Pd}{U} \qquad \text{dimensionless vessel permeability}$$

Therefore, the coupled dimensionless problem of microcirculation and tissue interstitium reads as follows:

$$\begin{cases} \nabla \cdot \mathbf{u}_t - Q((\bar{p}_v - \bar{\bar{p}}_t) - \sigma(\pi_v - \pi_t))\delta_\Lambda = 0 & \text{in } \Omega \\ \frac{1}{k_t}\mathbf{u}_t + \nabla p_t = 0 & \text{in } \Omega \\ \partial_s\big(\bar{u}_{v,i}(s)\big) + \frac{Q}{2\pi \mathrm{R}_i'^2}((\bar{p}_v - \bar{\bar{p}}_t) - \sigma(\pi_v - \pi_t)) = 0 & \text{on } \Lambda_i,\ i = 1, \ldots, N\,, \\ \frac{\pi \mathrm{R}_i'^2}{k_v}\big(1 + \kappa_i'^2(s)\mathrm{R}_i'^2\big)\bar{u}_{v,i}(s) + \partial_s \bar{p}_{v,i}(s) = 0 & \text{on } \Lambda_i,\ i = 1, \ldots, N\,, \\ \sum_{i \in \mathcal{K}_j} \pi \mathrm{R}_k'^2 \bar{u}_{v,i}|_{\mathcal{K}_j} = 0, & j = 1, 2, \ldots, M\,, \\ \bar{p}_{v,i}|_{\mathcal{K}_j} = \bar{p}_{v,\hat{i}}|_{\mathcal{K}_j} & i, \hat{i} \in \mathcal{K}_j,\ j = 1, 2, \ldots, M\,. \end{cases} \tag{1.22}$$

For simplicity we use the same notation for dimensionless and non-dimensionless pressure and velocity, respectively. Regarding the boundary condition we rescale the pressure one with the characteristic pressure value P, whereas for the Robyn condition on the rest of the boundary we replace the conductivity for the tissue β_t with $\beta_t = k_t/D'$, $D' = D/d$, in which D represent the characteristic length of the interstitial domain, where we assumed that the interstitial pressure decays from p_t to p_0.

OSS: For the sake of simplicity, the same symbols for the standard and dimensionless variables and for the standard and dimensionless operators have been used. Notice that the dimensionality of Ît'ÎŻ is [length] âĹŠ2 and that the dimensionless Dirac distribution is again called Ît'ÎŻ.

1.7 Modeling the Fahraeus-Lindqvist and Plasma Skimming with Hematocrit Transport

As previously mentioned, the viscosity of blood flowing through very small channels can not be considered to be constant. The main factor that affects the *apparent* viscosity of blood is the volumetric concentration of red blood cells, namely the *hematocrit*. Several phenomenological models are available to quantify this dependence, we refer here to a widely used one, proposed in [25]:

$$\frac{\mu_v}{\mu_{ref}} = \left[1 + \left(\frac{\mu_{0.45}}{\mu_{ref}} - 1\right) \cdot \frac{(1-H)^C - 1}{(1-0.45)^C - 1} \cdot \left(\frac{D}{D-1.1}\right)^2\right] \cdot \left(\frac{D}{D-1.1}\right)^2 \quad (1.23)$$

where H is the *discharge hematocrit*, defined such that $(\pi R^2(s))\bar{u}_v(s)H(s)$ is the total flow of red blood cells that crosses a section $\Sigma(s)$ of a capillary. In the expression (1.23), C is a parameter depending on the diameter $D = 2R$ of the capillary and on the hematocrit H:

$$C = (0.8 + e^{-0.075D}) \cdot \left(-1 + \frac{1}{1 + 10^{-11}D^{12}}\right) + \frac{1}{1 + 10^{-11}D^{12}} \quad (1.24)$$

and $\mu_{0.45}$ is a nominal value viscosity, related to the value at 45% hematocrit,

$$\frac{\mu_{0.45}}{\mu_{ref}} = 6 \cdot e^{-0.085D} + 3.2 - 2.44 \cdot e^{-0.06D^{0.645}}. \quad (1.25)$$

The reference viscosity μ_{ref} is obtained from the dynamic viscosity of water (H_2O) as follows

$$\mu_{ref} = 1.8\mu_{H_2O} = 1.8\frac{\mu_0}{1 + 0.0337T + 0.00022T^2}. \quad (1.26)$$

where T is the temperature (measured in Celsius) and $\mu_0 = 1.808$ centi-Poise (cP) is the viscosity of water at 0 C^o.

The model (1.23) entails the need to model the dynamics of hematocrit in the microvascular network. To this purpose we propose a one-dimensional model for transport of hematocrit that will be coupled to (1.22). This model is set on the following assumptions.

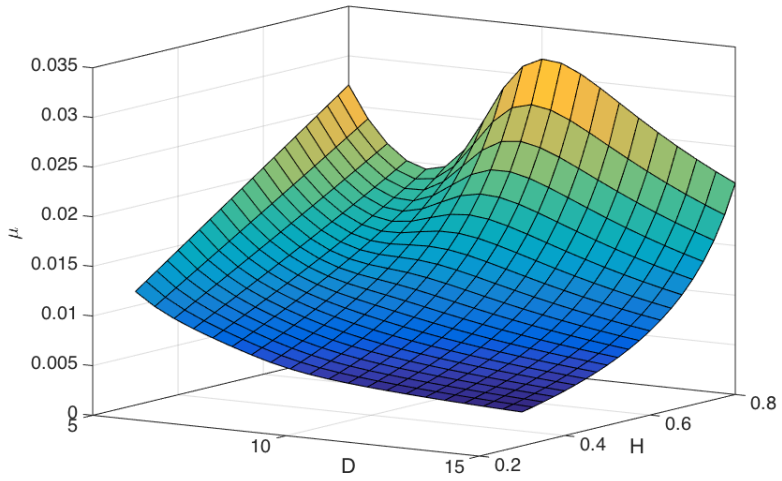

Figure 1.4: Visualization of the effective viscosity, calculated with expression (1.23), in terms of the hematorit and the capillary diameter.

Steady flow conditions As we did for the bulk flow model, we study the hematocrit transport in steady conditions.

Transport dominated regime Let us analyze the Péclét number that characterizes the hematocrit transport,

$$Pe = \frac{L\overline{v}}{D} \tag{1.27}$$

where $L \simeq 10^{-5}m$ is the RBC characteristic scale (also comparable with the capillary diameter), $\overline{v} \simeq 10^{-4}m/s$ is the average velocity of RBC in the capillaries and $D \simeq 10^{-12}m^2/s$ is the diffusivity parameter of RBC in water [7, 15, 22]. As a result we obtain $Pe \simeq 10^3$ that justifies the assumption.

Reactions and leak off We assume that the RBC do not leak off from the capillaries and we neglect any effects involving production or sequestration of RBC from the blood stream.

Absence of trifurcations at network junctions We assume that all the inner junctions of the network can be classified either as *anastomoses* or *bifurcations*.

On the basis of these hypotheses, the dynamics of hematocrit in a capillary network, where each capillary branch is modeled as a one-dimensional channel, is described by the mass balance equation. Denoting the flow rate of hematocrit across a single channel as Q_H, owing to the definition of discharge hematocrit we directly have $Q_H = \pi R^2 \bar{u}_v H$ and the mass balance equation for hematocrit becomes,

$$\partial_s\big(\pi R_i^2 \bar{u}_{v,i} H_i\big) = 0 \text{ on } \Lambda_i,\ i = 1, 2, \dots . \tag{1.28}$$

Equation (1.28) will be taken as the governing equation for hematocrit in each branch of the capillary network. We observe that this equation can be easily combined with the first of (1.22) to obtain

$$\pi R_i^2 \bar{u}_{v,i} \partial_s H - 2\pi R_i f(\bar{\bar{p}}_t, \bar{p}_v) H_i(s) = 0 \text{ on } \Lambda_i,\ i = 1, 2, \dots . \tag{1.29}$$

It shows that hematocrit is not constant along the axis of the branch, despite we neglect RBC reactions and leak off. However, hematocrit varies because the plasma can leak off and consequently the volumetric concentration of RBC may increase.

Equation (1.28) is not sufficient to uniquely determine the value of hematocrit in the network. It must be combined with suitable conditions for conservation of hematocrit at the junctions and at the boundary of the network. As (1.28) is a pure transport equation, it is well known that we have to prescribe a condition of the value of hematocrit at each *inflow* endpoint of the network branches. Let us denote by $\partial\Lambda_{in}$ the inflow points at the boundary of the network. On all these points we enforce a given value of hematocrit, namely $H = H_0$ on $\partial\Lambda_{in}$. For the *internal junctions* we exploit mass conservation of hematocrit. Let us consider a generic junction with multiple branches joining at a single node. Given the orientation of the flow, we can subdivide the branches into $K_{out} = \text{card}(\mathcal{K}_j^{out})$ outgoing ones and $K_{in} = \text{card}(\mathcal{K}_j^{in})$ inflow branches. We need to prescribe as many constraints as the number of inflow branches, namely N_{in}. Mass conservation always provides one constraint that is,

$$\sum_{i \in \mathcal{K}_j^{out}} \pi R_i^2 \bar{u}_{v,i} H_i = \sum_{i \in \mathcal{K}_j^{in}} \pi R_i^2 \bar{u}_{v,i} H_i \,. \tag{1.30}$$

The previous equation is not in general sufficient to close the problem in the case $K_{in} > 1$. The simple case $K_{in} = 1$ identifies anastomoses, where one, two or multiple outflow branches merge into a single inflow. In this case, since all the

terms on the left hand side are known, hematocrit value on the right is uniquely determined. In case of bifurcations, namely $K_{in} = 2$, the problem can be solved by means of the flow split model proposed in [24]. Since we exclude the presence of trifurcations or more complex configurations, this approach will be entirely sufficient to determine the distribution of hematocrit in the network. Without loss of generality, let us consider the classic Y-shaped configuration, where one parent vessel divides into two branches. We denote by the subscript f the quantities related to the parent vessel and with α, β the daughter branches. Given $Q_* = \pi R_*^2 \bar{u}_{v,*}$ with $* = f, \alpha, \beta$ and H_f, we aim to determine H_α and H_β, which provide hematocrit values at the inflow of the outgoing bifurcation branches. Using the approach of [24] we define,

$$F_{QB\alpha} = \frac{Q_\alpha}{Q_f} \quad F_{QE\alpha} = \frac{Q_\alpha H_\alpha}{Q_f H_f},$$

and we calculate these fractions using the following model

$$\begin{cases} F_{QE\alpha} = 0 & if\ F_{QB\alpha} \leq X_0 \\ \text{logit}(F_{QE\alpha}) = A + B\text{logit}(\frac{F_{QB\alpha} - X_0}{1-2X_0}) & if\ X_0 < F_{QB\alpha} < 1 - X_0 \\ F_{QE\alpha} = 1 & if\ F_{QB\alpha} \geq 1 - X_0 \end{cases} \tag{1.31}$$

where $\text{logit}(x) = \ln[x/(1-x)]$, X_0 is the fractional blood flow rate under which any RBC will flow into the daughter branch α and $D_*, , f, \alpha, \beta$ are the vessel diameters. Finally, the desired hematocrit levels are determined as

$$H_\alpha = F_{QE\alpha} H_f Q_f / Q_\alpha \,, \quad H_\beta = (1 - F_{QE\alpha}) H_f Q_f / Q_\beta \,. \tag{1.32}$$

1.8 Variational formulation

For complex geometry explicit solution of the problem are not available, therefore the only way to exploit this, is the proceed throw numerical simulation, going first of all to deduce the weak formulation of the problem.

1.8.1 Weak-formulation of the tissue problem

Due to the presence of the Dirac measure we cannot use standard regularity, but we need to introduce weighted Sobolev spaces introduced in [26].
Let consider a bounded open domain $\Omega \subset \mathbb{R}^d$ with Lipschitz boundary and an immersed surface Λ with dimension $\leq d-1$, we define:

$$L^2_\alpha(\Omega) := \left\{ v : \Omega \to \mathbb{R} \quad \text{measurable, s.t.} \quad \int_\Omega v^2(\mathbf{x}) d^{2\alpha}(\mathbf{x}, \Lambda) d\Omega < \infty \right\},$$

$$H^m_\alpha(\Omega) := \left\{ v \in L^2_\alpha(\Omega) \quad \text{s.t.} \quad Dv, ..., D^{(m)}v \in L^2_\alpha(\Omega) \right\},$$

for $\alpha \in (-1, 1)$, $m > 0$ and $d^{2\alpha}(\mathbf{x}, \Lambda) = dist(\mathbf{x}, \Lambda)$. This are Hilbert spaces with scalar product defined as:

$$(v, w)_{\alpha,\Omega} := \int_\Omega v^2(\mathbf{x}) w^2(\mathbf{x}) d^{2\alpha}(\mathbf{x}, \Lambda) d\Omega,$$

$$(v, w)_{\alpha,m,\Omega} := (v, w)_{\alpha,\Omega} + ... + (D^{(m)}v, D^{(m)}w)_{\alpha,\Omega}$$

from where we can define the inducted norm.
Let define another weighted Sobolev space that it will be useful later on:

$$H^{div}_{\alpha,\beta}(\Omega) := \left\{ \mathbf{v} \in L^2_\alpha(\Omega; \mathbb{R}^d) \quad \text{s.t.} \quad \nabla \cdot \mathbf{v} \in L^2_\beta(\Omega) \right\},$$

always with $\alpha, \beta \in (-1, 1)$. This is a Hilbert space with respect to the inner product

$$(\mathbf{v}, \mathbf{w})_{\alpha,\beta,\Omega} := (\mathbf{v}, \mathbf{w})_{\alpha,\Omega} + (\nabla \cdot \mathbf{v}, \nabla \cdot \mathbf{w})_{\beta,\Omega}.$$

It is possible now to specify the proper functional setting for pressure and velocity in the tissue, respectively:

$$\mathbf{V}_t = H^{div}_{\alpha,\beta}(\Omega) \qquad \text{and} \qquad Q_t = L^2_\alpha(\Omega). \tag{1.33}$$

In order to obtain the weak formulation of the tissue interstitium problem, we multiply equations 1.22(a),(b) with sufficiently smooth functions and integrate over the volume Ω, namely:

$$\int_\Omega \frac{1}{k_t}\mathbf{u}_t \cdot \mathbf{v}_t d\Omega + \int_\Omega \nabla p_t \cdot \mathbf{v}_t d\Omega = 0 \tag{1.34}$$

$$\int_\Omega (\nabla \cdot \mathbf{u}_t) q_t d\Omega - \int_\Omega Q((\bar{p}_v - \bar{\bar{p}}_t) - \sigma(\pi_v - \pi_t))\delta_\Lambda q_t d\Omega = 0 \tag{1.35}$$

We can now apply the Green's theorem to 1.35 to obtain an anti-symmetric formulation of Darcy's problem in the tissue:

$$\int_\Omega \frac{1}{k_t}\mathbf{u}_t \cdot \mathbf{v}_t d\Omega - \int_\Omega p_t(\nabla \cdot \mathbf{v}_t) d\Omega + \int_{\partial\Omega} p_t \mathbf{v}_t \cdot \mathbf{n} d\sigma = 0 \tag{1.36}$$

$$\int_\Omega (\nabla \cdot \mathbf{u}_t) q_t d\Omega - \int_\Omega Q((\bar{p}_v - \bar{\bar{p}}_t) - \sigma(\pi_v - \pi_t))\delta_\Lambda q_t d\Omega = 0 \tag{1.37}$$

Let discuss now about the treatment of the boundary term. Thanks to linearity of the integral, we can rewrite the boundary term in 1.36 by splitting the integral and enforcing the correct conditions, Dirichlet for the pressure term and Robin for the mixed part, namely:

$$\int_{\partial\Omega_t} p_t \mathbf{v}_t \cdot \mathbf{n} d\sigma = \int_{\Gamma_p} g_t \mathbf{v}_t \cdot \mathbf{n} d\sigma + \int_{\Gamma_u} p_0 \mathbf{v}_t \cdot \mathbf{n} d\sigma + \frac{1}{\beta_t}\int_{\Gamma_u} (\mathbf{u}_t \cdot \mathbf{n})(\mathbf{v}_t \cdot \mathbf{n}) d\sigma \tag{1.38}$$

By substituting this in the previous equations, the weak formulation of the problem tissue reads as:

$$\begin{aligned}\int_\Omega \frac{1}{k_t}\mathbf{u}_t \cdot \mathbf{v}_t d\Omega + \frac{1}{\beta_t}\int_{\Gamma_u} (\mathbf{u}_t \cdot \mathbf{n})(\mathbf{v}_t \cdot \mathbf{n}) d\sigma - \int_\Omega div(\mathbf{v}_t) p_t d\Omega = \\ = -\int_{\Gamma_p} g_t \mathbf{v}_t \cdot \mathbf{n} d\sigma - \int_{\Gamma_u} p_0 \mathbf{v}_t \cdot \mathbf{n} d\sigma\end{aligned} \tag{1.39}$$

$$\int_\Omega (\nabla \cdot \mathbf{u}_t) q_t d\Omega - \int_\Omega Q((\bar{p}_v - \bar{\bar{p}}_t) - \sigma(\pi_v - \pi_t))\delta_\Lambda q_t d\Omega = 0. \tag{1.40}$$

1.8.2 Weak-formulation of the vessel problem

Regarding the network, we are going to require regularity for vessel velocity and pressure over each branch separately. Reminding that we are imposing the pressure continuous at every junctions, $p_v(s) \in C^0(\bar{\Lambda})$ and velocity discontinuous in order to provide the mass conservation, we demand that $u_v \in V_v$ and $p_v \in Q_v$

defined as:

$$V_v = \bigcup_{i=1}^{N} H^1(\Lambda_i) = \bigcup_{i=1}^{N} V_{v,i} \qquad \text{and} \qquad q_v = \bigcup_{i=1}^{N} L^2(\Lambda_i)$$

In order to deduce the weak formulation of the vessel problem we multiply the third equation of (1.22) by a test function $q_v \in Q_v$. Using the linearity of the integral we define the following simplified notation for the scalar product L^2 on the network domain and we will rewrite the integral over the whole network as a summation of integrals over single branches:

$$\int_{\Lambda} (\cdot) = \sum_i \int_{\Lambda_i} (\cdot)_i. \tag{1.41}$$

Let us assume the vessels radius to be a step function of the arc length s assuming constant values over the $(d-2)-$dimensional varieties Λ_i:

$$\mathrm{R}(s) = \sum_{i}^{N} \mathrm{R}_i \delta_{\Lambda_i}(s), \tag{1.42}$$

being δ_{Λ_i} the Dirac delta function of the $i-th$ branch.

Let $q_v|_{\mathcal{K}_j}$ be the uniquely defined value of q_v at the location of the j-th junction. We weakly enforce the flow rate compatibility constraints at the junctions, by multiplying the fifth equation of (1.22) by $q_v|_{\mathcal{K}_j}$ and we add it to the third equation. In this way, we obtain the third equation of (1.39). To derive the last equation of (1.39), we multiply the fourth equation of (1.22) by a test function $v_{v,i} \in V_{v,i} = H^1(\Lambda_i)$ and by $\pi \mathrm{R}_i^2$. Then, we sum the contribution of each branch of the network.

$$\sum_i \int_{\Lambda_i} \partial_s\big(\bar{u}_{v,i}(s)\big) q_v(s) ds + \sum_i \int_{\Lambda_i} \frac{Q}{2\pi \mathrm{R}_i'^2} ((\bar{p}_v - \bar{\bar{p}}_t) - \sigma(\pi_v - \pi_t)) q_v(s) ds = \\ = 0 \tag{1.43}$$

$$\sum_i \int_{\Lambda_i} \frac{\pi^2 \mathrm{R}_i'^4}{k_v}\big(1+\kappa_i'^2(s)\mathrm{R}_i'^2(s)\big)\bar{u}_{v,i}(s)v_{v,i}(s)ds + \sum_i \int_{\Lambda_i} \pi \mathrm{R}_i'^2 \partial_s \bar{p}_{v,i}(s)v_{v,i}(s)ds = 0 \tag{1.44}$$

Moreover, using again Green's formula, we transfer the spatial derivative from the pressure to the test function, as follows,

$$\sum_i \int_{\Lambda_i} \pi \mathrm{R}_i^2 \partial_s \bar{p}_{v,i} v_{v,i} = -\sum_i \int_{\Lambda_i} \bar{p}_{v,i}\partial_s(\pi R_i^2 v_{v,i}) + \sum_i \left[\bar{p}_{v,i}\pi R_i^2 v_{v,i}|_{s=L} - \bar{p}_{v,i}\pi R_i^2 v_{v,i}|_{s=0}\right].$$

At this point, we re-organize the local boundary terms in order to collect contributions of different branches affecting the same junction point and using the continuity of the pressure. Reminding the indexes defined previously we characterize the junctions that ends inside the interstitial space with $\mathcal{E}$ and the one intersecting the boundary with $\mathcal{B}$, obtaining:

$$\begin{aligned}\sum_i \left[\bar{p}_{v,i}\pi R_i^2 v_{v,i}|_{s=L} - \bar{p}_{v,i}\pi R_i^2 v_{v,i}|_{s=0}\right] = \\ = \sum_j \bar{p}_v|_{\mathbf{y}_j}\left[\sum_{i\in\mathcal{K}_j^+} \pi R_i^2 v_{v,i}|_{\mathbf{y}_j} - \sum_{i\in\mathcal{K}_j^-} \pi R_i^2 v_{v,i}|_{\mathbf{y}_j}\right] + \\ + \sum_{i\in\mathcal{B}}\left[\bar{p}_v\,\pi R_i^2 v_v|_{\mathbf{x}_i^+} - \bar{p}_v\,\pi R_i^2 v_v|_{\mathbf{x}_i^-}\right] + \sum_{i\in\mathcal{E}} \bar{p}_v\,\pi R_i^2 v_v|_{\mathbf{z}_i^+}\,.\end{aligned}$$

For the sake of simplicity, we also implicitly assumed that boundary points and bifurcation or branching points can not coincide, this only allows us to avoid further indexes.

The last step is to enforce suitable boundary conditions at the vessels tips. However we first need to highlight a characteristic of the pressure. We implicitly assumed the trace of $(p_v v_v)$ over Λ_i, exists for v_v smooth enough, i.e. the evaluation of the product at a boundary point makes sense. Furthermore, in order to deduce the mass conservation constrain, we shall write $(p_v v_v)(s_j) = p_v(s_j)v_v(s_j)$ for some extreme point $s_j \in \Lambda$. Obviously, a general L^2 function is not appropriate because one can not evaluate its punctual values; we need to require more regularity, this is why the natural choice is $p_v \in C^0(\bar{\Lambda})$.

After this manipulation, adding this last term to (1.44) we obtain:

$$\sum_i \int_{\Lambda_i} \frac{\pi^2 \mathrm{R}_i'^4}{k_v}\big(1+\kappa_i'^2(s)\mathrm{R}_i'^2(s)\big)\bar{u}_{v,i}(s)v_{v,i}(s)ds - \sum_i \int_{\Lambda_i} \bar{p}_{v,i}\partial_s(\pi \mathrm{R}_i^2 v_{v,i}) + \\ + \sum_j \bar{p}_v|_{\mathbf{y}_j}\left[\sum_{i\in\mathcal{K}_j^+} \pi R_i^2 v_{v,i}|_{\mathbf{y}_j} - \sum_{i\in\mathcal{K}_j^-} \pi R_i^2 v_{v,i}|_{\mathbf{y}_j}\right] + \\ + \sum_{i\in\mathcal{B}}\Big[\bar{p}_v\,\pi R_i^2 v_v|_{\mathbf{x}_i^+} - \bar{p}_v\,\pi R_i^2 v_v|_{\mathbf{x}_i^-}\Big] + \sum_{i\in\mathcal{E}} \bar{p}_v\,\pi R_i^2 v_v|_{\mathbf{z}_i^+} = 0 \tag{1.45}$$

We reach a term that looks like the weak mass conservation constraint (written for the generic test function v_v). It is now explained why we pre-multiplied the vessels problem with the function $\pi \mathrm{R}_i^2$. In fact, thanks to that trick, the desired constraint come to light in a natural way. The conservation of local flow rate at vessel junctions can be indeed expressed in terms of the above notation as follows:

$$\sum_{i\in\mathcal{K}_j^+} \pi R_i^2 u_{v,i}|_{\mathbf{y}_j} - \sum_{i\in\mathcal{K}_j^-} \pi R_i^2 u_{v,i}|_{\mathbf{y}_j}, \qquad j=1,...,M \tag{1.46}$$

In order to weakly enforce (1.46) in (1.43) we write the variational formulation by multiplying it with the pressure test function q_v and we add this null term to the equation, namely:

$$\sum_j \left[\sum_{i\in\mathcal{K}_j^+} \pi R_i^2 u_{v,i}|_{\mathbf{y}_j} - \sum_{i\in\mathcal{K}_j^-} \pi R_i^2 u_{v,i}|_{\mathbf{y}_j}\right] q_v(s_j), \qquad j=1,...,M \tag{1.47}$$

$$\sum_i \int_{\Lambda_i} \partial_s\big(\bar{u}_{v,i}(s)\big)q_v(s)ds + \sum_i \int_{\Lambda_i} \frac{Q}{2\pi \mathrm{R}_i'^2}((\bar{p}_v - \bar{\bar{p}}_t) - \sigma(\pi_v - \pi_t))q_v(s)ds - \\ - \sum_j \left[\sum_{i\in\mathcal{K}_j^+} \pi R_i^2 u_{v,i}|_{\mathbf{y}_j} - \sum_{i\in\mathcal{K}_j^-} \pi R_i^2 u_{v,i}|_{\mathbf{y}_j}\right] q_v(s_j) = 0 \tag{1.48}$$

Finally we can represent the vessel problem weak formulation as follows:

$$\sum_i \int_{\Lambda_i} \partial_s\big(\bar{u}_{v,i}(s)\big) q_v(s) ds + \sum_i \int_{\Lambda_i} \frac{Q}{2\pi \mathrm{R}_i'^2}((\bar{p}_v - \bar{\bar{p}}_t) - \sigma(\pi_v - \pi_t)) q_v(s) ds - \\ - \sum_j \left[\sum_{i \in \mathcal{K}_j^+} \pi R_i^2 u_{v,i}|_{\mathbf{y}_j} - \sum_{i \in \mathcal{K}_j^-} \pi R_i^2 u_{v,i}|_{\mathbf{y}_j} \right] q_v(s_j) = 0 \qquad \forall q_v \in Q_v, \tag{1.49}$$

$$\sum_i \int_{\Lambda_i} \frac{\pi^2 \mathrm{R}_i'^4}{k_v}\big(1 + \kappa_i'^2(s)\mathrm{R}_i'^2(s)\big)\bar{u}_{v,i}(s) v_{v,i}(s) ds - \sum_i \int_{\Lambda_i} \bar{p}_{v,i} \partial_s(\pi \mathrm{R}_i^2 v_{v,i}) + \\ + \sum_j \bar{p}_v|_{\mathbf{y}_j} \left[\sum_{i \in \mathcal{K}_j^+} \pi R_i^2 v_{v,i}|_{\mathbf{y}_j} - \sum_{i \in \mathcal{K}_j^-} \pi R_i^2 v_{v,i}|_{\mathbf{y}_j} \right] + \tag{1.50}$$
$$+ \sum_{i \in \mathcal{B}} \Big[\bar{p}_v \, \pi R_i^2 v_v|_{\mathbf{x}_i^+} - \bar{p}_v \, \pi R_i^2 v_v|_{\mathbf{x}_i^-} \Big] + \sum_{i \in \mathcal{E}} \bar{p}_v \, \pi R_i^2 v_v|_{\mathbf{z}_i^+} = 0 \qquad \forall v_v \in V_v.$$

Let now close our problem including suitable boundary condition at the network extrema. We split the set of boundary ends $\mathcal{B}$, where we enforce a pressure value, in boundary data input and output, $\mathcal{B}_{in}$ and $\mathcal{B}_{out}$ respectively. In out case we will always enforce a constant pressure drop $\Delta P_v = P_v^{out} P_v^{in}$, that means we will adopt piecewise-constant boundary data, the dimensionless one, namely:

$$g_v(s) = \begin{Bmatrix} P_v^{out} = g_v^- & s \in \mathcal{B}_{out} \\ P_v^{in} = g_v^+ & s \in \mathcal{B}_{in} \end{Bmatrix}.$$

We have to remind that we are considering the mixed formulation of the problem, so we enforce in a weak natural way the pressure boundary condition, while we need to enforce directly the essential condition on the dead ends. Similarly to what we have done for the tissue, we can rewrite as

$$p_v = p_0 + \frac{\pi \mathrm{R}'^2}{\beta_v} u_v \qquad on \quad \mathcal{E}. \tag{1.51}$$

Adding this last two condition the final weak-formulation for the vessel become:

$$\sum_i \int_{\Lambda_i} \partial_s\big(\bar{u}_{v,i}(s)\big) q_v(s) ds + \sum_i \int_{\Lambda_i} \frac{Q}{2\pi \mathrm{R}_i'^2}((\bar{p}_v - \bar{\bar{p}}_t) - \sigma(\pi_v - \pi_t)) q_v(s) ds - \\ - \sum_j \left[\sum_{i \in \mathcal{K}_j^+} \pi R_i^2 u_{v,i}|_{\mathbf{y}_j} - \sum_{i \in \mathcal{K}_j^-} \pi R_i^2 u_{v,i}|_{\mathbf{y}_j} \right] q_v(s_j) = 0 \qquad \forall q_v \in Q_v, \tag{1.52}$$

$$\sum_i \int_{\Lambda_i} \frac{\pi^2 \mathrm{R}_i'^4}{k_v} \big(1 + \kappa_i'^2(s) \mathrm{R}_i'^2(s)\big) \bar{u}_{v,i}(s) v_{v,i}(s) ds - \sum_i \int_{\Lambda_i} \bar{p}_{v,i} \partial_s(\pi \mathrm{R}_i^2 v_{v,i}) + \\ + \sum_j \bar{p}_v|_{\mathbf{y}_j} \left[\sum_{i \in \mathcal{K}_j^+} \pi \mathrm{R}_i^2 v_{v,i}|_{\mathbf{y}_j} - \sum_{i \in \mathcal{K}_j^-} \pi \mathrm{R}_i^2 v_{v,i}|_{\mathbf{y}_j} \right] + \\ + \sum_{i \in \mathcal{E}} \frac{1}{\beta_v} \pi^2 \mathrm{R}_i^4 \bar{u}_{v,i}|_{\mathbf{z}_i^+} v_v|_{\mathbf{z}_i^+} = \\ = - \sum_{i \in \mathcal{B}} \Big[g_v^+ \pi R_i^2 v_v|_{\mathbf{x}_i^+} - g_v^- \pi \mathrm{R}_i^2 v_v|_{\mathbf{x}_i^-} \Big] - \sum_{i \in \mathcal{E}} \pi \mathrm{R}_i^2 p_0 v_v|_{\mathbf{z}_i^+} \qquad \forall v_v \in V_v. \tag{1.53}$$

1.8.3 Coupled tissue-vessels weak formulation

Let combine now all the previous equation in a unified weak formulation for our model of fluid exchange between microcirculation and tissue interstitium. The coupled variational formulation becomes:

$$\text{Find} \qquad \mathbf{u}_t \in \mathbf{V}_t,\ p_t \in Q_t,\ u_v \in V_v,\ p_v \in Q_v \qquad \text{s.t.}$$

$$
\begin{cases}
\int_\Omega \frac{1}{k_t}\mathbf{u}_t\cdot\mathbf{v}_t d\Omega + \frac{1}{\beta_t}\int_{\Gamma_u}(\mathbf{u}_t\cdot\mathbf{n})(\mathbf{v}_t\cdot\mathbf{n})d\sigma - \int_\Omega div(\mathbf{v}_t)p_t d\Omega = & \\
\quad = -\int_{\Gamma_p} g_t\mathbf{v}_t\cdot\mathbf{n}d\sigma - \int_{\Gamma_u} p_0\mathbf{v}_t\cdot\mathbf{n}d\sigma & \forall q_t\in Q_t,\\
\int_\Omega(\nabla\cdot\mathbf{u}_t)q_t d\Omega - \int_\Omega Q((\bar{p}_v-\bar{\bar{p}}_t)-\sigma(\pi_v-\pi_t))\delta_\Lambda q_t d\Omega = 0 & \forall\mathbf{v}_t\in\mathbf{V}_t,\\
\sum_i\int_{\Lambda_i}\partial_s\big(\bar{u}_{v,i}(s)\big)q_v(s)ds + \sum_i\int_{\Lambda_i}\frac{Q}{2\pi \mathrm{R}_i'^2}((\bar{p}_v-\bar{\bar{p}}_t)-\sigma(\pi_v-\pi_t))q_v(s)ds- & \\
\quad -\sum_j\left[\sum_{i\in\mathcal{K}_j^+}\pi R_i^2 u_{v,i}|_{\mathbf{y}_j} - \sum_{i\in\mathcal{K}_j^-}\pi R_i^2 u_{v,i}|_{\mathbf{y}_j}\right]q_v(s_j) = 0 & \forall q_v\in Q_v,\\
\sum_i\int_{\Lambda_i}\frac{\pi^2\mathrm{R}_i'^4}{k_v}\big(1+\kappa_i'^2(s)\mathrm{R}_i'^2(s)\big)\bar{u}_{v,i}(s)v_{v,i}(s)ds - \sum_i\int_{\Lambda_i}\bar{p}_{v,i}\partial_s(\pi\mathrm{R}_i^2 v_{v,i})+ & \\
\quad +\sum_j\bar{p}_v|_{\mathbf{y}_j}\left[\sum_{i\in\mathcal{K}_j^+}\pi\mathrm{R}_i^2 v_{v,i}|_{\mathbf{y}_j} - \sum_{i\in\mathcal{K}_j^-}\pi\mathrm{R}_i^2 v_{v,i}|_{\mathbf{y}_j}\right]+ & \\
\quad +\sum_{i\in\mathcal{E}}\frac{1}{\beta_v}\pi^2\mathrm{R}_i^4\bar{u}_{v,i}|_{\mathbf{z}_i^+}v_v|_{\mathbf{z}_i^+} = & \\
\quad = -\sum_{i\in\mathcal{B}}\left[g_v^+\pi R_i^2 v_v|_{\mathbf{x}_i^+} - g_v^-\pi\mathrm{R}_i^2 v_v|_{\mathbf{x}_i^-}\right] - \sum_{i\in\mathcal{E}}\pi\mathrm{R}_i^2 p_0 v_v|_{\mathbf{z}_i^+} & \forall v_v\in V_v.
\end{cases}
\tag{1.54}
$$

The prove of the well-poseness of this problem and the demonstration of existence, uniqueness and regularity of the exact solution of problem (1.54) have already been addressed for a similar problem setting by [18]. This is a non standard analysis due to the presence of the concentrated mass term δ_Λ,anyway it is possible to reformulate the weak form in such a way to avoid the use of the Dirac mass source and prove the well-possess using the standard Lax-Milgram Theory (see [18]).

1.8.4 Weak-formulation of the hematocrit transport problem

For hematocrit transport problem, as for the pressure-velocity problem in the network, we required a certain regularity for the hematocrit in every vessel separately, namely $H_T = \bigcup_{i=1}^N H^1(\Lambda_i)$. Then starting from the strong form, we multiply the governing equation (1.28) by a test function $w_i \in H^1(\Lambda_i)$ and we integrate over all the domain Λ. We use again the linearity of the integral to rewrite the integral on all Λ as sum of the integral on every branch.

$$\int_{\Lambda} \frac{\partial(\pi \mathrm{R}'^2 \bar{u}_v H)}{\partial s} \omega ds \;=\; \sum_i \int_{\Lambda_i} \frac{\partial(\pi \mathrm{R}_i'^2 \bar{u}_{v,i} H_i)}{\partial s} \omega ds \;=\; 0 \tag{1.55}$$

We first highlight that hematocrit is considered as velocity for the vessels problem, it can be discontinuous at every junction. Then, we use Green's formula to transfer the derivative from H_i to w_i and we sum over the branches. In this way we obtain the following expression,

$$\begin{aligned}
&\sum_i \int_{\Lambda_i} \partial_s(\pi R_i^2 \bar{u}_{v,i} H_i) w_i = \\
&\quad = -\sum_i \int_{\Lambda_i} \pi R_i^2 \bar{u}_{v,i} H_i \partial_s w_i + \sum_i \left[\pi R_i^2 \bar{u}_{v,i} H_i w_i|_{s=L} - \pi R_i^2 \bar{u}_{v,i} H_i w_i|_{s=0}\right].
\end{aligned}$$

Then, we rearrange the last term of the previous equation junction by junction, as well as we isolate the terms on the boundary and on the dead ends,

$$\begin{aligned}
&+\sum_i \left[\pi R_i^2 \bar{u}_{v,i} H_i w_i|_{s=L} - \pi R_i^2 \bar{u}_{v,i} H_i w_i|_{s=0}\right] = \\
&\qquad = \sum_j \left[\sum_{i \in \mathcal{K}_j^{out}} \pi R_i^2 \bar{u}_{v,i} H_i w_i|_{\mathbf{y}_j} - \sum_{i \in \mathcal{K}_j^{in}} \pi R_i^2 \bar{u}_{v,i} H_i w_i|_{\mathbf{y}_j} \right] \\
&\qquad + \sum_{i \in \mathcal{B}} \left[\pi R_i^2 \bar{u}_{v,i} H_i w_i|_{\mathbf{x}_i^{out}} - \pi R_i^2 \bar{u}_{v,i} H_i w_i|_{\mathbf{x}_i^{in}}\right] + \sum_{i \in \mathcal{E}} \pi R_i^2 \bar{u}_{v,i} H_i w_i|_{\mathbf{z}_i^+}
\end{aligned} \tag{1.56}$$

Using the previous expression, we enforce the mass balance of hematocrit at the network junctions and the boundary conditions. For this purpose we define the following quantities for the j-th junction. The blood flow split relative to all the inflow branches is,

$$F_{QB,j,i} = \frac{\pi R_i^2 \bar{u}_{v,i}|_{\mathbf{y}_j}}{\sum_{i \in \mathcal{K}_j^{out}} \pi R_i^2 \bar{u}_{v,i}|_{\mathbf{y}_j}}, \quad \forall\, i \in \mathcal{K}_j^{in},$$

and let $F_{QE,j,i}$ be the corresponding split of discharge hematocrit,

$$\begin{cases} F_{QE,j,i} = 1 & if\ \text{card}(\mathcal{K}_j^{in}) = 1; \\ F_{QE,j,i} = 0 & if\ \text{card}(\mathcal{K}_j^{in}) = 2 \ \wedge\ F_{QB,j,i} \leq X_0; \\ logit(F_{QE,j,i}) = A + Blogit(\frac{F_{QB,j,i}-X_0}{1-2X_0}) & if\ \text{card}(\mathcal{K}_j^{in}) = 2 \ \wedge\ X_0 < F_{QB,j,i} < 1 - X_0; \\ F_{QE,j,i} = 1 & if\ \text{card}(\mathcal{K}_j^{in}) = 2 \ \wedge\ F_{QB,j,i} \geq 1 - X_0. \end{cases} \tag{1.57}$$

As a consequence of these definitions, the discharge hematocrit entering each branch downstream the j-th junction is,

$$\pi R_i^2 \bar{u}_{v,i} H_i|_{\mathbf{y}_j} = F_{QE,j,i} \sum_{i \in \mathcal{K}_j^{out}} \pi R_i^2 \bar{u}_{v,i} H_i|_{\mathbf{y}_j}.$$

We weakly enforce the hematocrit split conditions in the variational formulation as follows,

$$\sum_{i \in \mathcal{K}_j^{in}} \pi R_i^2 \bar{u}_{v,i} H_i w_i|_{\mathbf{y}_j} = \sum_{i \in \mathcal{K}_j^{in}} F_{QE,j,i} w_i|_{\mathbf{y}_j} \left(\sum_{i \in \mathcal{K}_j^{out}} \pi R_i^2 \bar{u}_{v,i} H_i|_{\mathbf{y}_j} \right).$$

We also enforce the boundary conditions for hematocrit at the boundary of the network,

$$\pi R_i^2 \bar{u}_{v,i} H_i w_i|_{\mathbf{x}_i^{in}} = \pi R_i^2 \bar{u}_{v,i} H_0 w_i|_{\mathbf{x}_i^{in}}.$$

Substituting, for clarity, these terms into (1.56), we obtain,

$$\begin{aligned} &+ \sum_i \left[\pi R_i^2 \bar{u}_{v,i} H_i w_i|_{s=L} - \pi R_i^2 \bar{u}_{v,i} H_i w_i|_{s=0} \right] \\ &\quad = \sum_j \sum_{i \in \mathcal{K}^{out}} \pi R_i^2 \bar{u}_{v,i} H_i w_i|_{\mathbf{y}_j} + \sum_{i \in \mathcal{B}} \pi R_i^2 \bar{u}_{v,i} H_i w_i|_{\mathbf{x}_i^{out}} + \sum_{i \in \mathcal{E}} \pi R_i^2 \bar{u}_{v,i} H_i w_i|_{\mathbf{z}_i^+} \\ &\qquad - \sum_j \sum_{i \in \mathcal{K}_j^{in}} F_{QE,j,i} w_i|_{\mathbf{y}_j} \left(\sum_{i \in \mathcal{K}_j^{out}} \pi R_i^2 \bar{u}_{v,i} H_i|_{\mathbf{y}_j} \right) - \sum_j \sum_{i \in \mathcal{B}} \pi R_i^2 \bar{u}_{v,i} H_0 w_i|_{\mathbf{x}_i^{in}}. \end{aligned}$$

Consequently, the variational formulation of the hematocrit governing equation

reads as follows,

$$
\begin{aligned}
-\sum_i \int_{\Lambda_i} \pi R_i^2 \bar{u}_{v,i} H_i \partial_s w_i + \sum_j \sum_{i \in \mathcal{K}^{out}} \pi R_i^2 \bar{u}_{v,i} H_i w_i|_{\mathbf{y}_j} + \sum_{i \in \mathcal{B}} \pi R_i^2 \bar{u}_{v,i} H_i w_i|_{\mathbf{x}_i^{out}} \\
+ \sum_{i \in \mathcal{E}} \pi R_i^2 \bar{u}_{v,i} H_i w_i|_{\mathbf{z}_i^+} - \sum_j \sum_{i \in \mathcal{K}_j^{in}} F_{QE,j,i} w_i|_{\mathbf{y}_j} \left(\sum_{i \in \mathcal{K}_j^{out}} \pi R_i^2 \bar{u}_{v,i} H_i|_{\_j} \right) \\
= \sum_j \sum_{i \in \mathcal{B}} \pi R_i^2 \bar{u}_{v,i} H_0 w_i|_{\mathbf{x}_i^{in}} \qquad \forall w_i \in H^1(\Lambda_i)\,. \quad (1.58)
\end{aligned}
$$

1.9 Numerical approximation

The next step is to derive the discretization of the problem. To do that we use the finite element approximation technique, combined with a discretization of the domain. In our case the partitions of Ω and Λ are completely independent, this is one of the advantage of our formulation. Therefore, we can define two discrete approximation separately.

1.9.1 Discretization of tissue problem

We first state Ω to be a polygonal domain, where we define τ_t^h an admissible family of partitions of $\bar{\Omega}$ into tetrahedrons K

$$\bar{\Omega} = \bigcup_{K \in \tau_t^h} K,$$

that satisfies the usual conditions of a conforming triangulation of Ω.
We denote with h the characteristic mesh size, $h = \max_{K \in \tau_t^h} k_K$, being h_K the diameter of simplex K. The solution of (1.54)(a),(b) is approximated using discontinuous piecewise-polynomial finite elements for the pressure and $\mathbf{H}^{div}$-conforming *Raviart-Thomas* finite elements (RT) for velocity, namely

$$Y_k^h := \{v_h \in L^2(\Omega),\ v_h|_K \in P_k(K) \quad \forall K \in \tau_t^h\}, \quad (1.59)$$

$$RT_k^h := \{\mathbf{w}_h \in H_{div}(\Omega),\ \mathbf{w}_h|_K \in P_k(K; \mathbb{R}^d) \oplus \mathbf{x}\, P_k(K) \quad \forall K \in \tau_t^h\}, \quad (1.60)$$

where P_k represent the standard polynomials space od degree $\leq k$, for every $k \geq 0$, inn the variable $\mathbf{x} = (x_1, \ldots, x_d)$. In our problem we are going to use the lowest

order *Raviart-Thomas* approximation, corresponding to $k = 0$.

1.9.2 Discretization of capillary network problem

For the capillary network we adopt the same separation technique introduced at the continuous level, obtaining the following discretized domain:

$$\Lambda_h = \bigcup_{i=1}^{N} \Lambda_i^h \,.$$

This means that each curved branch Λ_i is approximated by a piecewise linear 1D line, denoted with Λ_i^h, that is, more precisely, a partition of the i-th network branch made by a sufficiently large number of segments.
The solution for the vessels problem is approximated using continuous piecewise-polynomial finite element spaces for pressure, but not for velocity. Since we want the vessel velocity to be discontinuous at multiple junctions, we define the related finite element space over the whole network as the collection of the local spaces of the single branches. Conversely the pressure has been assumed to be continuous over the network, therefore its finite element approximation is standard. We will use the following families of finite element spaces for pressure and velocity, respectively:

$$X_{k+1}^h(\Lambda) := \{w_h \in C^0(\bar{\Lambda}) w_h|_S \in P_{k+1}(S) \quad \forall S \in \Lambda^h\}, \tag{1.61}$$

$$W_{k+2}^h(\Lambda) := \bigcup_{i=1}^{N} X_h^{k+2}\left(\Lambda_i^h\right), \tag{1.62}$$

for every integer $k \geq 0$. We use generalized *Taylor-Hood* elements on each branch, this implies that on every branch is satisfied the local stability of the mixed finite element pair. Regarding the pressure instead, we guarantee its continuity over the entire network. As for the tissue discretization, we have used the lowest order, that is $k = 0$.

1.9.3 Discretization of hematocrit transport problem

As for the fluid dynamics problem, for the hematocrit discretization we proceed as for the velocity approximation on the vessels, since the both are discontinuous at

multiple junctions. We consider discrete functional subspaces of $H_T = \bigcup_{i=1}^{N} H^1(\Lambda_i)$ for $k \geq 0$, namely:

$$H_T^h \;=\; W_{k+2}^h(\Lambda) := \bigcup_{i=1}^{N} X_h^{k+2}\left(\Lambda_i^h\right) \tag{1.63}$$

1.9.4 Discrete coupled tissue-network and hematocrit transport problem

The discrete formulation can be easily deduced from the weak-formulation of the full fluid and hematocrit problem projecting the equation and the solution on the discrete subspace defined previously, adding the subscript h. First of all, let us define the following discrete functional subspaces for $k \geq 0$:

$$\begin{aligned}
&\mathbf{V}_t^h = RT_k^h(\Omega) \quad \text{and} \quad Q_t^h = Y_k^h(\Omega)\ , \\
&V_v^h = W_{k+2}^h(\Lambda^h) \quad \text{and} \quad Q_v^h = X_{k+1}^h(\Lambda^h) \quad \text{and} \quad W_v^h = W_{k+2}^h(\Lambda^h)\,.
\end{aligned}$$

Before to introduce the discrete equations, we specify the following notation for the inner product in out functional spaces, in order to simplify our notation:

$$\int_\Omega (\,\cdot\,)\, d\Omega \;=\; (\,\cdot\,,\,\cdot\,)_\Omega \qquad \int_\Lambda (\,\cdot\,)\, ds \;=\; (\,\cdot\,,\,\cdot\,)_\Lambda$$

We can now propose the discretized weak formulation for all the problem as follows:

find $\mathbf{u}_t^h \in \mathbf{V}_t^h$, $p_t^h \in Q_t^h$, $u_v^h \in V_v^h$, $p_v^h \in Q_v^h$, $H^h \in W_v^h$ such that

$$
\begin{cases}
(\frac{1}{k_t}\mathbf{u}_t\,,\,\mathbf{v}_t)_\Omega + \frac{1}{\beta_t}(\mathbf{u}_t\cdot\mathbf{n}\,,\,\mathbf{v}_t\cdot\mathbf{n})_{\Gamma_u} - (p_t\,,\,\nabla\cdot\mathbf{v}_t)_\Omega = \\
\qquad = -(g_t\,,\,\mathbf{v}_t\cdot\mathbf{n})_{\Gamma_p} - (p_0\,,\,\mathbf{v}_t\cdot\mathbf{n})_{\Gamma_u} & \forall \mathbf{v}_t \in \mathbf{V}_t, \\
(\nabla\cdot\mathbf{u}_t\,,\,q_t)_\Omega - (Q((\bar{p}_v-\bar{\bar{p}}_t)-\sigma(\pi_v-\pi_t))\delta_\Lambda\,,\,q_t)_\Omega = 0 & \forall q_t \in Q_t, \\
(\frac{\pi^2\mathrm{R}_i'^4}{k_v}\big(1+\kappa_i'^2(s)\mathrm{R}_i'^2(s)\big)\bar{u}_{v,i}(s)\,,\,v_{v,i}(s))_\Lambda - (\bar{p}_{v,i}\,,\,\partial_s(\pi\mathrm{R}_i^2 v_{v,i}))_\Lambda + \\
\qquad + \sum_j \bar{p}_v|_{\mathbf{y}_j}\Big[\sum_{i\in\mathcal{K}_j^+}\pi\mathrm{R}_i^2 v_{v,i}|_{\mathbf{y}_j} - \sum_{i\in\mathcal{K}_j^-}\pi\mathrm{R}_i^2 v_{v,i}|_{\mathbf{y}_j}\Big] + \\
\qquad + \Big[\frac{1}{\beta_v}\pi^2\mathrm{R}^4\bar{u}_v v_v\Big]_\mathcal{E} = \\
\qquad = -\sum_{i\in\mathcal{B}}\Big[\,g_v^+\,\pi R_i^2 v_v|_{\mathbf{x}_i^+} - g_v^-\,\pi\mathrm{R}_i^2 v_v|_{\mathbf{x}_i^-}\Big] - [\,\pi\mathrm{R}^2 p_0 v_v]_\mathcal{E} & \forall v_v \in V_v \\
(\partial_s\big(\bar{u}_{v,i}(s)\big)\,,\,q_v(s))_\Lambda + (\frac{Q}{2\pi\mathrm{R}_i'^2}((\bar{p}_v-\bar{\bar{p}}_t)-\sigma(\pi_v-\pi_t))\,,\,q_v(s))_\Lambda - \\
\qquad - \sum_j\Big[\sum_{i\in\mathcal{K}_j^+}\pi R_i^2\bar{u}_{v,i}|_{\mathbf{y}_j} - \sum_{i\in\mathcal{K}_j^-}\pi R_i^2\bar{u}_{v,i}|_{\mathbf{y}_j}\Big]q_v(s_j) = 0 & \forall q_v \in Q_v, \\
-(\pi R_i^2\bar{u}_{v,i}H_i\,,\,\partial_s w_i)_\Lambda + \sum_j\sum_{i\in\mathcal{K}^{out}}\pi R_i^2\bar{u}_{v,i}H_i w_i|_{\mathbf{y}_j} + \sum_{i\in\mathcal{B}}\pi R_i^2\bar{u}_{v,i}H_i w_i|_{\mathbf{x}_i^{out}} \\
\qquad + [\pi\mathrm{R}^2\bar{u}_v H w]_\mathcal{E} - \sum_j\sum_{i\in\mathcal{K}_j^{in}}F_{QE,j,i}w_i|_{\mathbf{y}_j}\Big(\sum_{i\in\mathcal{K}_j^{out}}\pi R_i^2\bar{u}_{v,i}H_i|_{-j}\Big) = \\
\qquad \sum_j\sum_{i\in\mathcal{B}}\pi R_i^2\bar{u}_{v,i}H_0 w_i|_{\mathbf{x}_i^{in}} & \forall w_i \in W_v^h
\end{cases}
\tag{1.64}
$$

1.9.5 Algebraic formulation

At this point we can derive the algebraic form of the discretized problem. Let first define the degree of freedom for the finite element spaces:

$$
\begin{aligned}
N_t^h &:= \dim\left(\mathbf{V}_t^h\right), \qquad & M_t^h &:= \dim\left(Q_t^h\right) \\
N_v^h &:= \dim\left(V_v^h\right), \qquad & M_v^h &:= \dim\left(Q_v^h\right) \\
& & S_v^h &:= \dim\left(W_v^h\right)
\end{aligned}
\tag{1.65}
$$

Since the tissue 3D and the vessel 1D meshes are independent, we can define three self-governing sets, containing respectively the finite element basis for $\mathbf{V}_t^h \times Q_t^h$, $V_v^h \times Q_v^h$ and W_v^h:

$$\left\{\boldsymbol{\varphi}_t^i\right\}_{i=1}^{N_t^h} \times \left\{\psi_t^i\right\}_{i=1}^{M_t^h}, \qquad \left\{\varphi_v^i\right\}_{i=1}^{N_v^h} \times \left\{\psi_v^i\right\}_{i=1}^{M_v^h}, \qquad \left\{\phi_v^i\right\}_{i=1}^{S_v^h} \times \left\{\varphi_v^i\right\}_{i=1}^{N_v^h}. \quad (1.66)$$

Using this bases, we can express our variables as linear combination of the basis' elements as follows:

$$\begin{aligned} \mathbf{u}_t^h(\mathbf{x}) &= \sum_{i=1}^{N_t^h} U_t^i \, \boldsymbol{\varphi}_t^i(\mathbf{x}), \qquad p_t^h(\mathbf{x}) = \sum_{i=1}^{M_t^h} P_t^i \, \psi_t^i(\mathbf{x}), \qquad \forall \mathbf{x} \in \Omega \\ u_v^h(s) &= \sum_{i=1}^{N_v^h} U_v^i \, \varphi_v^i(s), \qquad p_v^h(s) = \sum_{i=1}^{M_v^h} P_v^i \, \psi_v^i(s), \qquad \forall s \in \Lambda \\ H^h(s) &= \sum_{i=1}^{S_v^h} H_v^i \, \phi_v^i(s), \qquad \forall s \in \Lambda \end{aligned} \quad (1.67)$$

being $\mathbf{U}_t = \{U_t^i\}_{i=1}^{N_t^h}$, $P_t = \{P_t^i\}_{i=1}^{M_t^h}$, $U_v = \{U_v^i\}_{i=1}^{N_v^h}$, $P_v = \{P_v^i\}_{i=1}^{M_v^h}$ and $H_v = \{H_v^i\}_{i=1}^{S_v^h}$ the vectors containing the degree of freedom of the finite elements approximations. Now using the linearity of the inner product, we can rewrite the weak formulation of the previous chapter in an algebraic formulation of the form:

$$\begin{bmatrix} \mathbb{M}_{tt} & -\mathbb{D}_{tt}^T & \mathbb{O} & \mathbb{O} \\ \mathbb{D}_{tt} & \mathbb{B}_{tt} & \mathbb{O} & -\mathbb{B}_{tv} \\ \mathbb{O} & \mathbb{O} & \mathbb{M}_{vv} & -\mathbb{D}_{vv}^T - \mathbb{J}_{vv}^T \\ \mathbb{O} & -\mathbb{B}_{vt} & \mathbb{D}_{vv} + \mathbb{J}_{vv} & \mathbb{B}_{vv} \end{bmatrix} \begin{bmatrix} \mathbf{U}_t \\ \mathbf{P}_t \\ \mathbf{U}_v \\ \mathbf{P}_v \end{bmatrix} = \begin{bmatrix} \mathbf{F}_t \\ -\mathbb{B}_{tt}\sigma\Delta\pi \\ \mathbf{F}_v \\ \mathbb{B}_{vv}\sigma\Delta\pi \end{bmatrix} \quad (1.68)$$

$$\begin{bmatrix} \mathbb{B}_h + \mathbb{J}_h + \mathbb{O}_h \end{bmatrix} \begin{bmatrix} \mathbf{H}_v \end{bmatrix} = \begin{bmatrix} \mathbf{F}_h \end{bmatrix} \quad (1.69)$$

For simplicity we introduced the notation $\langle \cdot, \cdot \rangle_J$ to indicate the junction therm of problem 1.64, that is the weak imposition of the mass conservation over each

junction, namely:

$$\langle u_v, q_v \rangle_J := \sum_j \left[\sum_{i \in \mathcal{K}_j^+} \pi R_i^2 u_{v,i}|_{\mathbf{y}_j} - \sum_{i \in \mathcal{K}_j^-} \pi R_i^2 u_{v,i}|_{\mathbf{y}_j} \right] q_v(s_j). \tag{1.70}$$

Then, the submatrix can be defined as follow:

$$[\mathbb{M}_{tt}]_{ij} := (\frac{1}{k_t}\boldsymbol{\varphi}_t^j, \boldsymbol{\varphi}_t^i)_\Omega + \frac{1}{\beta}(\boldsymbol{\varphi}_t^j \cdot \mathbf{n}, \boldsymbol{\varphi}_t^i \cdot \mathbf{n})_{\Gamma_u} \qquad \mathbb{M}_{tt} \in \mathbb{R}^{N_t^h \times N_t^h},$$

$$[\mathbb{D}_{tt}]_{ij} := (\nabla \cdot \boldsymbol{\varphi}_t^j, \psi_t^i)_\Omega \qquad \mathbb{D}_{tt} \in \mathbb{R}^{N_t^h \times M_t^h},$$

$$[\mathbb{B}_{tt}]_{ij} := (Q\overline{\overline{\psi}}_t^j \delta_{\Lambda_h}, \psi_t^i)_\Omega \qquad \mathbb{B}_{tt} \in \mathbb{R}^{M_t^h \times M_t^h},$$

$$[\mathbb{B}_{tv}]_{ij} := (Q\overline{\psi}_v^j \delta_{\Lambda_h}, \psi_t^i)_\Omega \qquad \mathbb{B}_{tv} \in \mathbb{R}^{M_t^h \times M_v^h},$$

$$[\mathbb{B}_{vt}]_{ij} := (Q\overline{\overline{\psi}}_t^j, \psi_v^i)_\Lambda \qquad \mathbb{B}_{vt} \in \mathbb{R}^{M_v^h \times M_t^h},$$

$$[\mathbb{B}_{vv}]_{ij} := (Q\overline{\psi}_v^j, \psi_v^i)_\Lambda \qquad \mathbb{B}_{vv} \in \mathbb{R}^{M_v^h \times M_v^h},$$

$$[\mathbb{M}_{vv}]_{ij} := (\frac{\pi^2 R'^4}{k_v}(1 + \kappa'^2 R'^2)\overline{\varphi}_v^j, \varphi_v^i) + \frac{1}{\beta_v}[\pi^2 R'^4 \varphi_v^j \varphi_v^i]_\varepsilon \qquad \mathbb{M}_{vv} \in \mathbb{R}^{N_v^h \times N_v^h},$$

$$[\mathbb{D}_{vv}]_{ij} := (\pi R'^2 \partial\overline{\varphi}_v^j, \psi_v^i)_\Lambda \qquad \mathbb{D}_{vv} \in \mathbb{R}^{N_v^h \times M_v^h},$$

$$[\mathbb{J}_{vv}]_{ij} := \langle \varphi_v^j, \overline{\psi}_v^i \rangle_J \qquad \mathbb{J}_{vv} \in \mathbb{R}^{N_v^h \times M_v^h},$$

$$[\mathbf{F}_t]_i := -(g_t^h, \boldsymbol{\varphi}_t^i \cdot \mathbf{n})_{\Gamma_p} - (p_0^h, \boldsymbol{\varphi}_t^i \cdot \mathbf{n})_{\Gamma_u} \qquad \mathbf{F}_t \in \mathbb{R}^{N_t^h},$$

$$[\mathbf{F}_v]_i := -[\pi R'^2 g_v \varphi_v^i]_\mathcal{B} - [\pi R'^2 p_0 \varphi_v^i]_\varepsilon \qquad \mathbf{F}_v \in \mathbb{R}^{N_v^h}$$

$$[\mathbb{B}_h]_{i,j} := (\, \pi R_i^2 \bar{u}_{v,p} \varphi^p \phi_j \,,\, \partial_s \phi_i \,)_\Lambda \qquad \mathbb{B}_h \in \mathbb{R}^{S_v^h}$$

$$[\mathbb{J}_h]_{i,j} := \langle \phi_v^j, \phi_v^i \rangle_J \qquad \mathbb{J}_h \in \mathbb{R}^{S_v^h}$$

$$[\mathbb{O}_h]_{i,j} := [\pi \mathrm{R}^2 \bar{u}_v^{out} \phi_h^j \phi_h^i]_\epsilon \qquad \mathbb{O}_h \in \mathbb{R}^{S_v^h}$$

$$[\mathbf{F}_h]_i := [\pi \mathrm{R}^2 \bar{u}_v^{in} H^0 \phi_h^i]_{\Lambda_{in}} \qquad \mathbf{F}_h \in \mathbb{R}^{S_v^h}$$

1.9.6 Solution strategy for the Nonlinear problem

To describe the iterative splitting strategy used to decouple 1.64 we define a shorthand notation. More precisely, let us group the first four equations of 1.64into the *fluid mechanics* operator $\mathcal{F}^h$. Given Ω, Λ^h, the external data g_t, g_v and the parameters for the porous medium K, μ_t the operator $\mathcal{F}^h$ takes as input the viscosity of the fluid μ_v as a function defined on Λ^h and gives back the solution of the fluid mechanics problem, namely $[\mathbf{u}_t^h, u_v^h, p_t^h, p_v^h] = \mathcal{F}^h(\mu_v)$. Similarly, the last equation of 1.64can be represented as the operator $\mathcal{H}^h$ such that, given the velocity field in the network u_v^h it gives back the hematocrit level at each point of Λ^h, precisely $H^h = \mathcal{H}^h(u_v^h)$. Using these operators and given an initial guess of the hematocrit distribution $H^{h,0}$, the iterative method to solve 1.64 consists of performing the following steps for any $k > 0$ until convergence:

1. calculate the apparent viscosity of blood, $\mu_{v,i}^k = \mu_{v,i}(H_i^{h,k-1})$;
2. solve the fluid mechanics problem $[\mathbf{u}_t^{h,*}, u_v^{h,*}, p_t^{h,k}, p_v^{h,k}] = \mathcal{F}^h(\mu_v^k)$;
3. apply relaxation of the velocity fields to enhance convergence,

$$\mathbf{u}_t^{h,k} = \alpha \mathbf{u}_t^{h,*} + (1-\alpha)\mathbf{u}_t^{h,k-1} \text{ and } \mathbf{u}_v^{h,k} = \alpha \mathbf{u}_v^{h,*} + (1-\alpha)\mathbf{u}_v^{h,k-1},\ \alpha \in (0,1];$$

4. solve the hematocrit problem $H^{h,*} = \mathcal{H}^h(u_v^{h,k})$;
5. apply relaxation $H^{h,k} = \beta H^{h,*} + (1-\beta)H^{h,k-1}$ with $\beta \in (0,1]$;
6. test convergence by means of the following indicators,

$$\frac{\left\|\mathbf{U}_v^{k+1} - \mathbf{U}_v^k\right\|}{\|\mathbf{U}_v^k\|} + \frac{\left\|\mathbf{p}_v^{k+1} - \mathbf{p}_v^k\right\|}{\|\mathbf{p}_v^k\|} + \frac{\left\|\mathbf{U}_t^{k+1} - \mathbf{U}_t^k\right\|}{\left\|\mathbf{U}_t^k\right\|} + \frac{\left\|\mathbf{p}_t^{k+1} - \mathbf{p}_t^k\right\|}{\left\|\mathbf{p}_t^k\right\|} < \epsilon_{\mathcal{F}}\,,$$

$$\frac{\left\|\mathbf{H}^{k+1} - \mathbf{H}^k\right\|}{\|\mathbf{H}^k\|} < \epsilon_{\mathcal{H}}$$

where $\epsilon_{\mathcal{F}}$, $\epsilon_{\mathcal{H}}$ is a fixed tolerance and $\mathbf{U}_t$, $\mathbf{U}_v$, $\mathbf{p}_t$, $\mathbf{p}_v$, $\mathbf{H}$ are the *degrees of freedom* that characterize the finite element functions $\mathbf{u}_t^h$, u_v^h, p_t^h, , $p_v^{h,k}$, H^h respectively.

Chapter 2

Review of strategies for the numerical solution of saddle point problems and Algebraic Multigrid Method

After the introduction of the problem in the previous chapter 1, we want to highlight the solution method for the linear system. Until this moment the method used to find the solution was a direct solver, namely *SuperLU*, which consist of decompose the non-singular matrix A, of our linear algebraic system, into the product LU where L and U are , respectively, a lower triangular and an upper triangular matrix. Direct method produce the exact solution in a finite number of steps (in the ideal absence of round-off errors).
Our objective is to find a faster method to solve it. Iterative method, instead, provide the solution of the system as a limit of a sequence $\{\mathbf{x}^k\}$, and usually involve the matrix A only through multiplications by a given vectors. We have to remind that for the simple test cases that we will solve at the beginning of chapter 3, *SuperLU* is a fast and not expensive solver, but going away from the ideal case, direct solver will fail. This is why we explore the solution with *Iterative Method*.

In our case A represent the algebraic formulation associated to the Galerkin problem. It can be proven that, when the grid-size decreases, the condition number of the matrix increases, and therefore the associated system becomes more and more ill-conditioned, see [27] for more detail. This calls for the system to be

preconditioned. It is therefore necessary to find an invertible matrix P, called preconditioner, such that $K_2\left(P^{-1}A\right) \ll K_2\left(A\right)$, where K_2 represent the condition number with respect to the norm 2, and then to apply the iterative method to the system preconditioned with P.
In order to derive a preconditioning strategy, we have to classify our situation. Problem like Stokes or Darcy in fluid dynamics are *saddle-point* type, they will be defined in the following section. This problem exhibit a peculiar nature, that we are going to use to provide an efficient solution strategy, as described in section 2 of this chapter using a general setting.
Nevertheless, when choosing a preconditioner, is essential to introduce the particular problem. We implemented a block-diagonal preconditioner, using the theory generously described in [3] and [13], based on Jacoby method, for the A-block part, and Schur discretization. Even if we can now provide more knowledge on the symmetric and defined positivity of the Schur complement S, the inverse is still computationally onerous to compute. Here we introduce the technique of the algebraic multigrid method for the resolution of a linear system. The explanation of what they are and how they will be used will be discuss in section 3 of this chapter.

Since we know that multigrid methods work really well for elliptic-type problem and we have available an Algebraic Multigrid Methods library, called SAMG, the discretization of the Schur complement is the natural direction to take.

2.1 Saddle Point problem

2.1.1 Problem statement and classification

As we can see from the following compact algebraic representation, our problem own the classical saddle-point structure, fully described in [3], namely:

$$\begin{bmatrix} \mathbf{A} & \mathbf{B}_1^T \\ \mathbf{B}_2 & -\mathbf{C} \end{bmatrix} \begin{bmatrix} x \\ y \end{bmatrix} = \begin{bmatrix} f \\ g \end{bmatrix}, \qquad \mathbf{A} \in \mathbb{R}^{n\times n},\, \mathbf{B}_{1,2} \in \mathbb{R}^{m\times n},\, \mathbf{C} \in \mathbb{R}^{m\times m} \quad \text{with } n \geq m, \tag{2.1}$$

we will later refer to our special case.

The constituent blocks of our saddle point type linear system, namely $\mathbf{A}, \mathbf{B}, \mathbf{C}$ satisfy the following conditions: $\mathbf{A}$ is symmetric and positive defined, $\mathbf{B}_1 = \mathbf{B}_2 = \mathbf{B}$, $\mathbf{C}$ is the zero matrix or it is symmetric, for uncoupled or coupled problem respectively in our case. The matrix $\mathbf{A}$ is the velocity mass matrix, a zero-order differential operator, $\mathbf{B}$ represents a discrete divergence operator and $\mathbf{B}^T$ a discrete gradient. In this cases we have two possible symmetric linear system of the form:

$$\begin{bmatrix} \mathbf{A} & \mathbf{B}^T \\ \mathbf{B} & 0 \end{bmatrix} \begin{bmatrix} x \\ y \end{bmatrix} = \begin{bmatrix} f \\ g \end{bmatrix}, \qquad \begin{bmatrix} \mathbf{A} & \mathbf{B}^T \\ \mathbf{B} & -\mathbf{C} \end{bmatrix} \begin{bmatrix} x \\ y \end{bmatrix} = \begin{bmatrix} f \\ g \end{bmatrix}, \tag{2.2}$$

.

Considering the first system, we can see his solution as a minimization problem of the form:

$$\min \quad J(x) = \frac{1}{2} x^T \mathbf{A} x - f^T x, \qquad \text{subject to} \quad \mathbf{B}x = g. \tag{2.3}$$

In this case y represent the Lagrange multipliers. Any solution (x^*, y^*) of problem 2.2 is a saddle point for the Lagrangian

$$\mathcal{L}(x, y) = \frac{1}{2} x^T \mathbf{A} x \; - \; f^T x \; + (\mathbf{B}x - g)^T \, y, \tag{2.4}$$

hence the name 'saddle point problem'. A saddle point is a point $(x^*, y^*) \in \mathbb{R}^{n+m}$ that satisfies

$$\min_x \max_y \mathcal{L}(x, y) = \mathcal{L}(x^*, y^*) = \min_y \max_x \mathcal{L}(x, y). \tag{2.5}$$

Stabilization is used when the finite element spaces of the variable x, y do not satisfy the *inf-sup* or Ladyzhenskaya-Babuska-Brezzi, LBB, condition. This will not be the case. It can be proven that reformulating the *inf-sup* condition at the algebraic level, we obtain the following generalized eigenvalue problem

$$\mathbf{B}\mathbf{A}^{-1}\mathbf{B}^T \; = \; \lambda \left(\frac{1}{\nu} M_p \right) \mathbf{P}, \tag{2.6}$$

where ν is the cinematic viscosity and M_p is the pressure mass matrix. As shown in [20], if the inf-sup constant β_h is independent from h, then the matrix $\mathbf{B}\mathbf{A}^{-1}\mathbf{B}^T$ is spectrally equivalent to $\frac{1}{\nu} M_p$. If the inf-sup condition is not satisfied, in algebraic

terms, means that:

$$\exists \mathbf{P}^* \in \mathbb{R}^{\mathcal{N}_p}, \quad U^T \mathbf{B}^T \mathbf{P} = 0, \quad \forall\, U \in \mathbb{R}^{\mathcal{N}_u},$$

$\mathbf{P}^*$ is called *spurious pressure modes* and $\mathbf{P}^* \in ker(\mathbf{B}^T)$.
Therefore, if the inf-sup condition is satisfied the kernel of $\mathbf{B}^T$ is empty, this implies that the dimension of the image of $\mathbf{B}$ is $\mathbf{N}_p$ and so:

$$\dim\left(\ker\left(\mathbf{B}\right)\right) = \mathcal{N}_u - \mathcal{N}_p, \tag{2.7}$$

moreover, when the discrete inf-sub condition is satisfied, the discrete space of velocities is larger than the space of pressures.
Let now intro introduce some general characteristics of saddle point problems.

Block factorizations and Schur complement The saddle point matrix admits the following block triangular factorization, with the condition of $\mathbf{A}$ to be nonsingular:

$$\begin{bmatrix} \mathbf{A} & \mathbf{B}^T \\ \mathbf{B} & -\mathbf{C} \end{bmatrix} = \begin{bmatrix} \mathbf{I} & \mathbf{O} \\ \mathbf{B}\mathbf{A}^{-1} & I \end{bmatrix} \begin{bmatrix} \mathbf{A} & O \\ O & \mathbf{S} \end{bmatrix} \begin{bmatrix} I & \mathbf{A}^{-1}\mathbf{B}^T \ \mathbf{O} & \mathbf{I} \end{bmatrix}, \tag{2.8}$$

where $\mathbf{S} = -\left(\mathbf{C} + \mathbf{B}\mathbf{A}^{-1}\mathbf{B}^T\right)$ is the Schur complement of $\mathbf{A}$. This matrix is fundamental for derive some theoretical aspect of this kind of problem, for example regarding the solvability conditions. It can be proven that the saddle point matrix is nonsingular if and only if $\mathbf{S}$ is. In order to discuss about the invertibility condition of Schur we have to restrict in our spacial case, that is $\mathbf{A}$ symmetric and $\mathbf{C} = \mathbf{O}$ or symmetric. In this case the Schur complement $\mathbf{S} = -\left(\mathbf{C} + \mathbf{B}\mathbf{A}^{-1}\mathbf{B}^T\right)$ is a symmetric negative defines matrix. The solvability condition of this problem can be summarize in this statement:

Theorem 2.1.1. *Assume* $\mathbf{A}$ *to be symmetric positive definite,* $\mathbf{B}1 = \mathbf{B}2 = \mathbf{B}$*, and* $\mathbf{C}$ *symmetric positive semidefinite. If* $ker\left(\mathbf{C}\right) \cap ker\left(\mathbf{B}^T\right) = 0$*, then the saddle point matrix is nonsingular. In particular, it is invertible if* $\mathbf{B}$ *has full rank.*

For instance, in Darcy, as in Stokes case, $\mathbf{B}^T$ represent a discrete gradient, therefore is often present a subspace of constant solution, called hydrostatic pressure mode, and the pressure is defined up to a constant. In order to remove this fact, one

option is to fix the value of the pressure in one point. However, iterative methods like GMRES are not effected by the presence of this zero-eigenvalue, if the initial solution for the velocity is zero.

Spectral properties of saddle point matrices If $\mathbf{A}$ is nonsingular, $\mathbf{B}$ has full rank and $\mathbf{C}$ is symmetric positive semidefinite or zero matrix, the saddle point matrix is congruent, or spectral equivalent, to the block diagonal matrix $\begin{bmatrix} \mathbf{A} & O \\ O & \mathbf{S} \end{bmatrix}$. This fact can be proved from factorization 2.8, obtaining:

$$\begin{bmatrix} \mathbf{I} & \mathbf{O} \\ -\mathbf{B}\mathbf{A}^{-1} & \mathbf{I} \end{bmatrix} \begin{bmatrix} \mathbf{A} & \mathbf{B}^T \\ \mathbf{B} & -\mathbf{C} \end{bmatrix} \begin{bmatrix} \mathbf{I} & -\mathbf{A}^{-1}\mathbf{B}^T \\ \mathbf{O} & \mathbf{I} \end{bmatrix} = \begin{bmatrix} \mathbf{A} & \mathbf{O} \\ \mathbf{O} & \mathbf{S} \end{bmatrix}. \tag{2.9}$$

Rusten and Winther present an important result for the bounds of the spectrum of saddle point matrix, in the case of $\mathbf{C} = \mathbf{0}$; we refer to Silvester and Wathen for a general case with $\mathbf{C}$ non zero.

2.1.2 Solution strategies and Preconditioning

Let now introduce some concepts regarding the possible solution strategies. They can be divided in two categories: *segregated* and *coupled* or *mixed* . Even for the iterative preconditioned approach we are going to follow the same that was used for direct method until now, a coupled one. Mixed finite element methods are favored when the velocity is the first variable of interest.

It is known that computing first the pressure and then the velocity bring to loss of accuracy.
Another vantage of mixed formulation is that they provide a locally mass conservation. For a better understanding of this fact we refer to [4].

In our case, a krylov subspace method is applied, GMRES exactly, with a particular problem-dependent preconditioner, based on segregated method. As we will se, the use of a good preconditioner is more important that the iterative method choose to solve the system. Our choice was to use GMRES as Krylov method, in order to be used even in case of general and non symmetric matrices, as our system matrix.
We remind that, since the spaces chosen for the problem discretization are inf-sup compatible, there is no need to add any stabilization therm. Ones the problem

is well defined, we deduce a faster and stable strategy for the resolution of the algebraic systems. As we already introduce, direct solver are the preferred method for ideal problem, but moving on more complex structure they will fail. Here we introduce iterative methods.
Furthermore, direct solver are still used to solve subproblems, like the one produced during the preconditioning procedure.

The negative point of the iterative methods, like Krylov subspace methods, is that, in some cases, the rate of convergence can be particularly low. Hence, the choice of the preconditioner is always a tricky process. An optimal preconditioner has to respect the following two criteria: first, its action on a general vector, namely $\mathbf{P}^{-1}\mathbf{w}$ can be computed with low computational cost, and second the fact that $\mathbf{P}$ as to be a good approximation of his matrix $\mathbf{A}$, in the sense $\mathbf{P}^{-1}\mathbf{A} \approx \mathbf{I}$.

Preconditioning attempts to improve the spectral properties of the system matrix, since the convergence depends on the distribution of the eigenvalues, so that convergence to a fixed tolerance is independent of the discretization parameter. The ideal preconditioner $\mathbf{P}$ is a matrix such that the preconditioned one, namely $\mathcal{M} = \mathbf{P}^{-1}\mathcal{A}$, where $\mathcal{A}$ is the system matrix, will have eigenvalues clustered around 1.

Since standard preconditioner are often found to perform poorly when applied to saddle point problem, there is the necessity to develop problem-dependent preconditioner. They require knowledge of the nature of the problem, the geometry and the discretization. We will focus our study on block preconditioners. One class of this preconditioners has close connection with Schur complement reduction.

Block diagonal preconditioners

The performance of such preconditioners depends on whether fast, approximate solver for linear system involving $\mathbf{A}$ and the Schur complement are available. In our case we are going to test both direct, in particular incomplete LU-factorization, and iterative methods in the form of algebraic multigrid methods.
In order to construct our preconditioner we will exploit the factorization 2.9.The basic block diagonal preconditioner is

$$\mathbf{P}_d = \begin{bmatrix} \mathbf{A} & \mathbf{O} \\ \mathbf{O} & -\mathbf{S} \end{bmatrix}, \tag{2.10}$$

where $\mathbf{S}$ is the already introduced Schur complement. Left preconditioning $\mathcal{A}$ with $\mathbf{P}_d$ we obtain:

$$\mathcal{M} = \mathbf{P}_d^{-1}\mathcal{A} = \begin{bmatrix} \mathbb{I} & \mathbf{A}^{-1}\mathbf{B}^T \\ -\mathbf{S}^{-1}\mathbf{B}^T & \mathbf{O} \end{bmatrix}. \tag{2.11}$$

Golub-Wathen (2000) provided the non-singularity of $\mathcal{M}$ showing the existence of three distinct eigenvalue, namely $1, \frac{1}{2}\left(1+\sqrt{5}\right)$ and $\frac{1}{2}\left(1-\sqrt{5}\right)$.!ADD LEMMA 5.2.7 GROSS

Using preconditioning in the iteration k of an iterative method like GMRES, practically means to solve the system $\mathbf{r}^{k+1} = \mathbf{P}^{-1}\mathbf{r}^k = \mathbf{P}^{-1}\left(\mathbf{b} - \mathcal{A}\mathbf{x}^0\right)$.

As known from literature, forming the preconditioned system $\mathcal{M}u = \mathbf{P}_d^{-1}b$ from the saddle point problem $\mathcal{A}u = b$, is as expensive as computing directly the inverse of the block matrix $\mathcal{A}$, since there exist an explicitly expression. This is why in practice we replace the ideal preconditioner $\mathbf{P}_d$ with its approximation $\widehat{\mathbf{P}}_d$:

$$\widehat{\mathbf{P}}_d = \begin{bmatrix} \widehat{\mathbf{A}} & \mathbf{O} \\ \mathbf{O} & -\widehat{\mathbf{S}} \end{bmatrix}, \tag{2.12}$$

where $\widehat{\mathbf{A}}$ and $\widehat{\mathbf{S}}$ are an approximation of the mass matrix $\mathbf{A}$ and the Schur complement $\mathbf{S}$.

Noticing that calling $\mathbf{w} = \mathbf{P}^{-1}\mathbf{y}$ is equivalent to solve the linear system $\mathbf{P}\mathbf{w} = \mathbf{y}$, practically it will never be compute $\widehat{\mathbf{A}}^{-1}$ or $\widehat{\mathbf{S}}^{-1}$, but we will solve two separated system, thank to the block-diagonal characteristic of $\mathbf{P}$, namely:

$$\widehat{\mathbf{A}}\,{\mathbf{r}_\mathbf{A}}^{k+1} = {\mathbf{r}_\mathbf{A}}^{k} \qquad \widehat{\mathbf{S}}\,{\mathbf{r}_\mathbf{S}}^{k+1} = {\mathbf{r}_\mathbf{S}}^{k}. \tag{2.13}$$

The solution strategies of this systems will be discussed later on and they will depend from the approximation strategies for the two different blocks.

2.2 Multigrid methods

In this section we give an introduction to multigrid method, both geometrical and algebraic, and to SAMG library, illustrating their functionality and efficiency.

The problem of iterative method is that they suffer of stagnation after a few iteration.

They have been used at the beginning for problem defined on geometrical domain. The basic idea under this method is to use a classical iterative method to smooth the error and project the discrete result on a lower dimensional space (coarser grid), where it will be easier to solve. At this point the result is reprojected back on the first higher dimensional space ("fine" grid). This projection strategy is iterated until the dimension of the problem is sufficient small to compute the solution in a very fast direct oi iterative way. The multigrid method are a combination of *smoothing* and *coarse grid correction*. In the 80s Ruge and Sruben have generalized this procedure for complex problem, decoupling multigrid from the geometric idea, introducing the spectral properties of matrices.

As we will see there exist two type of error, one in the space of high frequencies and the other in the space of low frequencies. The smoothing process goes to reduce the error on the high frequencies making it smooth, while the coarse grid correction work on the space of the low frequencies, transforming the smooth part of the error in rough.

Let now consider a generic linear system of the form:

$$A_h \, \mathbf{u}_h \, = \, \mathbf{f}_h. \tag{2.14}$$

The eigenvectors of the corresponding A_h matrix can be divided in low frequency and high frequency modes. Eigenvectors associated with high wavenumbers represent the oscillatory, or high frequency modes, whereas eigenvectors associated with low wavenumbers represent the smooth, or low frequency ones.

The error can be represented as a linear combination of the eigenvectors of the iteration matrix associated with the selected iterative method. The smoothing property of iterative method regards the fact that the error tends to decrease in the space generated from high frequency mode, remaining relegated in the space generated from low frequency mode, taking the characteristic smooth shape.

Both geometric and algebraic multigrid are based on the representation of smooth error modes as oscillatory ones, so that the iterative method computed on the coarse level can be more effective. In order to describe algebraic multigrid we need to present the basic concept on geometric multigrid. The algebraic one will be an extension of geometric on subspace created from spectral properties of our system.

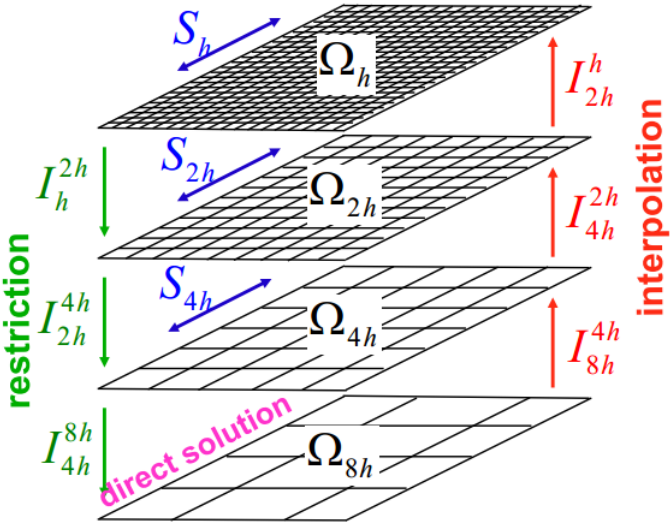

Figure 2.1: Two level Geometric multigrid

2.2.1 Geometric Multigrid

Geometric multigrid use a simple interpolation definition but efficient in case of problem defined on regular and simple geometric domain, where the sequence of discretization grid are easily defined. Let considering the problem 2.14, and let $\bar{\mathbf{u}}$ and $\tilde{\mathbf{u}}_h$ be the exact solution and the approximated one after ν iteration of an iterative method, namely $\tilde{\mathbf{u}}_h = S_h^{\nu}(\mathbf{u}_0, \mathbf{f}_h)$, where $\mathbf{u}_0$ represent the initial guess. As already introduced, the error $\mathbf{e}_h = \tilde{\mathbf{u}}_h - \bar{\mathbf{u}}$ is smooth and it can be seen has solution of the following system:

$$A_h \mathbf{e}_h = \mathbf{r}_h, \tag{2.15}$$

where $\mathbf{r}_h$ is the residual, $\mathbf{r}_h = A_h \tilde{\mathbf{u}}_h - \mathbf{f}_h$. We can now introduce two fundamental concept: Coarse Grid Correction and Multi Grid Method, following the approach proposed by Stüben [33].

Coarse Grid Correction

We saw that iterative method are able to reduce the high frequency component of the error, but after few iterations the convergence deteriorates. Let now see how to reduce the smooth component of it, there is where coarse grid correction (CGC) is used.

The advantage of study the system 2.15 instead of system 2.14 is that we can use the smoothness of the error and project it on a coarser grid. This space has lower dimension, therefore solve the problem on this space will be easier and choosing a greater discretization step improve the speed of convergence. Converting the error on a coarser grid transform the smooth component in oscillatory, then a fast convergence rate is restore. Ones the solution has been computed, it will be reprojected on the finest grid and, using the equation 2.2.1, we can compute the new approximated solution as follows:

$$\bar{\mathbf{u}} = \tilde{\mathbf{u}}_h - \mathbf{e}_h. \tag{2.16}$$

The smooth property of the error allows us to choose simple intergrid operator, with low computational cost. In order to solve the associated system on a coarser grid we need to project on that space not only the residual, but even the system matrix A_h. Let us now introduce some notations:

- Ω_h is the fine grid associated with the discretized problem with solution $\bar{\mathbf{u}}_h$
- Ω_H is the coarser grid respect to Ω_h and $\bar{\mathbf{u}}_H$ is the solution on this grid
- V_h and V_H are two finite dimensional spaces associated respectively to Ω_h and Ω_H, such that $\dim(V_H) < \dim(V_h) < +\infty$

There will be used the subscript h or H to distinguish quantities defined on the fine or coarse grid respectively. We now introduce two intergrid operators, prolongation and restriction, based on the geometric information of the problem.

Definition 1. *Let $v_h \in V_h$ and $v_H \in V_H$ be two discrete functions. The restriction operator $I_h^H : V_h \to V_H$ is such that*

$$I_h^H v_h = v_H. \tag{2.17}$$

Definition 2. *Let $v_h \in V_h$ and $v_H \in V_H$ be two discrete functions. The interpolation or prolongation operator $I_H^h : V_H \to V_h$ is such that*

$$I_H^h v_H = v_h. \tag{2.18}$$

Therefore we can define the residual restriction on Ω_H and the error prolongation on Ω_h as

$$\mathbf{r}_H = I_h^H \mathbf{r}_h, \qquad \text{and} \qquad \mathbf{e}_h = I_H^h \mathbf{e}_H. \tag{2.19}$$

The other component that has to be interpolated and prolongated is the coefficients matrix A_h. This choice can be provided following the Galerkin condition:

$$A_H = I_h^H A_h I_H^h, \tag{2.20}$$

A_H with this definition can be interpreted has the application of A_h on a vector of the space Ω_h and then prolongated using I_h^H on Ω_H. It can be verified [see [13]] that the Galerkin condition is verified if and only if

$$I_h^H = I_H^{hT}. \tag{2.21}$$

Thus the Galerkin condition implies the choice $I_h^H = I_H^{hT}$ for the restriction operator. In a compact formulation the coarse grid correction is as follows:

Algorithm 1: *Coarse Grid correction*

1 **Fine grid residual computation** : $\mathbf{r}_h = A_h \tilde{\mathbf{u}}_h - \mathbf{f}_h$
2 **Residual and A_h restriction on the coarse grid** : $\mathbf{r}_H = I_h^H \mathbf{r}_h$, $A_H = I_h^H A_h I_H^h$
3 **Error computation on Ω_H** : $\mathbf{e}_H = A_H^{-1} \mathbf{r}_H$
4 **Error prolongation** : $\mathbf{e}_h = I_H^h \mathbf{e}_H$
5 **Correction of the fine grid approximation** : $\hat{\mathbf{u}}_h = \tilde{\mathbf{u}}_h - \mathbf{e}_h$

Multi Grid Method

Combining together the smoothing process of the iterative method and the coarse grid correction we can define a *Two Grid Method*. The strategy is to place a few steps of smoothing process (pre-smoothing), of a chosen iterative method, before the coarse grid correction, and other steps of smoothing after the CGC (post-smoothing). All this steps perform to reduce the error in the frequency space where the previous iterations do not act well. Given an initial guess $\mathbf{u}_h^0$, we now present the procedure for a Two-Grid method:

This results can be apply recursively, obtaining a Multigrid Method. The process compute on Ω_h can be computed even on Ω_H and farther more, working on

Algorithm 2: *Two-Grid Method*

Pre-smoothing : ν_1 times solving $A_h\,\mathbf{u}_h = \mathbf{f}_h$ with an iterative method, $\tilde{\mathbf{u}}_h = S_h^{\nu}\left(\mathbf{u}_h^0, \mathbf{f}_h\right)$

Coarse Grid Correction : $\hat{\mathbf{u}}_h = CGC\left(\tilde{\mathbf{u}}_h, \mathbf{f}_h\right)$

Post-smoothing : ν_2 times solving $A_h\,\mathbf{u}_h = \mathbf{f}_h$ with an iterative method, $\tilde{\mathbf{u}}_h = S_h^{\nu}\left(\hat{\mathbf{u}}_h, \mathbf{f}_h\right)$

coarser and coarser grid. This results is well designed in figure 2.1, where multiple level of coarsening are drawn. After the ν_1 steps of pre-smoothing we compute the residual on Ω_H and we restrict it on a coarse grid Ω_{2H}. We continue in this way until we reach a system that is very fast to be computed, directly or recursively. Then the solution is interpolated back on the fine grids and eventually applied a post-smoothing. The process can be schematise as follows:

Algorithm 3: *Multigrid Method μ-cycle, MGM-μCycle*

if *k is the coarsest level* **then**
  Solve $A_k\,\tilde{\mathbf{u}_k} = \mathbf{f}_k$
else
  Pre-smoothing : ν_1 times solving $A_h\,\tilde{\mathbf{u}_h} = \mathbf{f}_h$ with an iterative method, $\tilde{\mathbf{u}}_k^{\nu_1} = S_k^{\nu_1}\left(\tilde{\mathbf{u}_k}, \mathbf{f}_k\right)$
  Residual computation : $\mathbf{r}_k = \mathbf{f}_k - A_k\,\tilde{\mathbf{u}}_k^{\nu_1}$
  Residual and A_h restriction on the coarse grid : $\mathbf{r}_{k+1} = I_k^{k+1}\mathbf{r}_k$, $A_{k+1} = I_k^{k+1}\,A_k\,I_{k+1}^k$
  $\mathbf{u}_{k+1}^0 = \mathbf{0}_{k+1}$
  for *l=1:μ* **do**
    $\tilde{\mathbf{u}}_{k+1}^l = MGM - \mu\text{Cycle}\left(\mathbf{u}_{k+1}^0, \mathbf{r}_{k+1}, A_{k+1}\right)$
  end
  Error prolongation : $\mathbf{e}_k = I_{k+1}^k\,\mathbf{e}_{k+1}$
  Correction of the fine grid approximation : $\tilde{\mathbf{u}}_k = \tilde{\mathbf{u}}_k - \mathbf{e}_k$
  Post-smoothing ν_2 times : $\tilde{\mathbf{u}}_k^{\nu_1} = S_k^{\nu_2}\left(\tilde{\mathbf{u}_k}, \mathbf{f}_k\right)$
end

The parameter μ characterize the type of multigrid cycle with the respect to the shape assumed from the graphic representation of restriction and interpolation. For $\mu = 1$ we have the V-cycle, instead for $\mu = 2$ we obtain the W-cycle. Both structure are presented in Figure 2.2. Those are the most used and simple scheme, but there exist more complex structure, created as combination of V and W cycle. We refer to [5] for more detail.

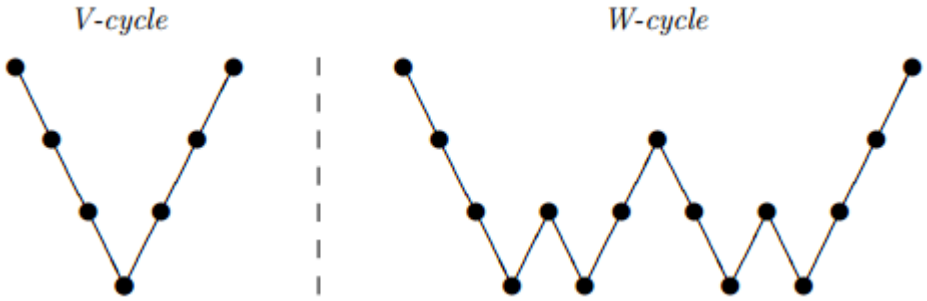

Figure 2.2: Graphic representation of multigrid V-cycle and W-cycle on four levels

2.2.2 Algebraic Multigrid

In this section we will introduce the concept of Algebraic multigrid method starting from the Geometric one, defined previously. The first developments of AMG method were presented from Brandt 1985,1986. We will refer to an iterative method as "smoother", due to the effect that its application provide on the error estimation. As we already saw for the Geometric Multigrid, a classical iterative method used as *smoother* is not reducing efficiently the error in all the space generated from the eigenvectors of a system matrix A, but only on a subspace. The Algebraic multigrid method works projecting the problem is this subspace, using the spectral information of the matrix A.

In geometric multigrid the unknown variable are defined at grid points and we select a subset of this points as coarser grid. In algebraic multigrid, a coarser grid will refer to a subset of index of out unknown variable.

The biggest difference between the geometric environment and the algebraic one, concern the smooth concept. In a geometric multigrid the term "smooth" is used in a natural way and to be seen relative to a coarser grid. In algebraic multigrid, instead, there are no pre-defined grids and a smoothing property in the geometric sense becomes meaningless. We will introduce in this section a new concept of *algebraically smoothness*.

Before to do that, we need to introduce the concept of *undirected adjacency graph*, because it gave us all the geometric information that we need. We construct an adjacency graph associating the vertices of the graph with the grid points and drawing an edge between the vertices i and j if either A_{ij} or A_{ij} are different from zero. Every grid is completely defined by his graph. It is not the objective of this thesis to discuss about adjacency graph, therefore we refer to [12] and [6] for more

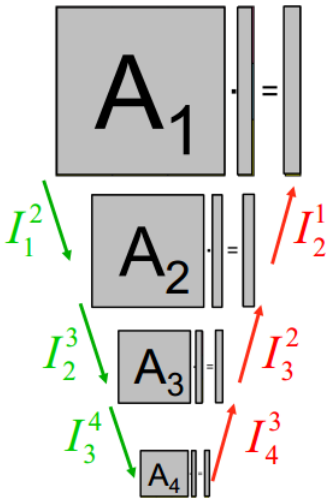

Figure 2.3: Two level Geometric multigrid

information. In this work we will just describe how to select a coarse grid using the graph theory. The steps will be: define the new smoothing properties, choose the intergrid transfer operators, using this new characteristics we will describe how to select the coarse grid, so that coarse-grid correction has the same effect that it has in geometric multigrid. Concretely speaking, it must eliminate the error components in the range of the interpolation operator.

Moving from geometric the spectral analysis, we must adopt some restriction on the coefficient matrix A, in order to construct suitable restriction and projection operator. The most classic and studied choice is the one defined from Ruge and Stuben in [35], which requires A to be symmetric and positive defined.

In conclusion, it is useful to highlight that one of the advantage of AMG method is that they can be easily parallelized, since we are working extrapolating completely the algebraic meaning from the geometric sense. !! aggiungere il riferimento all'immagine 2.3.

Algebraic Smoothness

Since algebraic multigrid approach is based on abstraction from the geometric sense, we cannot simply examine the Fourier modes of the error in order to study the smoothness property. We will proceed by analogy. In the geometric case, the most important property of smooth error is that it is not effectively reduced by an iterative method. Thus, we can define smooth an error that is not reduced

effectively by iterative scheme.

Before to define formally what an algebraically smooth error is, we highlight another important difference between Geometric and Algebraic Multigrid. In the Geometric approach the projection operator is fixed and the smoother is defined in order to satisfy any request of this operator. On the contrary, for the AMG, the smoother is fixed and studying the property of the smooth error we define an appropriated projection operator.

Hence, let now define a smoothing operator $R_h \in \mathbb{R}^{N_h \times N_h}$, associated to a selected iterative method. We can state:

Definition 3. *We define an error* $\mathbf{e}_h$ *to be* algebraic smooth *if it converges slowly with respect to a given smoothing operator* R_h*, namely if:*

$$R_h \, \mathbf{e}_h \approx \mathbf{e}_h.$$

Using this definition in the error system 2.15 we obtain $A_h \, \mathbf{e}_h \approx \mathbf{O}_h$, which means that the smooth error has small residual.

One important consequence of this, is that we can approximate $\mathbf{e}_i$ with an average of its neighbors:

$$a_{ii} e_i \approx -\sum_{j \neq i} a_{ij} e_j. \tag{2.22}$$

This fact is important in determining the interpolation operator.

Influence and Dependence

After the concept of smoothness, the second important one is the strong dependence or strong influence. As already introduced, algebraic multigrid perform very well on diagonal dominance matrix, where the assumption defined for create intergrid operator are verified. Because of the dominance of the diagonal entry entry A, we can associate the ith equation with the ith unknown.

We are going to determine with other unknown are important in determining the ith variable. Let observe that if the coefficient a_{ij}, which multiplies $\mathbf{u}_j$ in the ith equation, is large relative to the other coefficients in the ith equation, then a small change in the value of u_j has more effect on the value of u_i respect any small change in the other variable of the same equation. Hence, given a threshold value $\theta \in (0, 1]$ we can define a strength function $s : \mathbb{R} \times \mathbb{R} \to \mathbb{R}^+$ as follows:

Definition 4. *The variable u_i is strongly dependent on j if*

$$s\,(i,j) \geq \theta. \tag{2.23}$$

Therfore, if the variable i strongly depends on variable j, then j strongly influences i. There exist different definitions for the strength function, we refer to [5] and [33] for details.

Interpolation Operator and Coarse Grid Selection

In this section we are going to explain the general idea for Interpolation and Coarse Gridb Correction, following the strategy proposed in [5].

Assuming that it is already given a selection of coarse-grid points, we can gather together the index 1,2,...,n in two set, C and F, such that $C \cup F$, where C correspond to the coarse grid variables and F contains only the variable defined on the fine grid. Let e_i, $i \in C$, be the error component that have to be interpolated on the fine grid. In the geometric multigrid linear interpolation is sufficient, but in this contest it is not. In order to construct a formula to approximate the fine-grid value e_j, we notice that if a $j \in C$ strongly influences an F-point i, then the value e_j contributes heavily to the value of e_i. Whereas, if $j \in C$ not strongly influences $i \in F$, e_j will not contribute. Thus, we can justify the idea that the fine-grid variable u_i can be interpolated from the coarse-grid quantity u_j if i strongly depends on j. We can now define the interpolation operator as follows, always referring to a fine grid with h and to a coarse one with H:

$$I_H^h\, e_i \;=\; \begin{cases} e & \text{if } i \in C, \\ \sum_{j \in C} \omega_{ij} e_j & \text{if } i \in F, \end{cases} \tag{2.24}$$

where ω_{ij} are weights, still to be determined. For a better understand of the construction process and demonstration, we refer to [5]. Let now move our focus on the Coarse Grid Selection. As in the geometric multigrid we need to provide a coarse grid where: the smooth error can be approximated accurately and that has fewer points, so that the residual problem can be solved easier then on the fine grid.

The selection process progress as follows. We first make an initial partitioning of the grid points into C-points and F-points. Then, as the interpolation operator

is constructed, we make adjustments to this partitioning, changing points initially chosen as F-points to be C-points and vice versa. This process is computed in order to ensure certain rules, which can be state in:

- for each F-point i, every point j that strongly influences i either should be in the coarse interpolatory set C_i or should strongly depend on at least one point in C_i
- the set of coarse points C should be a maximal subset of all points with the property that no C-point strongly depends on another C-point,

Since it is not always possible to enforce both of the previous hypothesis, a trade-off between accuracy and expense is generally worthwhile.

Defined this two request, we can review the procedure. The first selection is computer trying to satisfy the second hypothesis, then a second pass is made changing the position of the indexes in order to enforce the first one.

This approach is usually computed using the coloring scheme. As for the Interpolator constriuction we will not propose here the demonstration, but it can be find in [5].

Restriction Operator

Now that we define how to construct the Interpolation Operator and the Coarse Grid Selection, we clarify the notations, that will be the same proposed for the geometric approach. Let first define the prolongation and restriction operator.

Definition 5. *Let* $\mathbf{v}_h \in \mathbb{R}^{N_h}$ *and* $\mathbf{v}_H \in \mathbb{R}^{N_H}$*. The restriction operator* $I_h^H : \mathbb{R}^{N_h} \to \mathbb{R}^{N_H}$ *is such that*

$$I_h^H \mathbf{v}_h = \mathbf{v}_H. \tag{2.25}$$

Definition 6. *Let* $\mathbf{v}_h \in \mathbb{R}^{N_h}$ *and* $\mathbf{v}_H \in \mathbb{R}^{N_H}$*. The interpolation or prolongation operator* $I_H^h : \mathbb{R}^{N_H} \to \mathbb{R}^{N_h}$ *is such that*

$$I_H^h \mathbf{v}_H = \mathbf{v}_h. \tag{2.26}$$

The same properites defined prevoiusly in the geometric contenst has to hold again, therefore we have that

$$I_h^H = I_H^{hT}. \tag{2.27}$$

and for we construct the coarse-grid operator based on the Galerkin condition:

$$A_H = I_h^H A_h I_H^h. \tag{2.28}$$

Two-Grid and Multigrid cycle

The algorithm proposed previously for the algebraic concept, can be completely extend for the algebraic one, maintaining the same structure, but referring to interpolation, restriction and coarse-grid correction from the algebraic point of view. The algorithm are not proposed anymore, since they are completely equal to the geometric one.

An example of an algebraic multigrid V-cycle at 4 levels can be seen in figure 2.3. As we can see going deeper in the levels bring at the construction of smaller and smaller matrix, until the 0-level (smallest) size is achieved, then the solution can be computed with a direct method and re-interpolated on the finest one until the beginning of the process.

2.2.3 Multigrid as preconditioner

Originally, the algebraic multigrid method has been developed as a stand-alone iterative solver. Practical experience, however, has clearly shown that AMG is also a very good preconditioner, much better than standard (one-level) preconditioners. Heuristically, the major reason is due to the fact that AMG, in contrast to any one-level preconditioner, aims at the efficient reduction of all error components, short-range as well as long-range. Consequently, highest efficiency is typically obtained if multigrid cycling is accelerated by standard methods such as conjugate gradient (CG), BiCGstab or GMRes.
We are going to present now the main steps for a GMRES iterative methods using Algebraical Multigrid as preconditioner, (Algorithm 4), following the GMRES method proposed by [27].

2.2.4 The SAMG Library

SAMG (Algebraic Multigrid Methods for Systems) is a library provided from the Institute for Algorithms and Scientific Computing (SCAI). It contains subroutines for the highly efficient solution of large linear systems of equations with sparse

Algorithm 4: *AMG-Preconditioned Gmres*

Initialization : $\mathbf{x}^{(0)}$; $P\mathbf{r}^{(0)} = \mathbf{f} - A\mathbf{x}^{(0)}$; $\mathbf{x}^{(1)} = \mathbf{r}^{(0)}/||\mathbf{r}^{(0)}||_2$;
Iteration : **for** *j=1:k* **do**
  Compute $AMG - \mu\text{Cycle}\left\{P\mathbf{w}^{(j)} = A\mathbf{x}^{(j)}\right\}$
  for *i=1,j* **do**
    $g_{ij} = (\mathbf{x}^{(i)})^T(\mathbf{x}^{(j)})$
    $(\mathbf{x}^{(j)}) = (\mathbf{x}^{(j)}) - g_{ij}\mathbf{x}^{(i)}$
  end
  $(\mathbf{x}^{(j+1)}) = (\mathbf{w}^{(j)})/||(\mathbf{w}^{(j)})||_2$
end
$V_k = [\mathbf{x}^{(0)}, ..., \mathbf{x}^{(k)}]$, $\hat{H}_k = g_{ij}$, $1 \leq j \leq k$,$1 \leq i \leq j+1$;
Compute , the minimizer for $||\mathbf{r}^{(0)}||_2\, \mathbf{e}^{(1)} - \hat{H}_k\mathbf{z}$
Set $\mathbf{x}^{(k)} = \mathbf{x}^{(0)} + V_k\mathbf{z}^{(k)}$.

matrices. Usually, the numerical solution of these linear systems of equations needs most of the computational time of the whole simulation.

Compared to classical methods, SAMG has the advantage of being almost unconditionally numerically scalable. This means that the computational cost using SAMG depends only linearly on the number of unknowns. Depending on the application and problem size, the computational cost can be reduced by one to two orders of magnitude. SAMG can be incorporated into an existing software package as easily as any classical method.

SAMG is written in FORTRAN90 and it is based on an AMG approach which has turned out to be very flexible, robust and efficient in practice, the only restriction is that can be applied to both scalar and coupled systems but of "elliptic" partial differential equations type.

This is why apply it directly to our system is not working due to the presence of not diagonal dominance for the pressure block, but it will be used to solve the residual system in a GMRES iteration where an elliptic type problem arise from the discretization of the Laplacian associate to the pressure Schur complement.

SAMG can be used as a "plug-in" solver. Just the sparse linear system of equations modified in a particular form has to be passed to SAMG. In general, no information regarding the shape of the domain or the structure of the underlying grid needs to be provided. Thus, besides its robustness and efficiency, the main practical advantage of SAMG is that it can directly be applied to solve certain

classes of PDEs on unstructured meshes, both in 2D and 3D. Moreover, SAMG can even be applied to problems without any geometric background, provided that the underlying matrices are of a "similar type" as the ones arising from elliptic PDEs.

Chapter 3

Preconditioning strategies for the discrete coupled 3D-1D problem

In this chapter we are going to explain the possible solution strategies for the system resolution. As showed in scheme 3.1, the strategies can be separated in direct or iterative. For the direct option SuperLu was used.
Whereas, the iterative method studied in this work is GMRES. Both GMRES preconditioned and non preconditioned are tested. As we will see, the velocity preconditioner will be easily invertible, while the situation for the Schur complement approximation will be non trivial. Therefore, once the preconditioned strategy is chosen, we need to specify an auxiliary method for the resolution of the associated residual system $\mathbf{r}^{k+1} = \widehat{\mathbf{P}}_d^{-1}\mathbf{r}^k$.
The possible choices are: an Incomplete LU factorization or an Algebraic Multigrid Method. Due to all the advantages of AMG previously described, the second is the most interesting direction.

As we will see, the preconditioner is constructed differently with respect to every situation analyzed. Different preconditioners for the stand alone vessel, tissue and uncoupled problem are derived. For the coupled problem, instead, a different strategy has to be described.

This chapter will analyze the problem in the following order:

1. Preconditioner definition

2. Iterative strategy

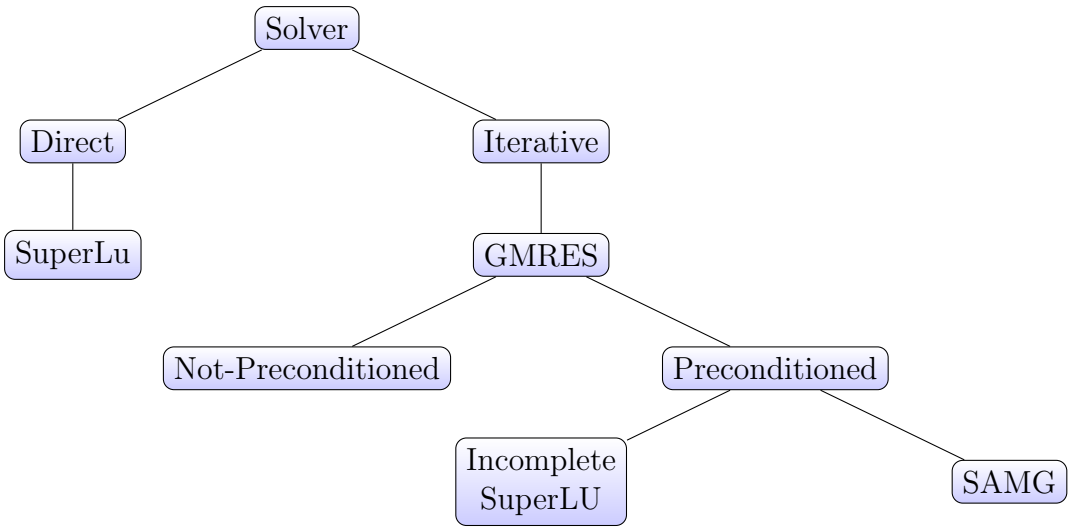

Figure 3.1

3. Definition of the residual system solver.

3.1 Specifications of Darcy and Stokes problem

Let us now clarify the solution strategy for our particular Darcy and Stokes problem. At the beginning we are going to treat separately the equation regarding the tissue and the vessel, in order to derive a general solution strategy for a single problem and, at a later stage, we will describe the global solution strategy. We can define four type of problem that we want to explore: Darcy in the tissue Σ_1, Stokes with Poiseuille hypothesis in the vessel Σ_2, uncoupled global system per tissue-vessel Σ_3, and the coupled one Σ_4. Let us define this problem with a new compact notation, where we invert the sign of the two pressure equations, refereed to the old one as follows:

$$\Sigma_1 := \begin{bmatrix} \mathbf{A}_t & \mathbf{B}_t^T \\ \mathbf{B}_t & \mathbf{O} \end{bmatrix} \begin{bmatrix} \mathbf{U}_t \\ \mathbf{P}_t \end{bmatrix} = \begin{bmatrix} \mathbf{F}_t \\ \mathbf{G}_t \end{bmatrix}, \tag{3.1}$$

$$\Sigma_2 := \begin{bmatrix} \mathbf{A}_v & \mathbf{B}_v^T \\ \mathbf{B}_v & \mathbf{O} \end{bmatrix} \begin{bmatrix} \mathbf{U}_v \\ \mathbf{P}_v \end{bmatrix} = \begin{bmatrix} \mathbf{F}_v \\ \mathbf{G}_v \end{bmatrix}, \tag{3.2}$$

$$\Sigma_3 := \begin{bmatrix} \mathbf{A}_t & \mathbf{B}_t & \mathbf{O} & \mathbf{O} \\ \mathbf{B}_t & \mathbf{O} & \mathbf{O} & \mathbf{O} \\ \mathbf{O} & \mathbf{O} & \mathbf{A}_v & \mathbf{B}_v^T \\ \mathbf{O} & \mathbf{O} & \mathbf{B}_v & \mathbf{O} \end{bmatrix} \begin{bmatrix} \mathbf{U}_t \\ \mathbf{P}_t \\ \mathbf{U}_v \\ \mathbf{P}_v \end{bmatrix} = \begin{bmatrix} \mathbf{F}_t \\ \mathbf{G}_t \\ \mathbf{F}_v \\ \mathbf{G}_v \end{bmatrix} \tag{3.3}$$

$$\Sigma_4 := \begin{bmatrix} \mathbf{A}_t & \mathbf{B}_t & \mathbf{O} & \mathbf{O} \\ \mathbf{B}_t & -\mathbf{C}_t & \mathbf{O} & \mathbf{Q}_{tv} \\ \mathbf{O} & \mathbf{O} & \mathbf{A}_v & \mathbf{B}_v^T \\ \mathbf{O} & \mathbf{Q}_{vt} & \mathbf{B}_v & -\mathbf{C}_v \end{bmatrix} \begin{bmatrix} \mathbf{U}_t \\ \mathbf{P}_t \\ \mathbf{U}_v \\ \mathbf{P}_v \end{bmatrix} = \begin{bmatrix} \mathbf{F}_t \\ \mathbf{G}_t \\ \mathbf{F}_v \\ \mathbf{G}_v \end{bmatrix} \tag{3.4}$$

where

$$\mathbf{A}_t = \mathbb{M}_{tt}, \qquad \mathbf{B}_t = -\mathbb{D}_{tt}, \qquad \mathbf{G}_t = \mathbb{B}_{tt}\sigma\Delta\pi$$

$$\mathbf{A}_v = \mathbb{M}_{vv}, \qquad \mathbf{B}_v = -\mathbb{D}_{vv} - \mathbb{J}_{vv}, \qquad \mathbf{G}_v = \mathbb{B}_{vv}\sigma\Delta\pi$$

$$\mathbf{C}_t = \mathbb{B}_{tt}, \quad \mathbf{C}_v = \mathbb{B}_{vv}, \quad \mathbf{Q}_{tv} = \mathbb{B}_{tv}, \quad \mathbf{Q}_{vt} = \mathbb{B}_{vt}.$$

We observe that problem Σ_1 and Σ_2 are of the same nature, $\mathbf{A}_t$ represent a mass matrix, $\mathbf{B}_t^T$ a discrete gradient and $\mathbf{B}_t$ a discrete divergence operator. Due to this fact, the solution strategies for both problems are equivalent. The only difference, as we will se, regards the discretization of the Schur complement, that change according to the discrete finite element method used for the unknown pressure.

3.2 A preconditioner for the Schur complement of saddle point problems

In order to describe the optimal choice for the preconditioner in our problem we have to remind the finite element spaces used for tissue and vessel separately Regarding the tissue the choice was Raviart-Thomas with piecewise constant $\mathcal{P}^0$ function, RT_0^h, and Discontinuous Galerkin locally piecewise constant $\mathcal{P}^0$, $DGP0$, for velocity and pressure respectively. For this *H-div conforming* approximation, the degrees of freedom for the velocity are normal components in the center of the edges, while the pressure is sampled at element centroids, as showed in Figure 3.2. The vessel choice was $P2/P1$, instead. Both are *H-div conforming* approximation. Using as starting point the result provide from [23], we are going to

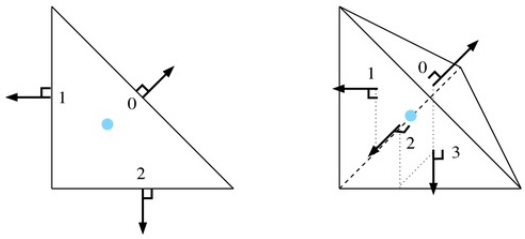

Figure 3.2: Degrees of freedom for pressure and velocity.

describe in detail the approximation strategies for $\widehat{\mathbf{P}}_d$. They propose two different approaches, one conforming and the other one non conforming. We will introduce a conforming approach taking advantage of the second non-conforming approach from the algebraic point of view.

Tissue approximation

We will now refer in our notation to the system Σ_1. Let point out the meaning of the matrix involved in this problem: $\mathbf{A}_t$ represent the velocity mass matrix multiplied for the inverse of dimensionless permeability tensor $\mathbf{K}_t$, $\mathbf{B}_t^T$ a discrete gradient and $\mathbf{B}_t$ a discrete divergence. Considering the preconditioner 2.12 let take $\widehat{\mathbf{A}}_t$ as the diagonal part of $\mathbf{A}_t$:

$$\left[\widehat{\mathbf{A}_t}\right] = (\mathbf{A}_t)_{ij}\,. \tag{3.5}$$

Since the coefficient $\mathbf{K}_t$ is a continuous scalar, the constrain of smoothness is perfectly respected. Therefore the approximated $\widehat{\mathbf{A}_t}$ is spectrally equivalent to $\mathbf{A}_t$. The computation of the inverse of $\widehat{\mathbf{A}_t}$ is now trivial, since it has a diagonal form. We are now focusing on the Schur complement, which is a very delicate matter. For mixed approach $\mathbf{S}_t = -\mathbf{B}_t\mathbf{A}_t^{-1}\mathbf{B}_t^T$ can be interpreted as a negative second order diffusion operator on the pressure unknown. This is explained from the differential meaning of the matrices involved: $\nabla(k_t^{-1}\cdot\nabla) \cong \Delta$. Therefore, we aim to determine the approximation of the Schur complement selecting an appropriate approximation for the Laplace operator on the space where the pressure belongs. A. Quarteroni and A. Valli proposed in [28] a stabilization method in case of lowest order elements, with spaces not inf-sup stable. Following the same approach let

approximate the Laplacian for 0-order pressure with this form:

$$\Delta_{ht}\left(p_t, q_t\right) \;=\; \delta \sum_{\sigma \in I_0} \int_{\sigma} \left[p_t\right] \left[q_t\right] \qquad \forall\, q_t \in Q_t \tag{3.6}$$

where I_0 is the set of all interior edge, where the one belonging to the boundary are ignored, and and δ is a penalization constant, that in this case will be the reciprocal of the element size.
Let now introduce the boundary condition. Considering the fact that we impose in our problem the boundary condition in a weakly form, in case of homogeneous Dirichlet BC we add the penalty therm

$$\mu_t \sum_{\sigma \in \partial O_{k_t}} \int_{\sigma} p_t \, q_t, \tag{3.7}$$

p_t and q_t are respectively the pressure discretized and his test function, while μ is a penalization term, that is consider the same of the previous one, and ∂O_{k_t} are the edge of the boundary elements.
For homogeneous mixed boundary condition we obtain:

$$\mathbf{u}_t \cdot \mathbf{n} \;=\; -k_t \nabla p_t \cdot \mathbf{n} \;=\; 0 \tag{3.8}$$

imposing them in a weak form and considering the fact that the gradient of pressure is null, since the pressure is locally constant, it remains:

$$\sum_{\sigma \in \partial O_{k_t}} \int_{\sigma} k_t \, p_t \, q_t, \tag{3.9}$$

Finally, the possible two representation for the Schur discretization are:

$$\begin{aligned} \widehat{\mathbf{S}}_{ht}\left(p_t, q_t\right) \;&=\; \delta \sum_{\sigma \in I_0} \int_{\sigma} \left[p_h\right] \left[q_h\right] \;+\; \mu \sum_{\sigma \in \partial O_{k_t}} \int_{\sigma} p_h \, q_h, \quad \forall\, q_t \in Q_t, \\ \widehat{\mathbf{S}}_{ht}\left(p_t, q_t\right) \;&=\; \delta \sum_{\sigma \in I_0} \int_{\sigma} \left[p_h\right] \left[q_h\right] \;+\; \sum_{\sigma \in \partial O_{k_t}} \int_{\sigma} k_t \, p_h \, q_h, \quad \forall\, q_t \in Q_t. \end{aligned} \tag{3.10}$$

Let us now derive the algebraic form of out discrete Schur complement. Therefore

the algebraic form of the Schur complement discretization is:

$$\left[\widehat{\mathbf{S}}_{ht}\right]_{ij} = \delta \sum_{\sigma \in I_0} \int_\sigma [\psi_i]\,[\psi_j] + \mu \sum_{\sigma \in \partial O_{k_t}} \int_\sigma \psi_i\,\psi_j,$$
$$\left[\widehat{\mathbf{S}}_{ht}\right]_{ij} = \delta \sum_{\sigma \in I_0} \int_\sigma [\psi_i]\,[\psi_j] + \sum_{\sigma \in \partial O_{k_t}} \int_\sigma k_t\,\psi_i\,\psi_j. \tag{3.11}$$

and the global preconditioner is:

$$\widehat{\mathbf{P}}_{ht} := \begin{bmatrix} diag(\mathbf{A}_t) & \mathbf{O} \\ \mathbf{O} & \widehat{\mathbf{S}}_{ht} \end{bmatrix}. \tag{3.12}$$

Vessel approximation

Following the same strategy described for Σ_1, we will derive the preconditioner approximation for Σ_2. For $\mathbf{A}_v$ we will use the same approximation, $diag(\mathbf{A})$:

$$\left[\widehat{\mathbf{A}_v}\right] = (\mathbf{A}_v)_{ij}\,. \tag{3.13}$$

For the Schur complement, the situation is different because of the finite element spaces. Here we use local approximation with $P1$ so it is a classical weak formulation for the Laplacian operator. In this case there is no need to introduce special hypothesis , but we can easily integrate by parts, namely:

$$\Delta_{hv}\,(p_v, q_v) = \int_{\Lambda_t} \nabla p_v\,\nabla q_v\,d\,s \qquad \forall\, q_v \in Q_v. \tag{3.14}$$

Moving now on the weak imposition of the boundary condition we highlight that in the vessel we will always work with non homogeneous Dirichlet condition, therefore the boundary condition therm will be:

$$\mu_v \sum_{\sigma \in \partial O_{k_v}} \int_\sigma p_v\,q_v. \tag{3.15}$$

In this situation the penalization therm μ_v has to be a positive constant ≥ 1.

Summarizing, the global bilinear form for discrete Schur approximation is:

$$\widehat{\mathbf{S}}_{hv}\,(p_v, q_v) \;=\; \int_{\Lambda_t} \nabla p_v\,\nabla q_v\,d\,s \;+\; \mu_v \sum_{\sigma\in\partial O_{k_v}} \int_{\sigma} p_v\,q_v, \qquad \forall\, q_v \in Q_v \tag{3.16}$$

and its algebraic for is:

$$\left[\widehat{\mathbf{S}}_{hv}\right]_{ij} \;=\; \int_{\Lambda_t} \nabla\psi_i\,\nabla\psi_j\,d\,s \;+\; \mu_v \sum_{\sigma\in\partial O_{k_v}} \int_{\sigma} \psi_i\,\psi_j, \tag{3.17}$$

For the vessel problem we conclude that the approximated diagonal preconditioner is:

$$\widehat{\mathbf{P}}_{hv} \;:=\; \begin{bmatrix} diag(\mathbf{A}_v) & \mathbf{O} \\ \mathbf{O} & \widehat{\mathbf{S}}_{hv} \end{bmatrix}. \tag{3.18}$$

Uncoupled tissue-vessel approximation

Now, focusing on Σ_3, we notice that the tissue and the vessel problem are completely independent. Due to that we can assembly a four-block diagonal preconditioner of the form:

$$\widehat{\mathbf{P}}_{d} \;:=\; \begin{bmatrix} diag(\mathbf{A}_t) & \mathbf{O} & \mathbf{O} & \mathbf{O} \\ \mathbf{O} & \widehat{\mathbf{S}}_{ht} & \mathbf{O} & \mathbf{O} \\ \mathbf{O} & \mathbf{O} & diag(\mathbf{A}_v) & \mathbf{O} \\ \mathbf{O} & \mathbf{O} & \mathbf{O} & \widehat{\mathbf{S}}_{hv} \end{bmatrix}. \tag{3.19}$$

This block-diagonal preconditioner is used inside the GMRES iteration in order to resolve the uncoupled problem. For the coupled problem instead, the situation is different.

We are not going to define a monolithic preconditioner for the coupled problem, but we will use a different strategy, which will be describe later. Let now close this first part, describing how this new preconditioners are used in combinations with Algebraic Multigrid Method.

3.3 Preconditioned GMRES for uncoupled problem

As already discussed, we aim to solve our problem using a preconditioned GMRES, and the final objective is to use AMG as preconditioner for the residual part of the Schur complement to accelerate the convergence of this iterative scheme.
In the previous section we introduced the monolithic preconditioner for uncoupled problem. We are going now to describe in detail how this preconditioner is used inside the GMRES algorithm, described in section 2.2.3, and how it interacts with Algebraic Multigrid Methods.

Practically speaking, the system that we aim to solve inside an iteration of GMRES method is $\mathbf{r}^{k+1} = \widehat{\mathbf{P}}_d^{-1}\mathbf{r}^k$, but in this case the residuals, with respect to every unknown, are uncorrelated. Therefore we want to solve four separated systems:

$$\mathbf{r}_{tv}^{k+1} = diag(\mathbf{A}_t)^{-1}\mathbf{r}_{tv}^k, \qquad \mathbf{r}_{tp}^{k+1} = \widehat{\mathbf{S}}_{ht}^{-1}\mathbf{r}_{tp}^k$$

$$\mathbf{r}_{vv}^{k+1} = diag(\mathbf{A}_t)^{-1}\mathbf{r}_{vv}^k, \qquad \mathbf{r}_{vp}^{k+1} = \widehat{\mathbf{S}}_{ht}^{-1}\mathbf{r}_{vp}^k.$$

Computing the inverse of a diagonal matrix is immediate, but for the both Schur complement approximated, we can avoid the computation of the inverse, describing the action of the inverse matrix on a vector, by means of the solution of the corresponding linear system.
A vector $\mathbf{x} = \mathbf{Q}^{-1}\mathbf{y}$ can be implemented by performing one iteration of the iterative method applied to $\mathbf{Qx} = \mathbf{y}$. Noticing that the higher the convergence rate of the iterative method to compute this two systems, the better the quality of $\widehat{\mathbf{P}}_d$. Two different approaches can be used:

- an *Incomplete LU factorization*
- an *Algebraic Multigrid Method.*

The Incomplete LU factorization seeks triangular matrices L, U such that $\hat{S} \approx LU$ rather than $\hat{S} = LU$. The solution of $LUx = b$ is computed rapidly, but it does not yield the exact solution.

Table 3.1: Possible solution strategies for the Schur complement residual problem. Strategies with * indicate that we use a classical diagonal inversion for the residual system corresponding to the velocity unknown.

$Test$	$SuperLU$	ILU^*_{tv}	$SAMG^*_{tv}$	$Non-Prec^*_{tv}$
A_1	$\times$			
B_1		$\times$		
C_1			$\times$	
D_1				$\times$

The other strategy of Multigrid, calls the SAMG library, which is also a very good preconditioner, much better than standard (one-level) preconditioners. In this case is used as preconditioner, for a GMRES method external of the SAMG library. Therefore, in this case, SAMG act as an Algebraic Multigrid system solver. We need to highlight that the problem derived for the Schur complement has an elliptic nature, hence this is the standard background for Algebraic Multigrid Method.

In conclusion, Table 3.1 contains all the possible strategies for solve the residuals systems. We remind that we classify the possible strategies considering the Schur complement approximation, while the residual system for the velocity unknown is always equal and trivial.

In the following chapter we are going to recall this test cases using the same notation. Test A_1 is refereed to solve the global uncoupled problem with a direct SuperLU method. Test B_1 and C_1 are designed to test the effect of the different preconditioned (ILU and SAMG respectively) approach on both tissue and vessel Schur complement approximation, while as we already explain, the velocity residual is computed inverting the block-A diagonal part. Test D_1 is introduced in order to make a comparison with a non-preconditioned GMRES.

Observation: In our case, it not assembled a monolithic block diagonal preconditioner, but every unknown block is separated from the others. This brings the necessity to include inside the GMRES algorithm of GetFEM++, the block multiplication.

The steps are provided in the following scheme:

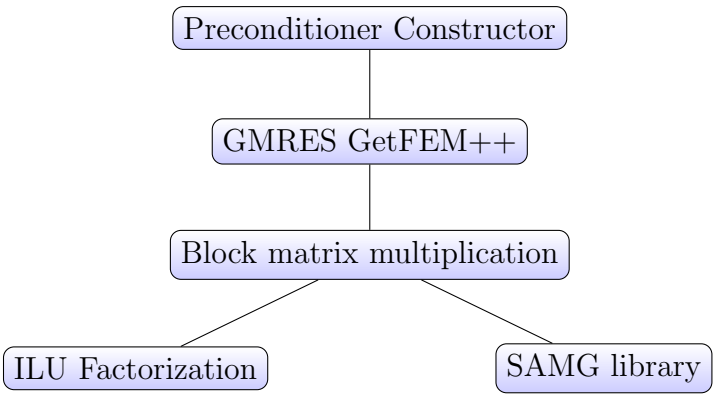

This means that after the construction of our block preconditioner, the GetFEM++ GMRES is called, then GMRES will call the new block multiplication. For the velocity block, the situation is trivial. While, for the Schur complement the block multiplication acts differently if we want to use the ILU factorization or the SAMG library. For the ILU way, we use the classical GetFEM++ ILU procedure, while for SAMG we need to construct special matrices which are compatible with the requested ones from the library. However the result is the same, a system is solved.

3.4 Preconditioned numerical solution of the multi-block coupled tissue-network problem

Trying to use the same preconditioner for the whole system introduced in the previous section, ignoring the coupling term, will not work well, in the sense that stagnation phenomena will be present in the residual evolution for the GMRES. This is due to the presence of non-diagonal block deriving from the mass source. The precondition described for Σ_3 is not anymore an optimal preconditioner for Σ_4 type system. In this case the residuals, with respect to every unknown, are correlated. Therefore we cannot solve anymore four separated systems. The idea is to perform an iterative method following the concept of Gauss-Seidel method, "decoupling" the tissue and vessel problem. The operative strategy at iteration k of our method was the following one:

1. Solving the vessel problem with a modified right-hand side, containing the extra-diagonal coupling therm between tissue and vessel pressure at step

Table 3.2: Possible solution strategies associated to the computation of the residual system for the Schur complement. Strategies with * indicate that we use a classical diagonal inversion for the residual system corresponding to the velocity unknown.

$Test$	$SuperLU_{vt}$	$SuperLU_v$	ILU_v^*	$SAMG_v^*$	ILU_t^*	$SAMG_t^*$	$Nonprec_t$
A_2	×						
B_2		×			×		
C_2		×				x	
D_2			×		×		
E_2				×		×	
F_2		×					×

$k-1$, namely:

$$\Sigma_4^A := \begin{bmatrix} \mathbf{A}_v & \mathbf{B}_v^T \\ \mathbf{B}_v & -\mathbf{C}_v \end{bmatrix} \begin{bmatrix} \mathbf{U}_v^k \\ \mathbf{P}_v^k \end{bmatrix} = \begin{bmatrix} \mathbf{F}_v \\ \mathbf{G}_v + \mathbf{Q}_{vt}\mathbf{P}_t^{k-1} \end{bmatrix} \tag{3.20}$$

2. Solving the tissue problem with a modified right-hand side, containing the extra-diagonal coupling therm between tissue and vessel pressure at step k, namely:

$$\Sigma_4^B := \begin{bmatrix} \mathbf{A}_t & \mathbf{B}_t^T \\ \mathbf{B}_t & -\mathbf{C}_t \end{bmatrix} \begin{bmatrix} \mathbf{U}_t^k \\ \mathbf{P}_t^k \end{bmatrix} = \begin{bmatrix} \mathbf{F}_t \\ \mathbf{G}_t + \mathbf{Q}_{tv}\mathbf{P}_v^k \end{bmatrix}. \tag{3.21}$$

System Σ_4^A can be solved using both direct method or preconditioned iterative method, since the dof are still much fewer that in the case of the tissue problem. For the iterative one, we can use the same block diagonal vessel preconditioner introduced for the problem Σ_2, which provide to work well.

For system Σ_4^B instead, iterative methods are preferred, because of his large dimensions. As tissue preconditioner we will use the block diagonal one, constructed for system Σ_1.

In both cases we need to separate the computation of the velocity residuals from the pressure Schur complement inside a GMRES iteration. As before the system to solve for the velocity residual is diagonal and therefore trivial. For the pressure one we have again different approaches.

Table 3.2 contains all potential scenarios. We will categorize them with label from A_2 to E_2. This categorization is going to be used even in the chapter of the numerical results. Test A_2 is refereed to solve the coupled problem with a direct SuperLU method for both Σ_4^A and Σ_4^B systems. Test B_2 and C_2 are designed to test the effect of the different preconditioned (ILU and SAMG) approach on the tissue Schur complement, while the vessel will be solved with a direct method. Test D_2 and E_2 use iterative method for both vessel and tissue problem, performing the same strategy to compute the residual system. The last test F_2 is introduced in order to show the effect of our preconditioner and compare it with GMRES method non preconditioned.

3.5 Numerical verification of the solver for the 3D problem

In order to show that we developed a good preconditioner we will test it in a setting in which the vessel and the tissue are completely uncoupled. We are going to solve the only Darcy problem in the tissue (ref. to problem Σ_1), with special boundary condition and mass source therm, namely:

$$\begin{cases} \dfrac{1}{k_t}\mathbf{u}_t + \nabla p_t = 0 & \text{in } \Omega \\ \nabla \cdot \mathbf{u}_t = g_t & \text{in } \Omega \end{cases} \tag{3.22}$$

where $g_t \in L^2(\Omega)$ is an arbitrary mass source term distributed in the volume, added in order to avoid a trivial null solution, because we are choosing to use Dirichlet homogeneous boundary condition:

$$p_t = 0 \quad on \quad \partial\Omega. \tag{3.23}$$

This choice is motivated from the coupled problem. In fact it is reasonable to consider the network as the unique source of fluid. Therefore in the case of $g_t = 0$ we will fall into the trivial solution $\mathbf{u}_t = \mathbf{0}, p_t = 0$.

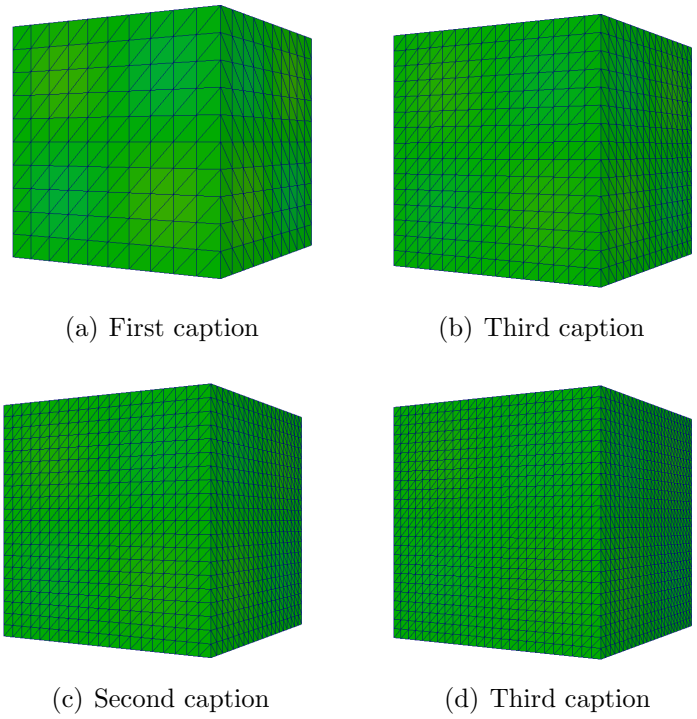

(a) First caption (b) Third caption

(c) Second caption (d) Third caption

Figure 3.3: Common figure caption.

Following the previous notation we are solving the system:

$$\begin{bmatrix} \mathbb{M}_{tt} & -\mathbb{D}_{tt}^T \\ \mathbb{D}_{tt} & \mathbb{O} \end{bmatrix} \begin{bmatrix} \mathbf{U}_t \\ \mathbf{P}_t \end{bmatrix} = \begin{bmatrix} \mathbf{0} \\ \mathbf{G}_t \end{bmatrix}, \tag{3.24}$$

where $\mathbb{M}_{tt}$, $\mathbb{D}_{tt}$ and $\mathbf{G}_t$ are:

$$\begin{aligned} [\mathbb{M}_{tt}]_{ij} &:= (\frac{1}{k_t}\boldsymbol{\varphi}_t^j, \boldsymbol{\varphi}_t^i)_\Omega, \\ [\mathbb{D}_{tt}]_{ij} &:= (\nabla \cdot \boldsymbol{\varphi}_t^j, \psi_t^i)_\Omega, \\ [\mathbf{G}_t]_i &:= (g_t, \psi_t^i)_\Omega. \end{aligned} \tag{3.25}$$

In order to make a preliminary validation of our preconditioner on a Darcy problem, we first consider a setting where the exact solution is known. We highlight that this simulation does not refer to physiological parameters and quantities.

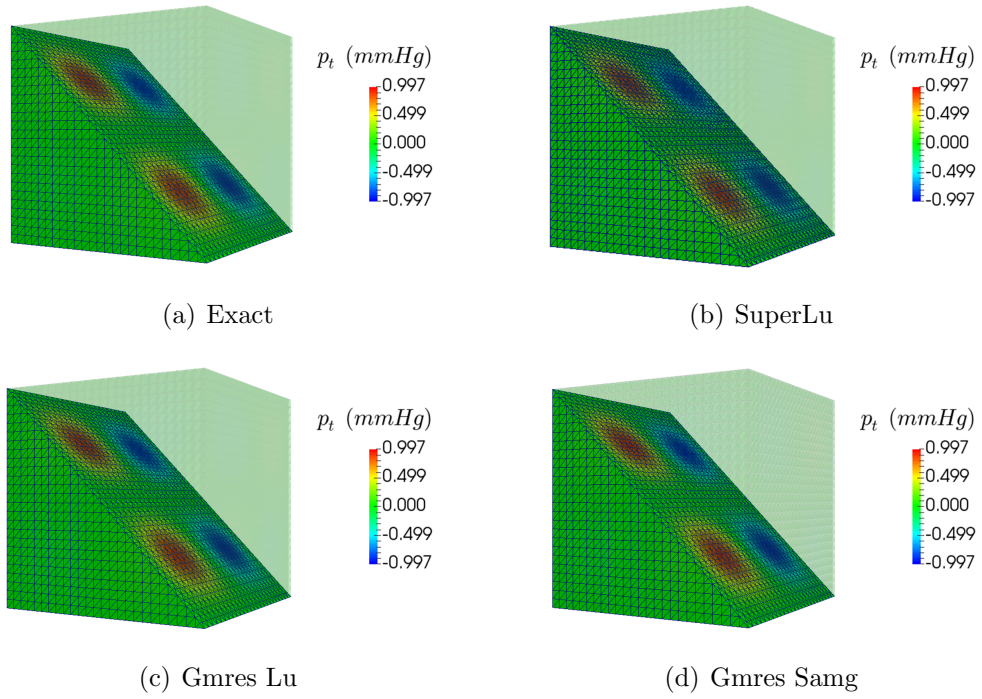

(a) Exact (b) SuperLu

(c) Gmres Lu (d) Gmres Samg

Figure 3.4: Comparison between analytical and numerical solution in terms of p_t. The results are obtained using the four different resolution approaches: SuperLU, GMRES with LU and GMRES with SAMG

The computational domain that we are going to consider is an unitary cube in $\mathbb{R}^3$, namely $\Omega = [0,1]^3$. The tissue domain is discretized using tetrahedral structure with different characteristic size h going from 1/10 to 1/25, as showed in figure 3.3.

It can be proved that the Darcy solution for the pressure in a dimensional parallelepiped $\Omega = [0, L_1] \times [0, L_2] \times [0, L_3]$ is:

$$p_t^{ex} = \sin(\frac{2\pi x}{L_1}) \sin(\frac{2\pi y}{L_2}) \sin(\frac{2\pi z}{L_3}), \tag{3.26}$$

substituting this result is the Darcy's Law we obtain the following form for the tissue velocity solution:

$$\mathbf{u}_t^{ex} = -k_t \nabla p_t^{ex} = -2\pi k_t \begin{bmatrix} \frac{1}{L_1} \sin(\frac{2\pi x}{L_1}) \sin(\frac{2\pi y}{L_2}) \sin(\frac{2\pi z}{L_3}) \\ \frac{1}{L_2} \sin(\frac{2\pi x}{L_1}) \sin(\frac{2\pi y}{L_2}) \sin(\frac{2\pi z}{L_3}) \\ \frac{1}{L_3} \sin(\frac{2\pi x}{L_1}) \sin(\frac{2\pi y}{L_2}) \sin(\frac{2\pi z}{L_3}). \end{bmatrix}, \tag{3.27}$$

We can now compute the right hand side source term as follows:

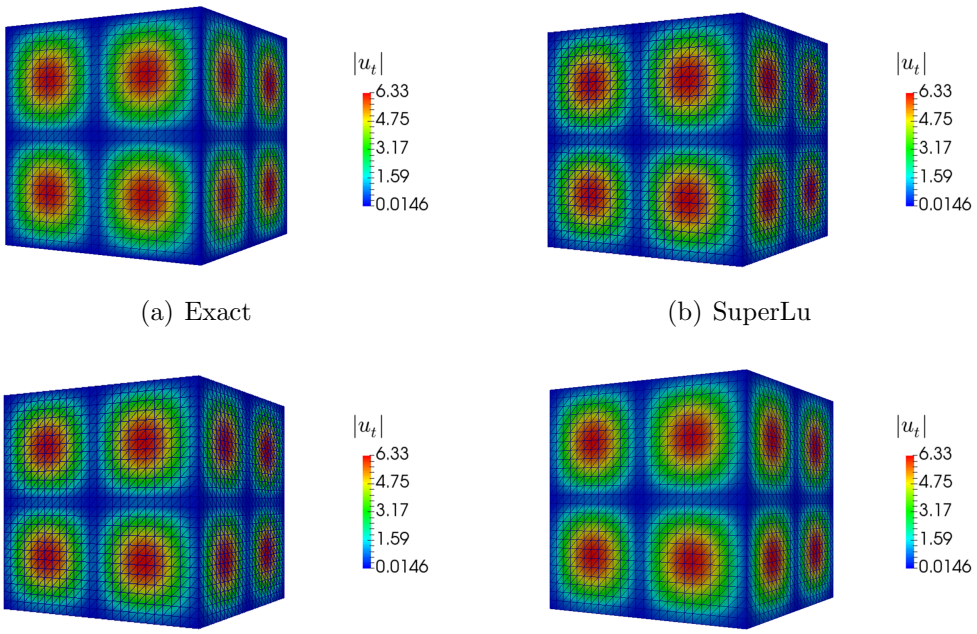

(a) Exact (b) SuperLu

(c) Gmres Lu (d) Gmres Samg

Figure 3.5: Comparison between analytical and numerical solution in terms of u_t. The results are obtained using the different resolution approaches: SuperLU, GMRES with LU and GMRES with SAMG

Table 3.3: Comparison between times for test A_1 SuperLU, test B_1 GMRES with LU inversion, test C_1 GMRES with SAMG and test D_1 GMRES not preconditioned

	10	15	20	25
A_1	3 s	38 s	4,6 min	25 min
B_1	0,07 s	3,7 s	12 s	33 s
C_1	2,25 s	18 s	17 s	37 s
D_1	2,64 s	14 s	40 s	1,3 min

$$g_t = \nabla \cdot \mathbf{u}_t^{ex} = 4\pi^2 k_t \left(\frac{1}{L_1^2} \frac{1}{L_2^2} + \frac{1}{L_3^2} \right) p_t^{ex}. \tag{3.28}$$

We observe that the previous exact pressure solution and source term fulfills the boundary condition. For this test, dimensionless parameter has been used. We consider $L_1 = L_2 = L_3 = 1$, the dimensionless permeability of the tissue unitary, $k_t = 1$ and the dimensionless conductivity of the capillary wall is null, because we are studying the only tissue Darcy problem.

All the parameter needed to construct the test case are defined we can make a comparison with four different resolution methods:

- a direct SuperLU,
- an iterative GMRES, with preconditioner described in section 3.2 for the only tissue, where the preconditioned residual system is computed using an incomplete Lu factorization,
- an iterative GMRES, with the same preconditioner, but where the preconditioned residual system is computed using the algebraic multigrid library SAMG,
- an iterative GMRES not preconditioned

In our simulation we will refer to Test A_1 for the solution computed with SupeLu, Test B_1 for GMRES that use SuperLu for compute the residual preconditioned system, Test C_1 for GMRES that use the algebraic multigrid library SAMG for the preconditioned system and Test D_1 for GMRES that is not preconditioned.

The final solution, the number of iteration and the degree of freedom are explored. In table 3.3 and 3.4 we report the computation times and the iteration

Table 3.4: Comparison between iterations for test A_1 SuperLU, test B_1 GMRES with LU inversion, test C_1 GMRES with SAMG and test D_1 GMRES not preconditioned

	10	15	20	25
A_1	-	-	-	-
B_1	78	80	80	80
C_1	132	169	158	161
D_1	894	1295	1 500	1 500

Table 3.5: List of the degree of freedom needed with different number of discretization of tissue geometry, N

	10	15	20	25
$dof\ p_t$	6 000	20 250	48 000	93 750
$dof\ u_t$	12 600	41 850	98 400	191 250

of GMRES needed respectively. As we can see the number of iterations remain almost constant, special in test B_1 and C_1, while we increase the degree of freedom, 3.5. This brings us to confirm that the preconditioner created for the only tissue uncoupled problem is an optimal preconditioner.

We report in the following figures 3.4 and 3.5 the computed solution with the four different methods and the exact solution interpolated. As we can see, there is a full coherence between the computed solution and the expected one. We notice that the pressure belongs to the interval $[-1, 1]$, while the velocity is in $[0, 2\pi]$.

Chapter 4

Application of the numerical method to Blood Flow and Hematocrit Transport

In this chapter we apply the computational model for blood flow and hematocrit transport to various test cases of increasing complexity. The simplest ones, more precisely a single capillary branch and a bifurcation, are presented to validate the predictions of the model against analytical solutions and expected behaviors. In this case, we also elucidate the sensitivity of the outcome with respect to characteristic parameters of the model, such as the curvature of the capillaries and their permeability. Later on we present a more complex, but still idealized, model for a capillary network. Using this model we investigate the ability of the model to capture the macroscopic traits of microcirculation.

4.1 Analytical and Numerical Solution

We performed a test to verify and compare the numerical solution with the analytical one. To this purpose a mesh for interstitial domain equal to 11x11x11 was used and parameters and boundary conditions reported in Table 4.1 and 4.2 were employed. To obtain the analytical solution for u_v we considered the two

SYMBOL	PARAMETER	UNIT	VALUE	REF.
d	characteristic length	m	1×10^{-4}	[17]
D	characteristic length of the domain	m	$= L = 1 \times 10^{-4}$	[17]
R	average radius	m	4×10^{-6}	[37]
k	tissue hydraulic conductivity	m^2	1×10^{-18}	[?]
μ_t	interstitial fluid viscosity	cP	1.2	[36]
μ_v	blood viscosity	cP	Pries formula	[25]
L_p	wall hydraulic conductivity	$m^2\,s\,kg^{-1}$	10^{-12}	[?]
P	characteristic pressure	Pa	133.32	[?]
U	characteristic velocity	$m\,s^{-1}$	1×10^{-3}	[24]
$\Delta\pi$	oncotic pressure gradient	$mmHg$	25	[32]
σ	reflection coefficient	$[-]$	0.95	[16]

Table 4.1: Physiological parameters used for all the numerical tests (unless differently specified).

equations of the coupled system defined in the vessel domain

$$\begin{cases} \frac{\pi R'^2}{\kappa_v}\left(1 + \kappa_i'^2(s)\mathrm{R}_i'^2\right)\bar{u}_v + \partial_s \bar{p}_v = 0 & \text{in} \quad \Lambda \\ \partial_s \bar{u}_v + \frac{1}{\pi R'^2}\, Q[(\bar{p}_v - \bar{\bar{p}}_t) - \sigma(\pi_v - \pi_t)] = 0 & \text{in} \quad \Lambda \end{cases} \tag{4.1}$$

The value of $\bar{\bar{p}}_t$ is dependent on the arc length s and it is determined using the other two equations of the system. To overcome the complexity of the coupling of the equations we considered a constant p_t near to the vessel, choosing a high value of tissue hydraulic conductivity k equal to $1 \times 10^{-8}\, m^2$. In this way $p_t = const = p_0$ and $\bar{\bar{p}}_t = p_0$.

Substituting u_v from the first equation to the second one we obtain a non homogeneous second order differential equation:

$$\begin{cases} \frac{\partial^2 \bar{p}_v}{\partial s^2} - \frac{Q}{k_v}\big(1 + \kappa_i'^2(s)\mathrm{R}_i'^2\big)\bar{p}_v(s) = -\frac{Q}{k_v}\big(1 + \kappa_i'^2(s)\mathrm{R}_i'^2\big)[\bar{\bar{p}}_t + \sigma(\pi_v - \pi_t)] \\ \bar{p}_v(s=0) = 32 \\ \bar{p}_v(s=1) = 28.5 \end{cases} \tag{4.2}$$

If $Q = 0$ the solution of the problem coincides with Poiseuille's Law. In fact the equation (4.2) is reduced to:

$$\begin{cases} \frac{\partial^2 \bar{p}_v}{\partial s^2} = 0 \\ \bar{p}_v(s=0) = 32 \\ \bar{p}_v(s=1) = 28.5. \end{cases} \tag{4.3}$$

and returns a linear function for $p_v(s)$, figure 4.5, and substituting it in the first equation of (4.1) a constant velocity along the vessel is obtained.

To get the analytical solution of (4.2) with $Q \neq 0$ we first found the solution of the corresponding homogeneous equation, namely:

$$\begin{cases} \frac{\partial^2 \bar{p}_v}{\partial s^2} - \frac{Q}{k_v}\big(1 + \kappa_i'^2(s)\mathrm{R}_i'^2\big)\bar{p}_v(s) = 0 \\ \bar{p}_v(s=0) = 32 \\ \bar{p}_v(s=1) = 28.5 \end{cases} \tag{4.4}$$

The characteristic equation of (4.4) is:

$$r^2 - \frac{Q}{k_v}\big(1 + \kappa_i'^2(s)\mathrm{R}_i'^2\big) = 0 \tag{4.5}$$

which solution are $r = \pm\sqrt{\big(Q\big(1 + \kappa_i'^2(s)\mathrm{R}_i'^2\big)\big)/k_v}$. So the complementary solution is:

$$p_v(s) = Ae^{-\sqrt{\frac{Q(1+\kappa_i'^2(s)\mathrm{R}_i'^2)}{k_v}}} + Be^{\sqrt{\frac{Q(1+\kappa_i'^2(s)\mathrm{R}_i'^2)}{k_v}}} \tag{4.6}$$

Imposing the boundary conditions we obtained $A = 367.18$ and $B = 357.93$. To solve the non homogeneous equation we called $Y = C$ a constant function of s, so $\frac{\partial^2 Y}{\partial s^2} = 0$. We substituted Y in the equation (4.2):

$$0 - \frac{Q(1+\kappa_i'^2(s)\mathrm{R}_i'^2)}{k_v}C = -\frac{Q(1+\kappa_i'^2(s)\mathrm{R}_i'^2)}{k_v}[\bar{p}_t + \sigma(\pi_v - \pi_t)] \tag{4.7}$$

$$\Rightarrow C = [\bar{p}_t + \sigma(\pi_v - \pi_t)] = 22.75. \tag{4.8}$$

Finally the analytical solution with the parameters in Table 4.1 and 4.2 will be:

- rectilinear single branch, $k = 0$:

$$\bar{p}_v(s) = 367.18e^{-0.005s} - 357.93e^{0.005s} + 22.75 \tag{4.9}$$

- curve single branch, $k = 0,6$:

$$\bar{p}_v(s) = 366.235e^{-0.00483s} - 356.985e^{-0.00483s} + 22.75 \tag{4.10}$$

- curve single branch, $k = 0,11$:

$$\bar{p}_v(s) = 364.365e^{-0.00485s} - 355.115e^{-0.00485s} + 22.75 \tag{4.11}$$

Substituting (4.9),(4.10) and (4.11) in the first equation of (4.1) we obtain the following form for the vessel velocity:

- rectilinear single branch, $k = 0$:

$$\bar{u}_v(s) = 5.08e^{-0.005s} + 4.96e^{0.005s} \tag{4.12}$$

- curve single branch, $k = 0,6$:

$$\bar{p}_v(s) = 5.04498e^{-0.00483s} - 4.91756e^{-0.00483s} \tag{4.13}$$

- curve single branch, $k = 0,11$:

$$\bar{p}_v(s) = 4.99775e^{-0.00485s} - 4.87087e^{-0.00485s} \tag{4.14}$$

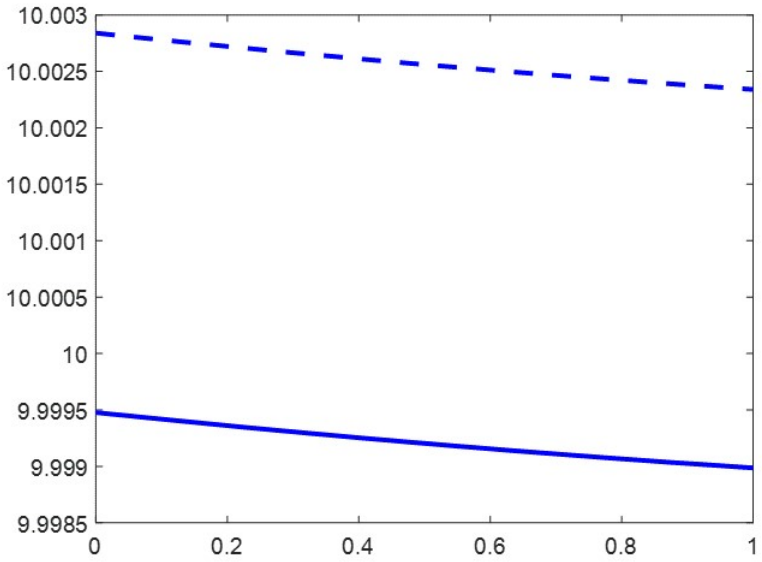

Figure 4.1: Comparison between analytical (dashed line) and numerical solution (continuous line) in terms of u_v in the case $k\,R = 0$ and $Lp = 10^{-12}\,m^2 s\,kg^{-1}$

The comparison between analytical and numerical solution in terms of u_v are shown in Figure 4.1 for the rectilinear case and in Figure 4.2 for the low curve branch. For this simulation the vessel conductivity $L_p = 10^{-12}\,m^2\,s\,kg^{-1}$ (the mean error between the two solutions is equal to 0.00%).

We also performed another test decreasing the wall hydraulic conductivity to $L_p = 0\,m^2 s\,kg^{-1}$, in order to nullify the filtration along the vessel. The velocity analytical solutions of this cases will be constant, while the pressures are linear. The comparison between the analytical and computed solution for the velocity is shown in figure 4.3. Here, we present the solutions computed and the analytical ones, in terms of u_v, between the cases $k\,R = 0$, $k\,R = 0.6$, $k\,R = 0.11$ when $Lp = 0\,m^2 s\,kg^{-1}$. The velocity magnitude decreases with the curvature, because curved vessels oppose higher resistance to flow. We observe that this behavior is

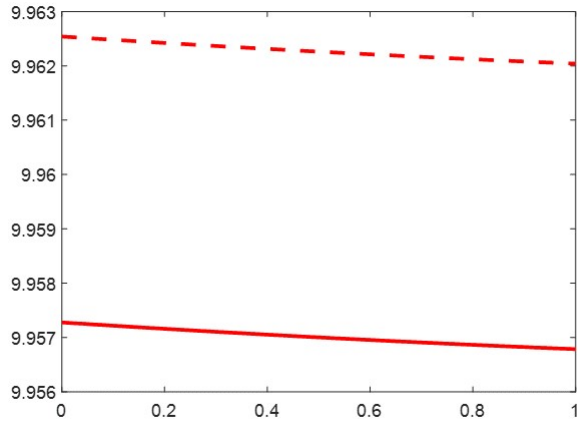

Figure 4.2: Comparison between analytical (dashed line) and numerical solution (continuous line) in terms of u_v in the case $k\,R = 0,6$ and $Lp = 10^{-12}\,m^2 s\,kg^{-1}$

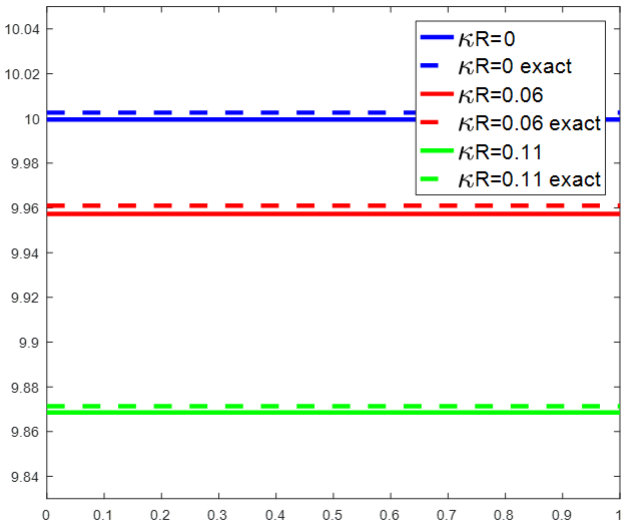

Figure 4.3: Solutions computed in terms of u_v between the cases $k\,R = 0$, $k\,R = 0,6$, $k\,R = 0,11$ when $Lp = 0\,m^2 s\,kg^{-1}$

correctly captured by the model.

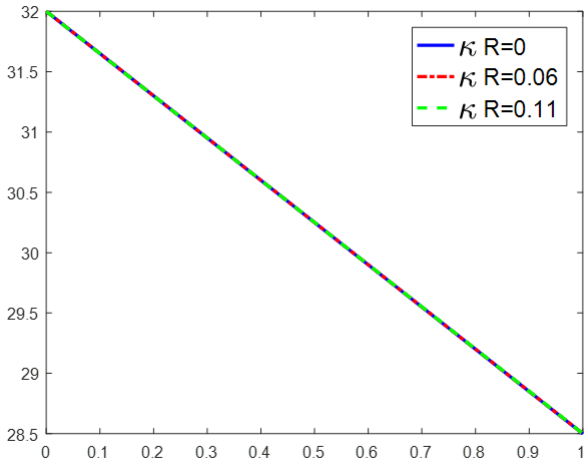

Figure 4.4: Solutions computed in terms of p_v between the cases $k\,R = 0$, $k\,R = 0,6$, $k\,R = 0,11$ when $Lp = 0\,m^2 s\,kg^{-1}$

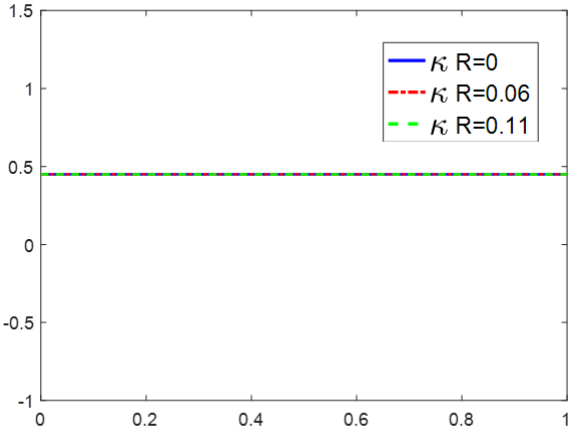

Figure 4.5: Solutions computed in terms of H_v as function as the between the cases $k\,R = 0$, $k\,R = 0.6$, $k\,R = 0.11$ when $Lp = 0\,m^2 s\,kg^{-1}$

4.2 Single capillary branch case

We present simulations of blood flow in a single branch of capillary vessel, interacting with the surrounding tissue, modeled as a homogeneous porous medium. For this idealized experiment we consider a tissue sample represented by a cube of 100 μm side. A single capillary branch crosses the tissue sample

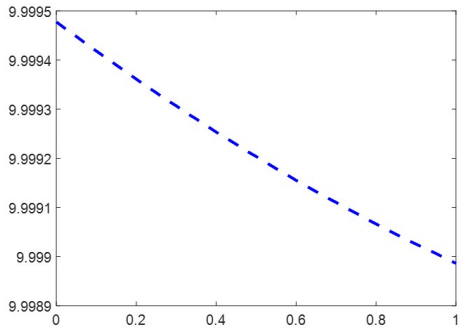

(a)

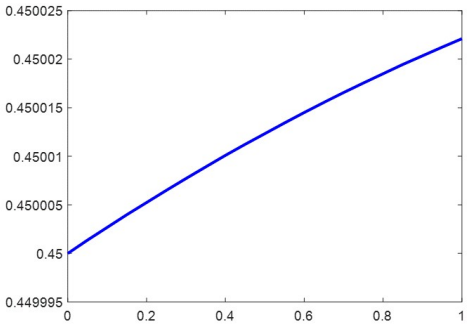

(b)

Figure 4.6: Solutions computed in terms of u_v and H for the case $k\,R = 0.6$ when $L_p = 10^{-12}\,m^2\,s\,kg^{-1}$. Above (a) we represent the velocity, while below (b) the hematocrit.

from side to side. Different capillary shapes are considered, as showed in figure 4.7, we simulate a straight segment fig. 4.7(a), a circular arc with intermediate curvature fig. 4.7(b) (such that κR, a dimensionless parameter is equal to 0.06) and a circular arc with high curvature figure 4.7(c) (such that $\kappa R = 0.11$, shown in Figure 4.8). All this branches have the same unitary length, therefore they are exposed at the same pressure gradient along the capillary extremes.

We are going to visualize the results for pressure, velocity, hematocrit and viscosity in the only high curved case. The other cases have the same behavior, what will change will be the value.

The velocity profile for a curved pipe with $\kappa R = 0.11$ is visualized in Figure

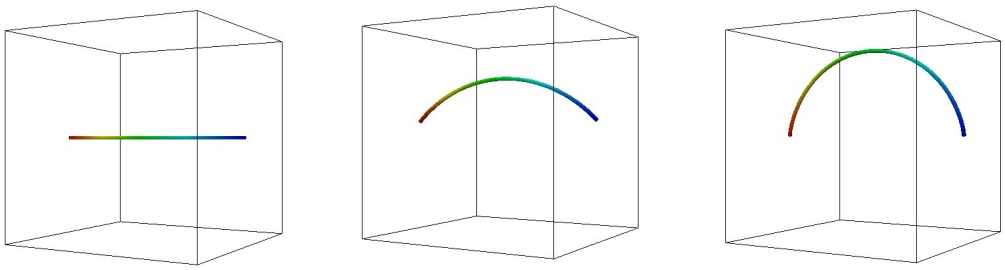

(a) (b) (c)

Figure 4.7: Geometrical configurations of the test cases, increasing the curvature from $k\,R = 0$ (a), to $k\,R = 0.6$(b) and $k\,R = 0.11$ (c).

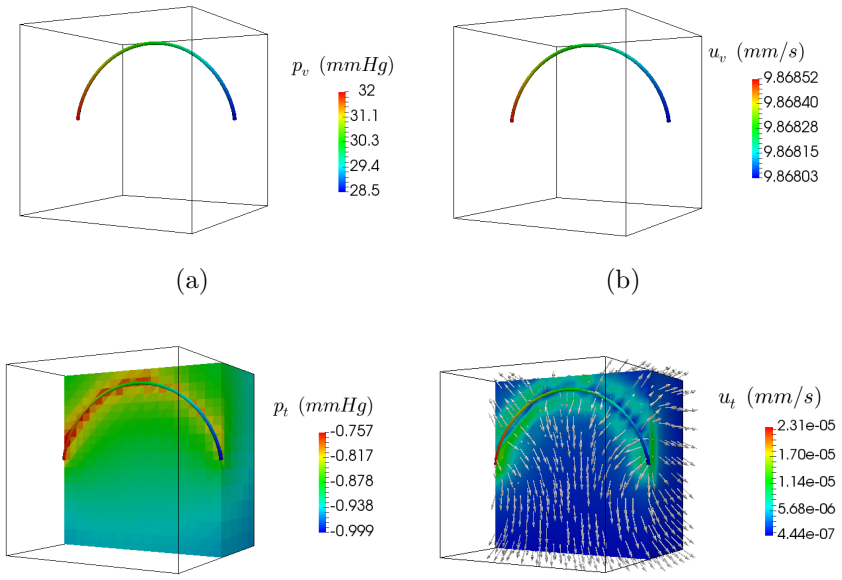

(a) (b)

(c) (d)

Figure 4.8: Pressure and velocity for vessel and tissue respectively, (a) vessel pressure, (b) vessel velocity, (c) tissue pressure visualised

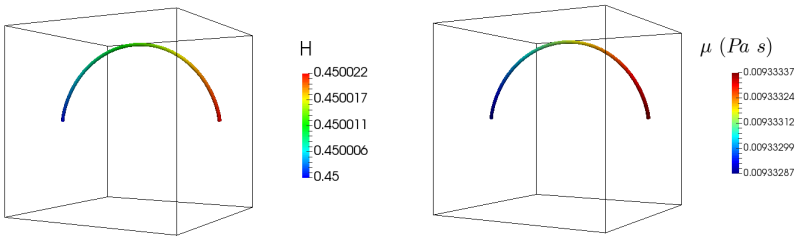

(a) (b)

Figure 4.9

4.8. We observe it looses symmetry with respect to the axis of the channel. The parameters of the model adopted in the simulations are collected (with description, units and sources) in Table 4.1.

Concerning the boundary conditions, we apply the pressure at the endpoints of the network, the hematocrit discharge at the corresponding inflow points and we allow for fluid exchange at the artificial interfaces that separate the tissue sample with the exterior. The latter effect is described by a condition of type

$$\mathbf{u}_t \cdot \mathbf{n}_t = \beta_t(p_t - p_0),$$

where β_t is the hydraulic conductivity of the tissue matrix and p_0 denotes a far field pressure. The data and parameters used for boundary conditions are reported in Table 4.2. In particular, the value of the pressure drop is determined on the basis of a prescribed value of the blood flow velocity in small capillaries. Assuming $u_v \simeq 1\, mm/s$, the blood flow rate through a capillary with $R = 4\,\mu m$ is

$$Q_b = \pi R^2 u_v = 5.03 \cdot 10^{-14}\, m^3/s. \tag{4.15}$$

Using (4.15), $\mu \simeq 9.33\, cP$ [25] and Poiseuille's law, with the hypothesis of no transcapillary flow, the pressure drop between the inlet and the outlet of the capillary will be equal to,

$$\Delta p_v = Q_b \frac{8\mu L}{\pi R^4} = 3.5\, mmHg. \tag{4.16}$$

Finally, we need to determine inlet and outlet pressures. This choice depends on the position of the capillary segment in the microvasculature. To this purpose,

we define $\bar{p}_v^*$ as the value of $\bar{p}_v$ for which the net filtration pressure is zero (for an average tissue pressure equal to the far field pressure p_0): if $\bar{p}_v > \bar{p}_v^*$ will be a net fluid filtration, while if $\bar{p}_v < \bar{p}_v^*$ will be a net fluid absorption. Considering parameters in Table 4.1 and constant interstitial pressure $p_t \simeq p_0 = -1$, we obtain,

$$\bar{p}_v^* = p_0 + \sigma\Delta\pi = -1 + 0.95 \cdot 25 = 22.75\, mmHg.$$

On the basis of the observation that the microvascular pressure ranges between 32 and 15 $mmHg$ (see [32]) this value, for a vessel near the arteriolar end of the capillary network, we set $p_{inlet} = 32\, mmHg$ and $p_{outlet} = 28.5\, mmHg$, such that both values are above $\bar{p}_v^*$. For a portion of capillary near the venular end we set $p_{inlet} = 18.5\, mmHg$ and $p_{outlet} = 15\, mmHg$. In the latter case we expect that the capillary will absorb fluid from the exterior.

SYMBOL	B.C.S	UNIT	VALUE	REF.
ΔP	hydrostatic pressure drop	$mmHg$	3.5	[32]
p_0	far field pressure	$mmHg$	-1	[**?**]
β_t	tissue conductivity	$-$	$\kappa_t/D' = 1.1 \cdot 10^{-5}$	[**?**]
H_0	hematocrit at inlet of capillary	$-$	0.45	[14]

Table 4.2: Data and parameters for the boundary conditions in the capillary and tissue regions

As already introduced, we show in figure 4.3 the computed and analytically determined values of the velocity magnitude. In this cases the analytical solution is available for pressure (fig. 4.4), velocity (fig. 4.3) and hematocrit variation (fig. 4.5) along the axis of the capillary, in case of impermeable capillary walls.

The hematocrit profile can then be easily determined if an analytical formula for the velocity is known, because the hematocrit discharge is constant along the pipe, namely $H(s)\bar{u}_v(s) = H_{inlet}\bar{u}_{v,inlet}$. The comparison of the numerical and analytical solution provides a verification of the numerical algorithm as well as a preliminary validation of the computational model.

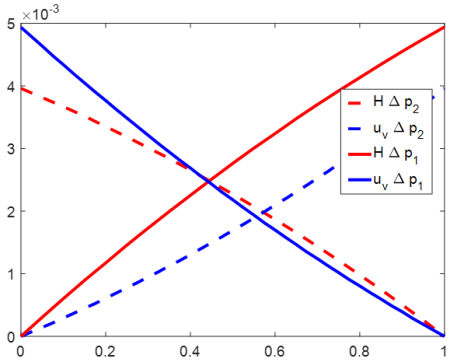

Figure 4.10

Figure 4.11: Percentage variation of the velocity magnitude (dashed line) and hematocrit (continuous line) along the capillary axis for the straight permeable capillary. Blue lines correspond to the arterial end while red lines refer to the venular end

When we switch on the capillary permeability and we allow for plasma leakage from the capillary to the interstitial tissue, the flow and hematocrit profiles change in both regions. If we consider a capillary segment near the venular end, due to overpressure in the interstitial volume with respect to the capillary, there is negative leakage and the capillary flow rate increases accordingly. As a consequence of augmented plasma flow rate, the discharge hematocrit slightly decreases. Opposite trends are observed for a capillary segment closer to the arteriolar end. This behavior is showed in figure 4.11, where the continuous line correspond to the velocity and dashed line to the hematocrit, while red and blue represent the arteriolar and venular end, respectively.

In order to complete the discussion about this basic case, we show the results for the only high curved branch, using the pressure gradient corresponding to an arteriolar end. In figure 4.8 (a) and (b) we show the variation of pressure and velocity along the capillary axis. Whereas, in figure 4.8 (c) and (d) we present the tissue pressure and velocity. We can see that far from the vessel, the interstitial pressure is almost unaffected by the presence of the vessel source, while in the surrounding tissue the pressure follows the same behavior of the vessel: higher at

the vessel inlet and lower at the outlet. Regarding the tissue velocity, the vectors are represented on a cross section of the tissue sample, on top of the contour plot of the velocity magnitude. The effect of leakage from the vessel is well visible.

In figure 4.9 (a) we show the vessel hematocrit and viscosity. As already introduced, the hematocrit tendency is inverse to the velocity one. Therefore it increases along the vessel. In figure 4.9 (b) instead, we present the viscosity. We can see has the values it is not constant, this is because the changes in hematocrit modify its value.

4.3 Y-shaped bifurcations

This test case is useful to evaluate the accuracy of the computational model in the description of the Fahraeus-Lindqvist effect, that is the variation of apparent viscosity due to rearrangement of red blood cells in the flow, and the plasma skimming effect, that is the asymmetric distribution of hematocrit when channels downstream a bifurcation are different. These phenomena mostly depend on the geometrical configuration of the vascular network, while the permeability of the capillary walls weakly affects them. For this reason, we perform all the computational tests for bifurcations in the case of impermeable walls, namely we set $L_p = 0$. All the remaining parameters and boundary conditions are the ones of Tables 4.1 and 4.2.

The geometrical model consists of a Y-shaped bifurcation, where all branches have the same length. The radii of the daughter branches are calculated on the basis of the Murray's law, that is $R_1^3 = R_2^3 + R_3^3$, where index (1) denotes the parent vessel and (2), (3) are the daughter channels. Unless differently specified, the daughter branches have equal radius, namely $R_2 = R_3$, which allows us to determine $R_2 = R_3$ as a function of R_1 as in Table 4.1. The current model is not sensitive to the angle of the daughter branches.

First, we analyze the role of curvature on the distribution of flow rate, discharge hematocrit and viscosity downstream to a bifurcation. The results of simulations are collected in Figure 4.12. We notice that curvature increases the resistance to flow which in turn affects the distribution of blood flow rate and discharge hematocrit at the bifurcation. Differences with respect to the symmetric case are

	straight			curved $\kappa R = 0.06$			curved $\kappa R = 0.11$		
branch	1	2	3	1	2	3	1	2	3
$\bar{u}_v$	0,6559	0.5221	0.5221	0.4048	0.3609	0.3588	0.4025	0.3607	0.3549
H	0.4500	0.4500	0.4500	0.4500	0.4509	0.4491	0.4500	0.4526	0.4474
H discharge	0.00093	0.0119	0.0119	0.0093	0.0128	0.0128	0.0093	0.0129	0.0127
Balance	-1.756E-09			1.001E-09			2.522E-09		

Table 4.3: For the text cases of Figure 4.12 we report the representative (mean) values of velocity ($\bar{u}_v$), hematocrit (H) and discharge hematocrit. The residual of the hematicrit dscharge balance (value (1) = value (2) + value (3)) is reported at the borrom row.

rather small, approximately of 1% for each quantity. However, we remind that we are considering a small portion of a normal capillary, namely the characteristic length is only $100\mu m$. For the more extended vasculature models, the difference will be amplified by the geometrical scale factor. Thanks to the fact that we consider impermeable capillary walls, we observe that mass balance at the bifurcation point is trivially verified by looking at flow rates and discharge hematocrit at the endpoints of the network. As it appears from Table 4.3, the balance of these quantities at the junctions of the network is satisfied within the tolerance of the numerical discretization.

As regards the viscosity, reported in the bottom row of Figure 4.12, we first verify that the predictions of the computational model are coherent with formula (1.23), also visualized in Figure 1.4. We observe that viscosity increases downstream to the bifurcation, even though the hematocrit sightly decreases in the bottom branch (because of increased resistance to flow). This is however in agreement with the model, because viscosity is highly sensitive to the variation of the capillary radius. Since this parameter decreases from 4 μm in the parent branch to 3.17 μm in the daughter branches, viscosity correspondingly increases (see Figure 1.4 for a visualization of this effect).

In Figure 4.13, we study the influence of the capillary radii (or diameters) of the daughter branches on the velocity, hematocrit and viscosity. More precisely, we progressively increase the radius of the upper daughter branch of 5% and 10%, while we decrease the radius of the lower branch of the same amount. This analysis confirms that blood velocity, hematocrit and viscosity are subject to a complex interaction at a bifurcation. More precisely, braking the symmetry of the daughter vessel branches, generates significant variations on the blood flow rate, hematocrit and viscosity downstream to the bifurcation.

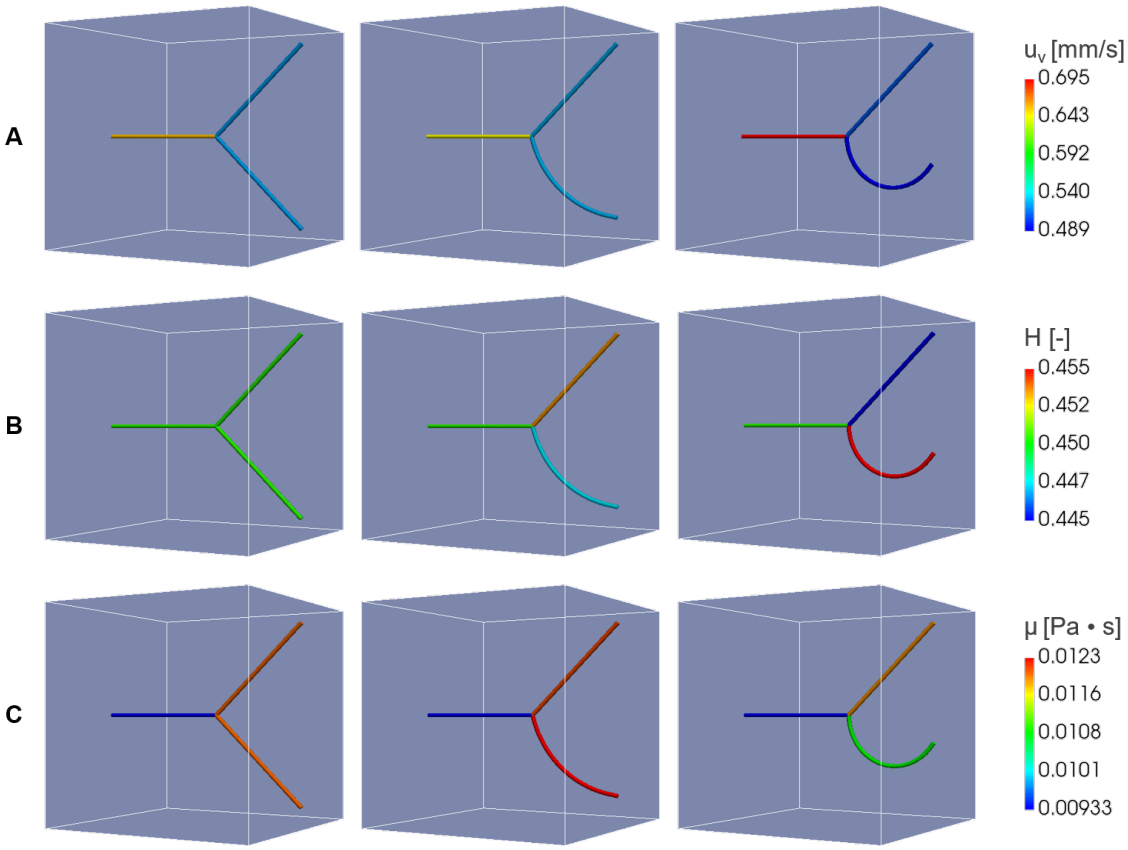

Figure 4.12: The top row (panel marked with A) shows the distribution of velocity in the bifurcation, for increasing levels of curvature $\kappa R = 0;\ 0,06;\ 0,11$, from left to right. We point out that all curved branches have the same length, such that the variation of resistance is only due to curvature. The middle row (marked with B) shows the corresponding variation of hematocrit in terms of % variation with respect to the nominal value 45%. In the bottom row (marked with C), we show the apparent viscosity, which is affected by variation of hematocrit and capillary diameter according to (1.23), see also Figure 1.4.

	reference			5%			10%		
branch	1	2	3	1	2	3	1	2	3
R	0.04	0.0317	0.0317	0.04	0.0333	0.0302	0.04	0.0349	0.0286
$\bar{u}_v$	0.6559	0.5222	0.5222	0.6687	0.5679	0.4826	0.6973	0.6165	0.4459
$\%\bar{u}_v$				1.95%	8.76%	-7.58%	6.31%	18.07%	-14.60%
H	0.4500	0.4500	0.4500	0.4500	0.4802	0.4067	0.4500	0.4979	0.3513
$\%H$				0.00%	6.72%	-9.61%	0.00%	10.65%	-21.93%
μ	0.0093	0.0120	0.0120	0.0093	0.0120	0.0116	0.0093	0.0118	0.0110
$\%\mu$				0.00%	0.25%	-2.97%	0.00%	-1.32%	-8.38%

Table 4.4: Quantitative analysis of the simulations illustrated in Figure 4.13.

A quantitative analysis of these effects is reported in Table 4.4. From the analysis of flow rates we see that the ±5% and ±10% variation of the radius increases the flow rate through the system of approximately the same percentage. Concerning hematocrit, we observe that its variations are amplified with respect to the magnitude of the perturbation. More precisely, because of the plasma skimming effect, red blood cells hardly flow into the daughter branch with smaller radius. For this reason, hematocrit is significantly smaller in the branches where the radius has been decreased than in the ones where it was increased. The behavior of viscosity is less apparent, but still in line with the model. Indeed, we see that the trend changes from perturbations of 5% with respect to 10%. This behavior can be interpreted using Figure 1.4, where we see that for small capillary radius, viscosity increases with hematocrit and decreases with capillary diameter. Our interpretation of Table 4.4 is that for perturbations of 5% the effect of diameter dominates on the effect of hematocrit, with for 10% perturbations, the variation of hematocrit is large enough to influence the change of viscosity in the same way. All these considerations suggest that the interaction between radius, flow rate, hematocrit and viscosity is highly nonlinear and hardly predictable with simple models that do not take into account their combined effects.

4.4 Comparative studies on a realistic microvascular network

In this section we use the computational model to simulate flow and hematocrit transport in a fairly complex and realistic model of microvascular network. The

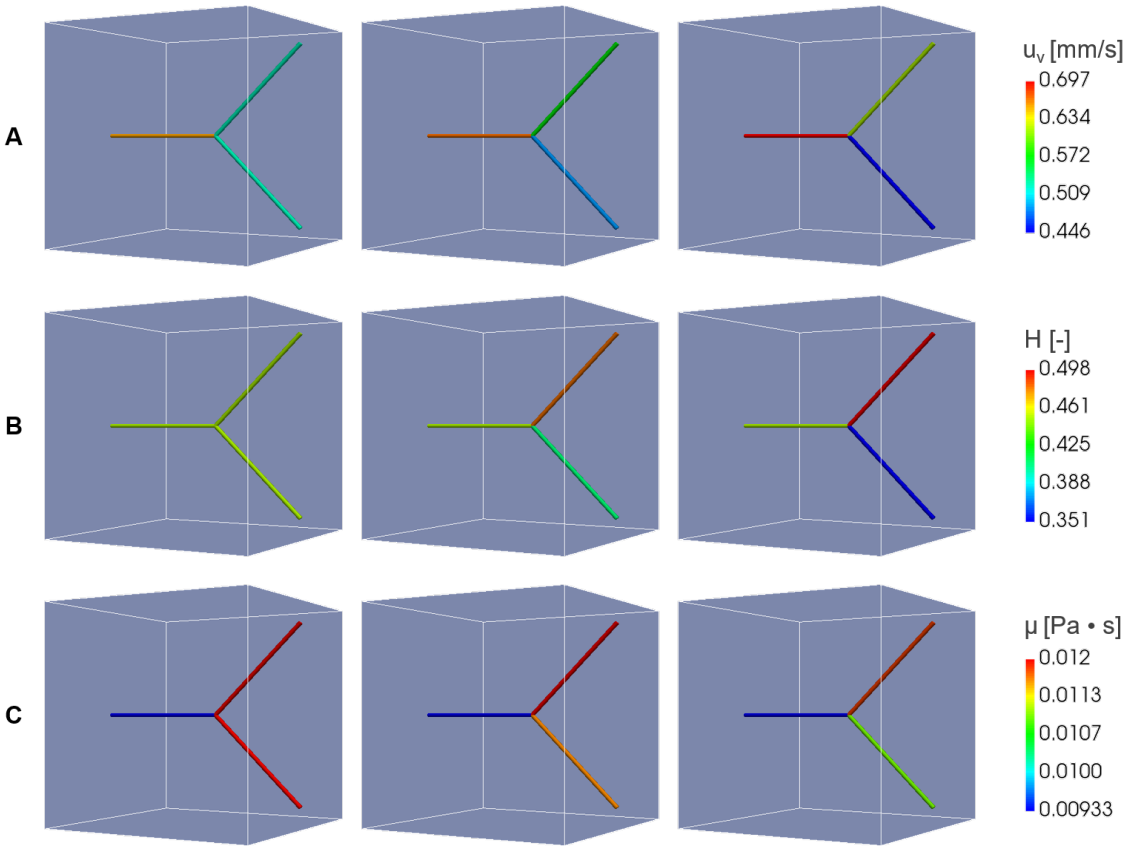

Figure 4.13: Velocities (panel A), hematocrit % variation with respect to the nominal value of 45% (penel B) and effective viscosity (panel C) are reported from top to bottom. In the first column, the daughter branches have equal radii $R_2 = R_3 = 3.17\mu m$. In the second column the radius of the upper branch is increased of 5% with respect to the nominal value while the one of the lower branch is decreased of the same amount. In the third column, the perturbation of the radii is $\pm 10\%$

section is subdivided in two parts. First we describe the procedure developed to generate artificial but realistic networks, second we discuss the numerical simulations of flow and hematocrit transport obtained with the computational model.

4.4.1 A generator of artificial vascular networks

The network that we have generated here satisfies the following criteria:

1. the morphology of the network respects the optimal distribution of a Voronoi tassellation;

2. the aspect ratio of each branch (L_i/R_i) is large enough to justify the one-dimensional flow assumption;

3. the radii of branches merging at any junction satisfy Murray's law;

4. the surface to volume density of the capillaries satisfies the physiologic value of $S/V = 7000$ m^{-1} [**?**];

The generation of such network is a complex (nonlinear) iterative procedure that is summarized below. We consider a representative cube of 500 μm side, because this is the typical length of a capillary vessel from the arteriolar to the venular end. We notice that the characteristic size of the cube has increased 5 times with respect to the previous cases (where it was equal to 100 μm). As we will explain later, this change also influences the boundary conditions for the vasculature, spanning the entire pressure range of microvasculature form 32 to 15 $mmHg$. The morphology of the network in such representative volume has been obtained by stacking several slabs containing a quasi-planar network.

Following previous works [30, 31], each planar network has been obtained using a biomimetic design based on the Voronoi tassellation model, which defines a partitioning of a plane into regions, based on the distance to seed points distributed on a subset of the plane. The edges of the Voronoi tassellation are equidistant to the seed points of the neighboring regions. Thank to this property, the Voronoi partition may be considered to be a reasonable model for the distribution of capillaries, which should fill a biological tissue in a way to maintain equal distance to the cells that populate that portion of tissue. The main parameter that influences the

morphology of the network is then the number of seed points. We have screened several network configurations spanning from 5 to 15 seeds and we decided to use networks arising from random distributions of 8 points on a 500 μm side square. This number of points is sufficiently small to guarantee an aspect ratio of the channels that is sufficiently high (about $L_i/R_i = 4$), given an average radius of the branches of 4 μm. By randomly varying the distribution of 8 points, we have generated 100 different network configurations that satisfy the criterion on aspect ratio.

The second step consists of assigning to each branch a suitable radius that respects the Murray's law together with the additional physiological constraints of having a distribution of radii in the range $2 - 6$ μm with mean value, defined as $\sum_i R_i L_i / \sum_i L_i$, equal to 4 μm $\pm 5\%$.

This task is achieved through the following procedure. We initialize the network with a uniform radius of 4 μm for every branch. Then we iterate among the following steps:

1. calculate the flow along the network, for suitable arteriolar and venular pressures. This step determines the connectivity of the network with respect of the flow and it allows us to identify bifurcations and anastomoses among all junctions. Finally, for any bifurcation, we randomly assign a flow split a, defined below;

2. we apply the Murray's law:

$$\begin{aligned} &\text{bifurcation} \quad R_{in}^3 = R_{out,1}^3 + R_{out,2}^3; \quad \text{for a given flow split } a = \frac{R_{in}}{R_{out,1}} \\ &\text{anastomosis} \quad R_{in,1}^3 + R_{in,2}^3 = R_{out}^3; \end{aligned}$$

and we iterate until the connectivity of the network does not change from one step to the next. Since the flow split at bifurcations is a random variable, this procedure is not deterministic and it gives a different outcome at any run. This procedure was applied 100 times to each of the 100 networks morphologies obtained before. The procedure was also repeated with initial radii of $4, 4.5, 5$ μm for a total of 3×10^4 possible configurations. Finally, we have discarded the ones with radii outside the interval $2 - 6$ μm and with a mean value of radius not equal to 4 μm $\pm 5\%$, ending up with about 10^4 valid configurations.

In this way we have obtained a large population of planar networks that satisfy the first three criteria described above. The three-dimensional network configuration with a physiologic surface to volume density is obtained by stacking a suitable number of planar networks one above the other. After some preliminary calculations and numerical verifications, it is apparent that superposing 18 admissible planar networks on top of each other provides a surface to volume ratio of approximately 7000 m^{-1}, as desired. Each of these slabs results to be $\Delta = 27.8$ μm thick. Every network can be randomly chosen among the database of $\simeq 10^4$ configurations obtained by means of the previous procedure. To avoid perfect planarity, unlikely to be observed in reality, we have placed each network in the central plane of the slab and perturbed the vertical coordinate of the network nodes of a random quantity less equal to $\Delta/2$. This construction also facilitates the definition of boundary conditions on the network, because 2 of the 6 faces of the cube, precisely the ones parallel to the network planes, do not intersect the network branches. The remaining 4 faces (called lateral faces of the cube) are subdivided in two neighboring arteriolar faces and two neighboring venular ones. At the arteriolar endpoints of the network we set 32 $mmHg$ while at the venular ends we have 15 $mmHg$. The corresponding pressure drop drives the flow along the network.
In conclusion, this protocol allows for a great variability, but is controlled by a fairly small number of parameters that we have optimized in order to satisfy the physiological criteria listed above. One of these realistic configurations is the one used for the simulations discussed in the next section. In particular, we show in Figure 4.14 the morphology of the network and the distribution of the radius.

4.4.2 Calculation, visualization and analysis of blood flow and hematocrit transport in realistic models of microvasculature

The numerical simulations have been carried out using the finite element solver described in Chapter 1. The geometrical model consists of 250 vascular branches with 80 nodes on each branch, for a total of 20×10^3 nodes in the network. The interstitial volume is discretized with a uniform tetrahedral mesh obtained by distributing 21 points along each edge of the cube and consisting of approximately $50\,10^3$ tetrahedral elements.

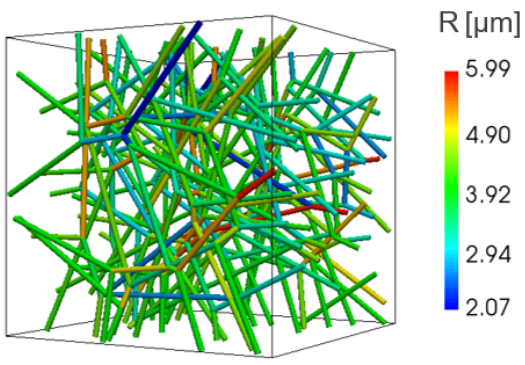

Figure 4.14: Visualization of the the morphology of the network and the distribution of the radii (mm).

The discrete model is transformed into a system of linear equations for the physical unknowns p_v, p_t, u_v, u_t, corresponding to $20\times20^3, 50\times10^3$, 40×10^3, 100×10^3 degrees of freedom, respectively. This is a fully coupled, block structured linear system that is solved by means of the GMRES iterative solver, accelerated by a block preconditioner based on the Schur complement of the pressure problems. The performance of this approach will be discussed in the next chapter. However, this is not the total time necessary to perform the simulations shown below, because the Fahraeus-Lindqvist and plasma skimming effects make the problem become nonlinear. The iterative approach described in Chapter 1 is applied here and the linear system described above is solved once for every iteration.

Figure 4.15 shows the main outputs of the model. On the top left panel we see that pressure in the network progressively decreases from the arteriolar to the venular ends of the microvasculature, as prescribed. The blood velocity (shown in the top right panel), however, is not uniformly distributed and several network branches are crossed by a flow rate significantly lower than the average (i.e. the dark blue color).

Concerning the interaction of the microvasculature with the interstitial flow, we observe that the variation of pressure through the capillary bed influences the pressure in the interstitial space. This is shown in the middle left panel, by the cross section of the interstitial pressure. We see that in proximity of the arteriolar end of the network, an increased interstitial pressure level is visible, while it decreases below average next to the venules. Then, it is apparent that the pressure gradient

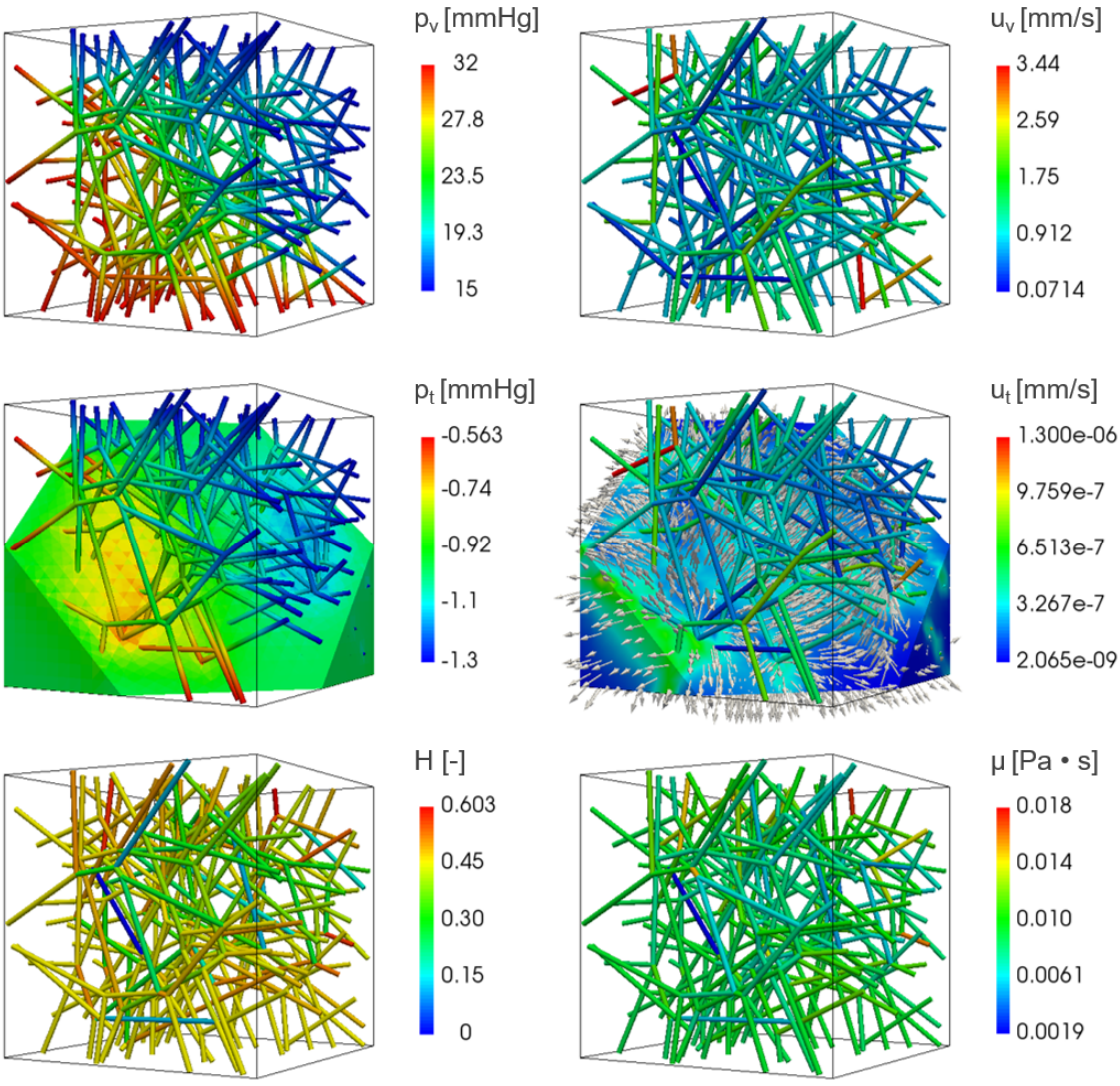

Figure 4.15: Visualization of the flow in a complex network interacting with the interstitial volume. In particular the panels show: the pressure drop along the network (top left); the velocity magnitude (top right); the pressure variation along a slice of the interstitial volume combined with the pressure in the network (middle left); the velocity field along a slice of the interstitial volume (the vectors show the direction and the colors the mangitude) combined with the pressure in the network (middle right); the variations of hematocrit-dependent effective viscosity (bottom left); the discharge hematocrit distribution in the network (bottom right).

in the vasculature induces a secondary, weaker gradient in the interstitium. This effect generates a modest flow in the interstitial volume, which is clearly visible in the middle right panel. On the bottom row of the figure we show the apparent viscosity and the discharge hematocrit. We notice that these two quantities are characterized by a high spatial variability, in line with the fact that they are directly affected by the Fahraeus-Lindqvist and plasma skimming effects, which generate the nonlinearity of the model. In particular, we notice several channels of the vasculature where the viscosity and the hematocrit are particularly low. These are branches where the blood flow is particularly low and the red blood cells hardly penetrate. Indeed, from the bottom right panel we notice that the distribution of hematocrit is shifted towards the bottom of the scale and hematocrit values significantly higher than 45% are hardly reached. This is a consequence of the plasma skimming model.

Chapter 5

Performance analysis of the numerical solver

This chapter is focused on assessing the performance of the new preconditioner for the fluid problem discussed in the previous section. The work is organized as follow. In the first paragraph we compare the different solvers in a simpler case, that is a single rectilinear branch immersed in a 3D cube, where the vessel and the tissue are considered to be uncoupled, which means that they do not interact. The second paragraph instead, concerns the different performances of all the solvers already introduced, but in the case of coupling between vessel and tissue, and on a fairly complex and realistic model of microvascular network. Hence, a different approach consisting of using the preconditioned GMRES inside a Gauss-Seidel iteration. The results are compared to the one obtained from direct solver and all the option for the iterative one. These times only consider the resolution of the fluid problems, which is not the total time necessary to perform the simulations shown below, because the Fahraeus-Lindqvist and plasma skimming effects make the problem become nonlinear. The iterative approach described in Chapter 3 is applied here and the linear system described above is solved once for every iteration.

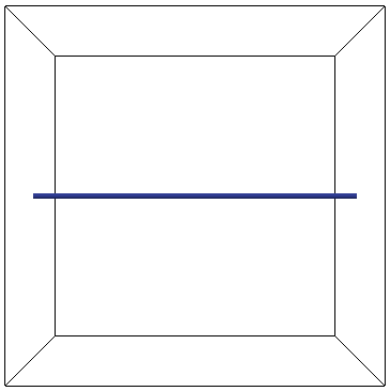

Figure 5.1: Tissue and vessel computational domain for this test-case. The discrete network is made by a single vessel immersed in an unitary cube tissue interstitium, Ω_h. Different discretization steps are used for the tissue, while the vessel remain fixed to 21 points.

5.1 Preconditioned Single-Branch Uncoupled Problem

Let us consider the easiest setting in which we are solving the two problem for vessel and tissue uncoupled. This first test case is used in order to test the quality of the preconditioned described in chapter 3 on the separated problems. The geometry tested is a single rectilinear branch, immersed in a 3D tissue cube, as showed in figure 5.1. Different discretization steps are used for the tissue, while the vessel remains fixed to 21 points.

The parameters used in this case are the same introduced in tables 4.1 and 4.2, for what regard the boundary condition. As before we will enforce Dirichlet boundary conditions for pressure in the vessel, using the arteriolar pressure gradient at the extreme, namely 32 $mmHg$ at the inlet and 28.5 $mmHg$ at the outlet. We are not interested anymore on an interpretation of results, but we will discuss only the performance of the different solution strategies. The problem used to derive the solution for this test is given in system 1.68.

The classification for the solution strategies will be the same one introduced in section 3.3, namely:

- Test A_1: Monolithic SuperLU
- Test B_1: Iterative GMRES, with preconditioner based on a trivial diagonal inversion for the velocity blocks and an Incomplete LU strategy for the Schur complement pressure blocks, for both vessel and tissue problem
- Test C_1: Iterative GMRES with the same preconditioner of test B_1, but where the preconditioned residual Schur complement systems are computed using the algebraic multigrid library SAMG
- Test D_1: Monolithic non-Preconditioned GMRES

The solution in this case will be trivial and known. The tissue pressure will be constant and equal to the far field pressure, -1 $mmHg$. The tissue velocity, thank to the Darcy Law, will be constant and equal to zero. The vessel pressure will be linear decreasing from 32 to 20.5 $mmHg$ along the vessel, while the velocity will be equal to 1 mm/s, derived from the exact solution for the rectilinear case described in the previous chapter.

We can use this case in order to test our preconditioner even if it is trivial, since, as we will see, there will be necessary at least 50 iterations to reach the solution with a residual of 10^{-8}.

In order to complete our setting, we are going to introduce the parameters need to arrest the iterative process: the maximum number of iterations is sets to 15 000 and the residual to 10^{-8}.

In order to show the performance of our iterative process, we compare the solution obtained with all the different methods with discretization step equal to 1/21 for both interstitium and vessel domains. In figure 5.2 we report the interstitium pressure and velocity solutions, on a line of length one, drawn on the plane with y-axis as normal. In figure 5.3, instead, we show the vessel pressure, while in figure 5.4 the vessel velocity. All this results assure us to state that our method is correct, since the solution are equal to the one obtained with the direct SuperLU method.

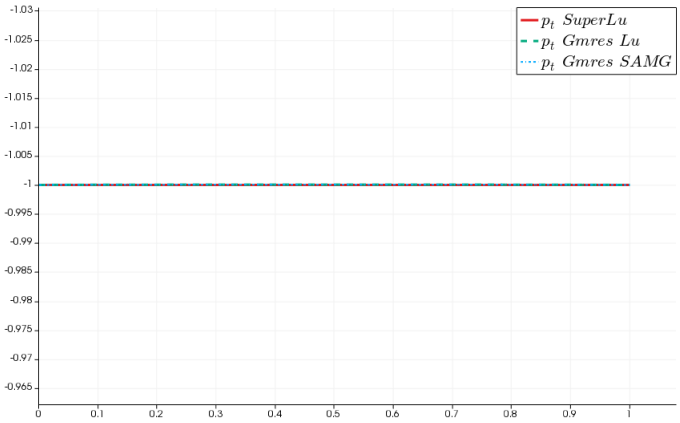

(a)

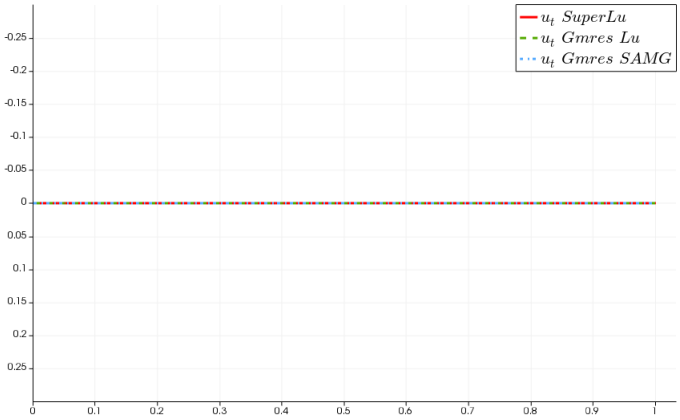

(b)

Figure 5.2: Comparison between tissue pressure (a) and velocity (b) obtained with the different solution strategies. The solution for test D_1 is not reported since the iterative process is not completed, the maximum number of iterations is reached before the residual constraint.

Table 5.1: Degree of freedom for the different meshes with 11,21,25, and 31 discretization on the interstitium domain, while the vessel remains fixed to 21 points.

	11	21	25	31
$dof\ p_t$	7 986	55 566	93 750	178 746
$dof\ u_t$	16 698	113 778	191 250	363 258
$dof\ p_v$	21	21	21	21
$dof\ u_v$	41	41	41	41

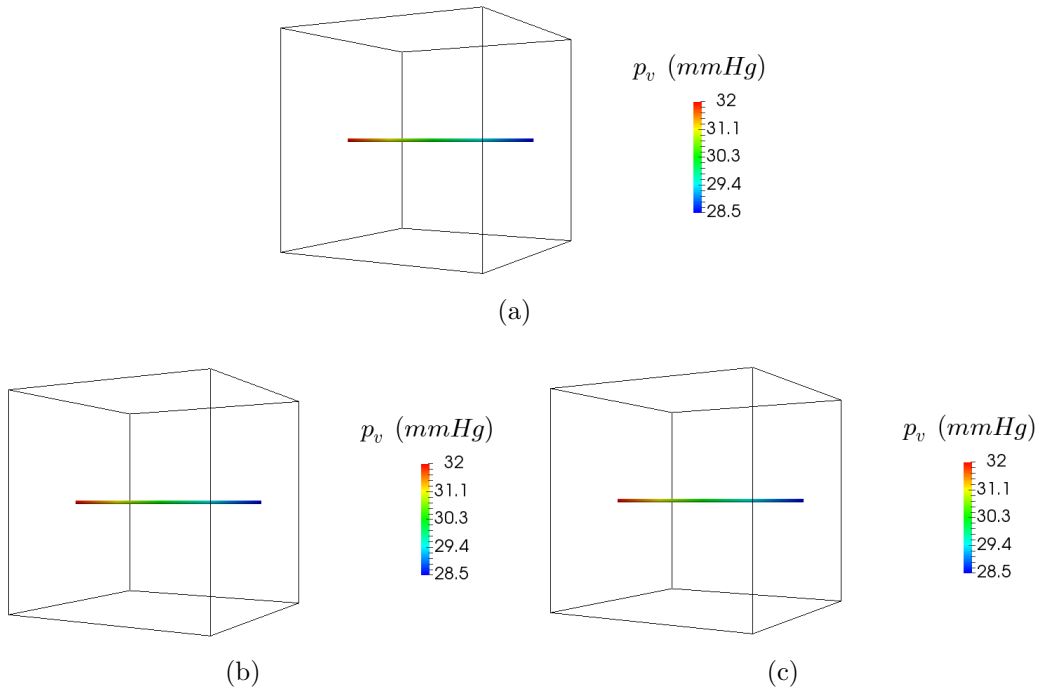

Figure 5.3: Vessel pressure obtained with the different solution strategies: (a) test A_1, (b) test B_1, (c) test C_1. The solution for test D_1 is not reported since the iterative process is not completed, the maximum number of iterations is reached before the residual constraint.

Table 5.2: Number of iteration for Test A_1 SuperLu, Test B_1 Gmres with Incomplete LU, Test C_1 Gmres with SAMG Test D_1 Gmres not preconditioned

	11	21	25	31
A_1	-	-	-	-
B_1	49	50	50	52
C_1	49	50	50	52
D_1	>15 000	>15 000	>15 000	>15 000

Table 5.3: Computation times for Test A_1 SuperLu, Test B_1 Gmres with Incomplete LU, Test C_1 Gmres with SAMG Test D_1 Gmres not preconditioned

	11	21	25	31
A_1	6 s	9,7 min	29,8 min	>30 min
B_1	0,6 s	9,5 s	21,3 s	60 s
C_1	3 s	22 s	42 s	1,6 min
D_1	>60 s	>60 s	>60 s	>60 s

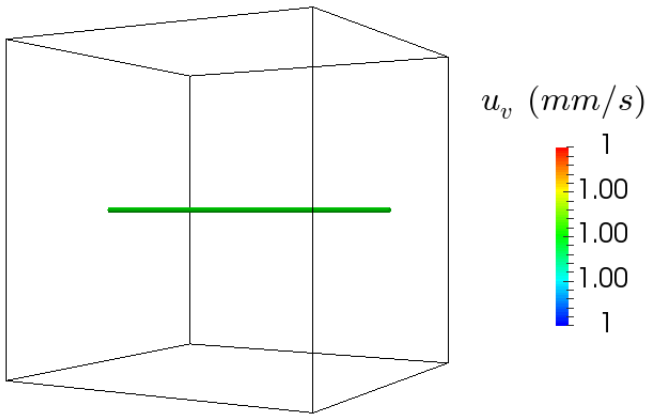

(a)

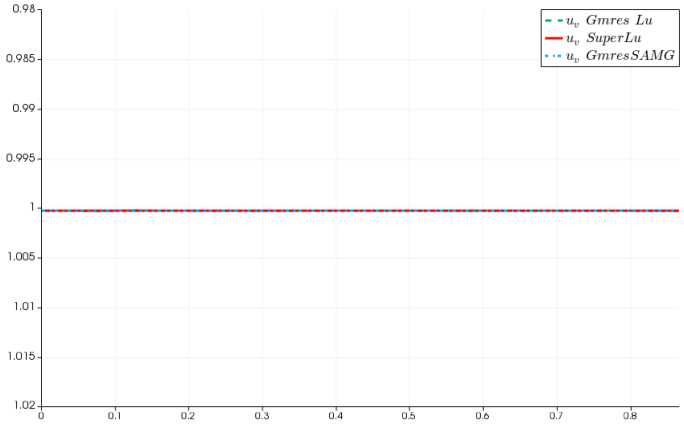

(b)

Figure 5.4: (a) Vessel velocity solution obtained with Monolithic SuperLU approach. (b) Comparison between vessel velocity obtained with the different solution strategies.

We are interested on examine the performance as number of iterations for the GMRES and time for reach the convergence. For this analysis different discretization steps are used for the tissue, namely 1/11, 1/21, 1/25 and 1/31, while the vessel remains fixed to 21 points. This choice brings to the number of degree of freedom for all the different physical unknowns p_v, p_t, u_v, u_t provided in table 5.1. The number of GMRES iterations for tests B_1, C_1 and D_1 are reported in tables 5.2. As we can see, this number remains constant while the number of *dof* increase in tests B_1 and C_1. As consequence, we can state that the preconditioner provided is an optimal preconditioner for this type of problem. In test D_1, that is the non-preconditioned GMRES we reach the maximum number of iterations permitted in this first case.

Let now discuss about the times. The solution are computed on a standard desktop PC. The times results are provided in table 5.3 and the plot is showed in figure 5.5. As we can see, since GMRES non-preconditioned reaches the maximum number of iterations permitted, it is not considered in our graphic. The direct method SuperLU require more time than iterative method both Incomplite LU and multigrid method. Incomplite LU is still faster than SAMG, this may reveal that we didn't reach yet a complexity where multigrid win versus other standard one-level method.

It was not possible to test out preconditioner on a larger tissue grid, due to lack of memory available on a standard PC taken into account.

5.2 Preconditioned Voronoi Coupled Problem

In this section we use the computational preconditioned model described in Chapter 3 to investigate functionality and performance in a fairly complex and realistic model of microvascular network. In this second test case we will solve the coupled problem for both tissue and vessel. Different discretization steps are used for the tissue, while the vessel remains fixed to the same configuration described in the previous sections. The network considered is exactly the one introduced in Chapter 4, as showed in figure 5.7.

The parameters used in this test case are the same introduced in Chapter

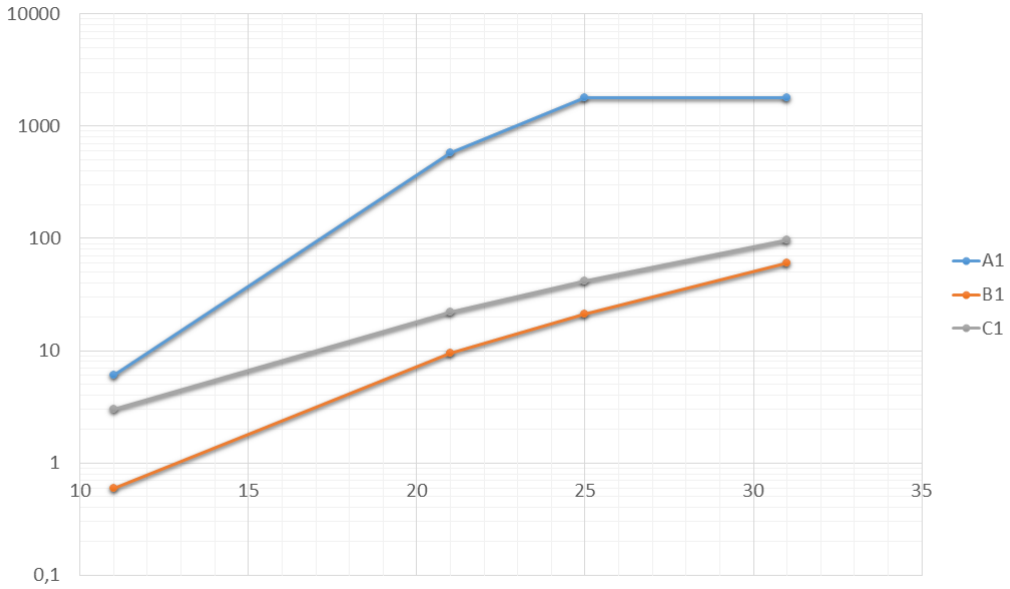

Figure 5.5: Visualization of time performance for the first test case on different interstitium discretization parameter.

4 for the same Voronoi network configuration. Even in this section we are not interested on an interpretation of the result but we evaluate the performance of the new iterative approach describe in section 3.3 for this type of coupled problem, described in 1.68.

The classification for the solution strategies is fully described in table 3.2. The solution of this case are obviously non trivial anymore. In order to complete our setting, we are going to introduce the parameters need to arrest the iterative process: the maximum number of iterations for the Gauss-Seidel external cycle is sets to 5, the maximum number of iterations for the GMRES to 80 000 and the residual to 10^{-8}.

The discretization steps used for the vessel were 1/11, 1/21 and 1/25. The degree of freedom for this second test case are presented in table 5.4. This problem is actually more complex then the previous one in the sens that a grater network configuration ($dof_2 \approx 240\, dof_1$) brings to a considerable loss of sparsity. This

Table 5.4: Degree of freedom for test case on tissue and voronoi network.

	11	21	25
$dof\, p_t$	7 986	55 566	93 750
$dof\, u_t$	16 698	113 778	191 250
$dof\, p_v$	5021	5021	5021
$dof\, u_v$	10291	10291	10291

becomes a problem assembling the system matrix associated, since for greater meshes it fully fits all the memory available. In figure 5.6 we showed the sparsity pattern for matrix $\mathcal{A}$ in the case of single branch configuration (a) uncoupled and (b) coupled, voronoi uncoupled in (c) and voronoi coupled in (d). As we can see considering the same tissue discretization, but changing the vessel has modified substantially the complexity of our problem, doubling the number of non null elements of our system, specially in a coupled problem, where the coupling term are more sparse. In figure 5.6 (e) and (f) we have represented the previous matrices highlighting the correspondence of every block to the notation previously described. The coupling terms $\mathbf{Q}_{tv}$ and $\mathbf{Q}_{vt}$ have become dominant moving on a more complex vessel configuration.
We tried to compute this test on a more powerful computer, with 32 GB memory, but even in this case we was not able to increase the number of discretization more then $31 \times 31 \times 31$ for the tissue.

We report in figure 5.10, 5.11 and 5.12 the tissue pressure and velocity obtained with all the possible solution strategies described. While figure 5.8 and 5.9 contain the solutions obtained for vessel pressure and velocity. All these results allow us to state that our methods are correct, since the solution obtained with the possible iterative strategies are equal to the one obtained with the direct method, test A_2.

The maximum number of external iterations for the Gauss-Seidel cycle is never reached, as we can see from table 5.5 no more then 3 iteration are performed. Comparing the number of iterations of case F_2, that is the GMRES non-preconditioned strategy, with the other cases we observe that our preconditioner drastically reduces this number. Focusing on the iterations for the first Gauss-Seidel iteration, we notice that even increasing the tissue mesh size, the number remains inside a range from 1808 to 2492.

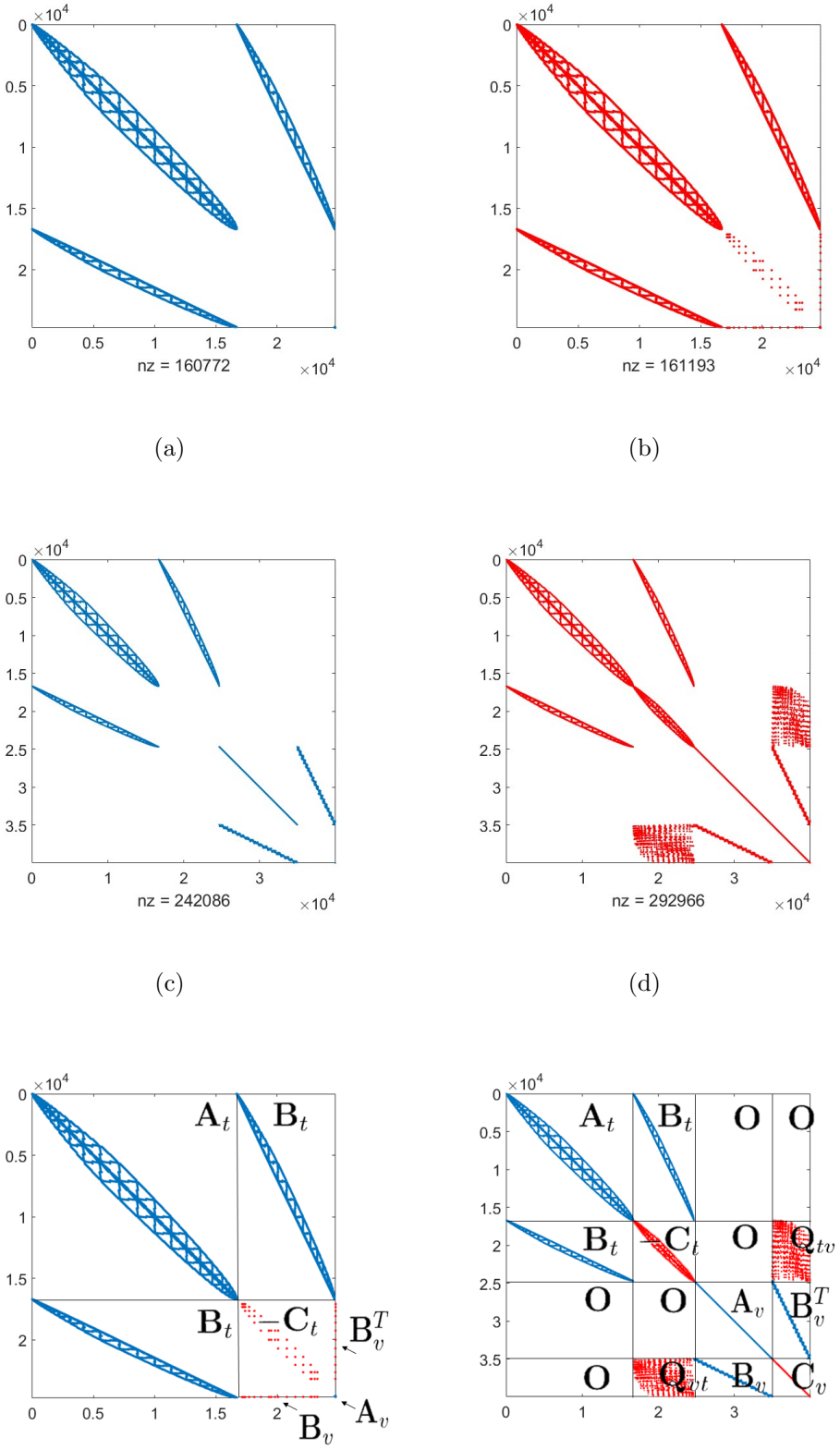

(a) (b)

(c) (d)

(e) (f)

Figure 5.6: Sparsity pattern for matrix $\mathcal{A}$ in the cases: (a) Single branch uncoupled (b) Single branch coupled (c) Voronoi uncoupled (d) Voronoi coupled (e) Single branch blocks visualization (f) Voronoi blocks visualization.

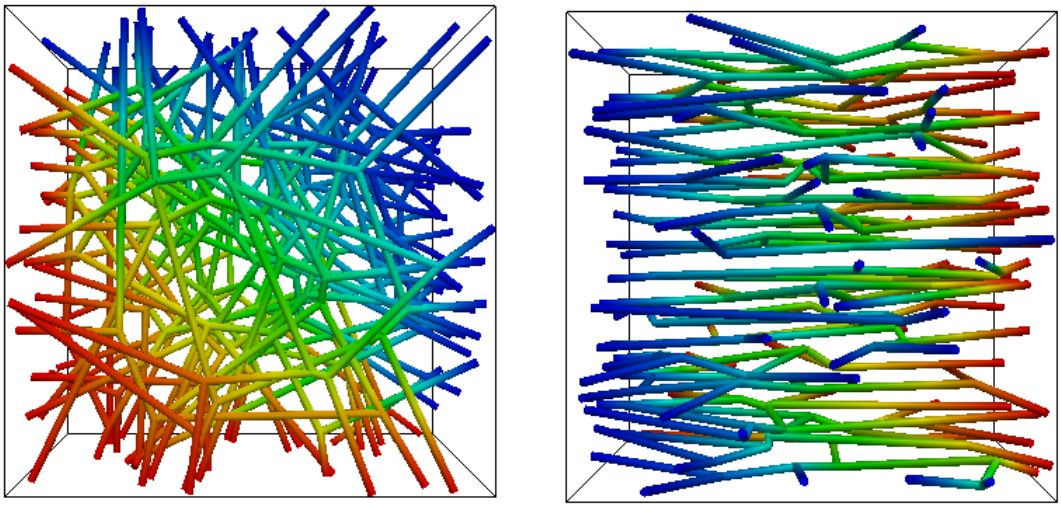

Above view (a) Side view (b)

Figure 5.7: Vessel computational domain for this test-case. The discrete network is immersed in an unitary cube tissue interstitium, Ω_h. Different discretization step are used for the tissue, while the vessel remain fixed to 21 points for every small segment and 251 branches.

In order to describe which of this methods provides the fastest solution we analyze table 5.6 and figure 5.13. In the figure we report the tendency of the total time for every methods, described as sum on all the tissue and vessel Gauss-Seidel iteration. As we can see method D_2 and B_2 are the fastest, while F_2, namely the non-preconditioned GMRES, is the slowest one. SuperLu even if is faster on coarser mesh, becomes slower than D_2, B_2 and E_2 on the finest mesh, while is still faster then C_2 and F_2.

For the moment SAMG is not the best solution for our preconditioner, hence for reach the number of *dof* where multigrid wins we need to increase the number of tissue discretization, but this is impossible due to the loss of memory, as already discuss.

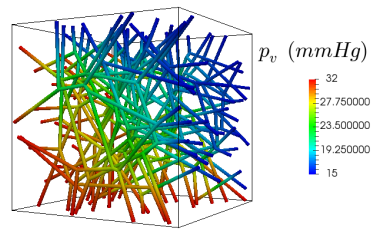

(a) Test A_2

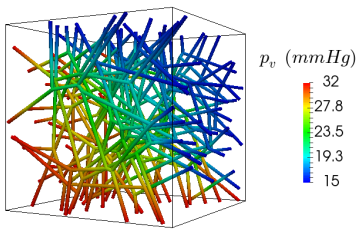

(b) Test B_2

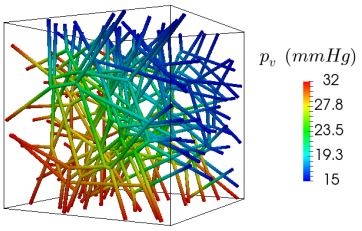

(c) Test C_2

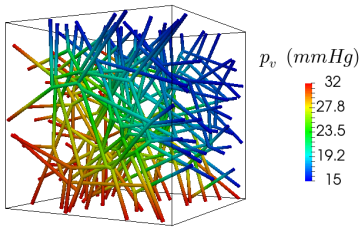

(d) Test D_2

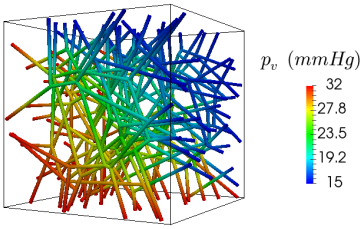

(e) Test E_2

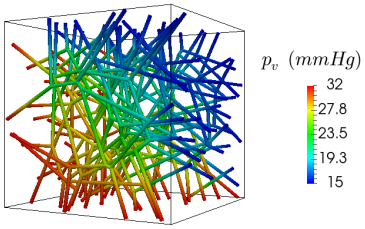

(f) Test F_2

Figure 5.8: Comparison between the vessel pressure using different resolution methods.

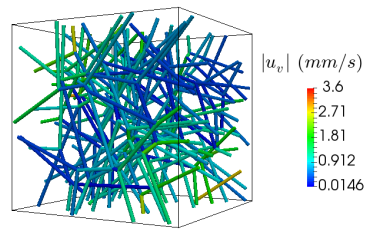

(a) Test A_2

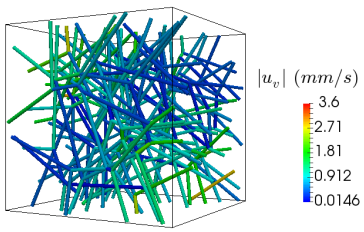

(b) Test B_2

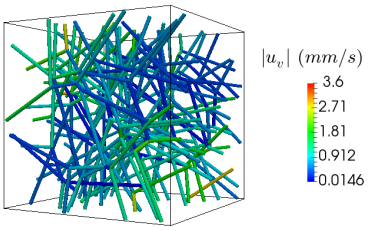

(c) Test C_2

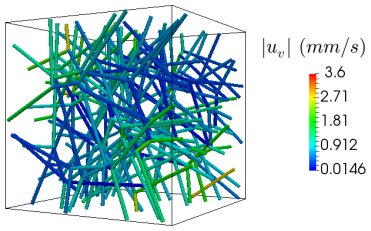

(d) Test D_2

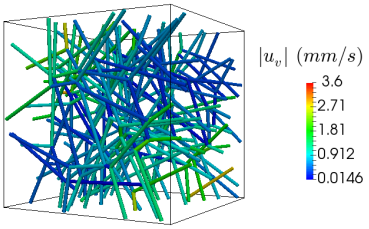

(e) Test E_2

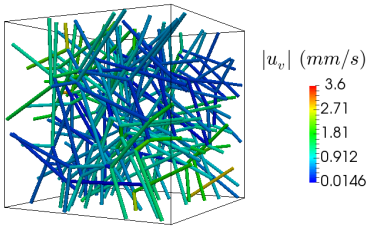

(f) Test F_2

Figure 5.9: Comparison between the vessel velocity using different resolution methods.

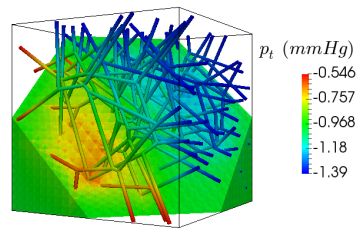

(a) Test A_2

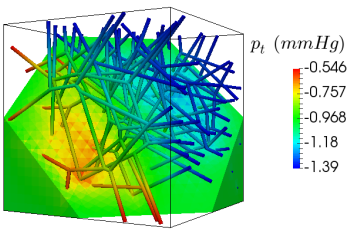

(b) Test B_2

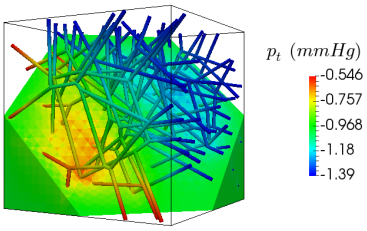

(c) Test C_2

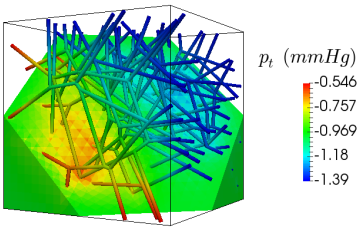

(d) Test D_2

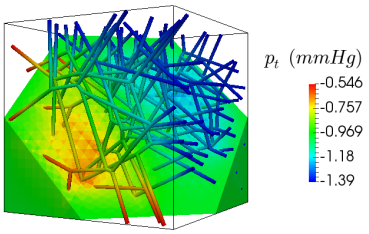

(e) Test E_2

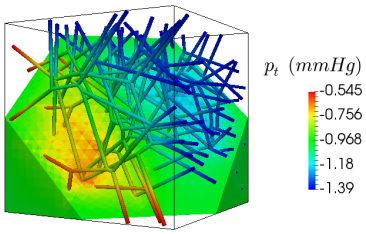

(f) Test F_2

Figure 5.10: Comparison between tissue pressure using different resolution methods.

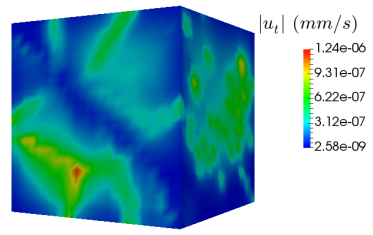

(a) Test A_2

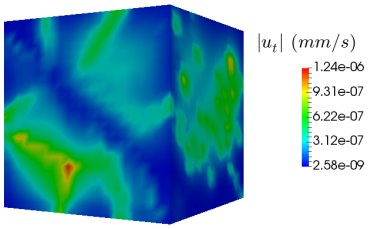

(b) Test B_2

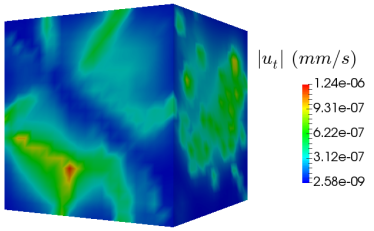

(c) Test C_2

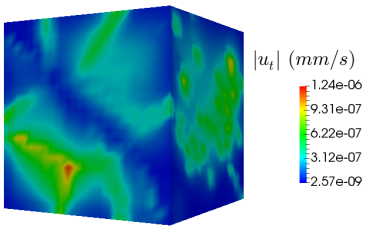

(d) Test D_2

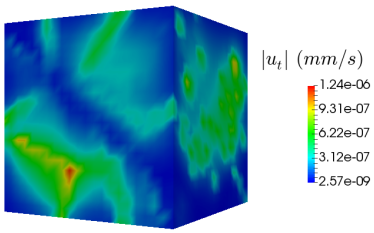

(e) Test E_2

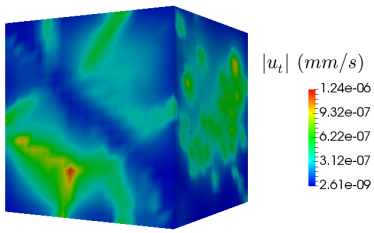

(f) Test F_2

Figure 5.11: Comparison between tissue velocity using different resolution methods.

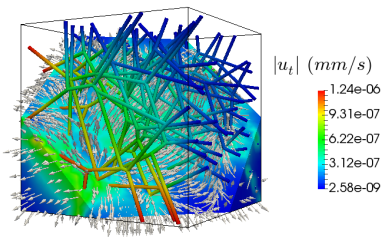

(a) Test A_2

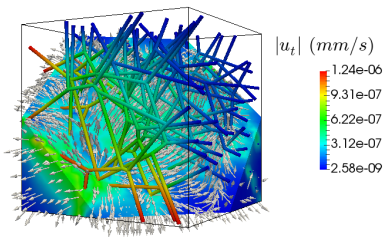

(b) Test B_2

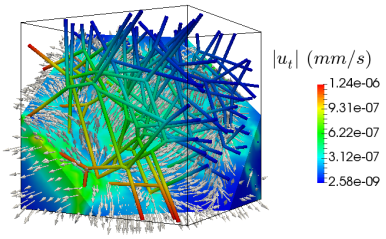

(c) Test C_2

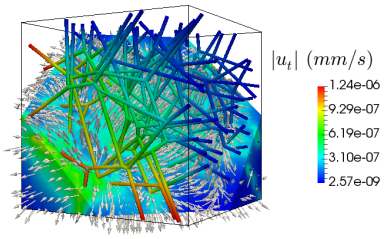

(d) Test D_2

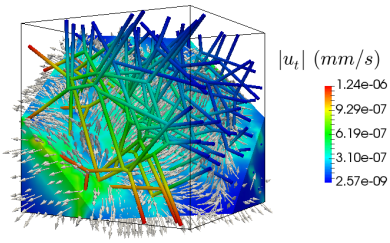

(e) Test E_2

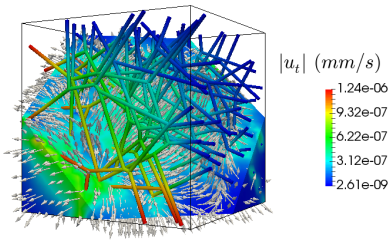

(f) Test F_2

Figure 5.12: Comparison between tissue velocity using different resolution methods.

Table 5.5: Number of iterations for different test cases.

		11			21			25		
		I	II	III	I	II	III	I	II	III
B_2	$iter_v$	-	-	-	-	-	-	-	-	-
	$iter_t$	1 842	598	2	1 878	567	1	2 216	628	1
C_2	$iter_v$	-	-	-	-	-	-	-	-	-
	$iter_t$	1 843	594	1	1 808	544	2	2 492	694	1
D_2	$iter_v$	509	-	-	509	-	-	509	-	-
	$iter_t$	1866	-	-	2 093	-	-	2 381	-	-
E_2	$iter_v$	509	-	-	509	-	-	509	-	-
	$iter_t$	1867	-	-	2 192	-	-	1 843	1	-
F_2	$iter_v$	-	-	-	-	-	-	-	-	-
	$iter_t$	14 587	44	-	50 437	86	-	70 386	137	-

Table 5.6: Computation times for different test cases.

		11			21			25		
		I	II	III	I	II	III	I	II	III
A_2	$time_{vt}$	6,5 s	-	-	11,3 min	-	-	30 min	-	-
B_2	$time_v$	0,08 s	0,08 s	0,08 s	0,08 s	0,09 s	0,09	0,1 s	0,09 s	0,09 s
	$time_t$	25 s	8 s	0,06 s	5,8 min	1,7 min	0,7 s	15 min	4,5 min	1,5 s
C_2	$time_v$	0,08 s	0,16 s	0,19 s	0,09 s	0,12 s	0,19 s	0,09 s	0,15 s	0,17 s
	$time_t$	90 s	29 s	0,19 s	12,4 min	3,7 min	1,8 s	32,7 min	9,2 min	3 s
D_2	$time_v$	1,43 s	-	-	1,49 s	-	-	1,5 s	-	-
	$time_t$	25 s	-	-	6,5 min	-	-	16 min	-	-
E_2	$time_v$	15 s	-	-	15 s	-	-	15 s	0,09 s	-
	$time_t$	90 s	-	-	15,8 min	-	-	24 min	0,3 s	-
F_2	$time_v$	0,08 s	0,08 s	-	0,09 s	0,08 s	-	0,1 s	0,1 s	-
	$time_t$	64 s	0,2 s	-	26,7 min	26 s	-	2,36 h	16 s	-

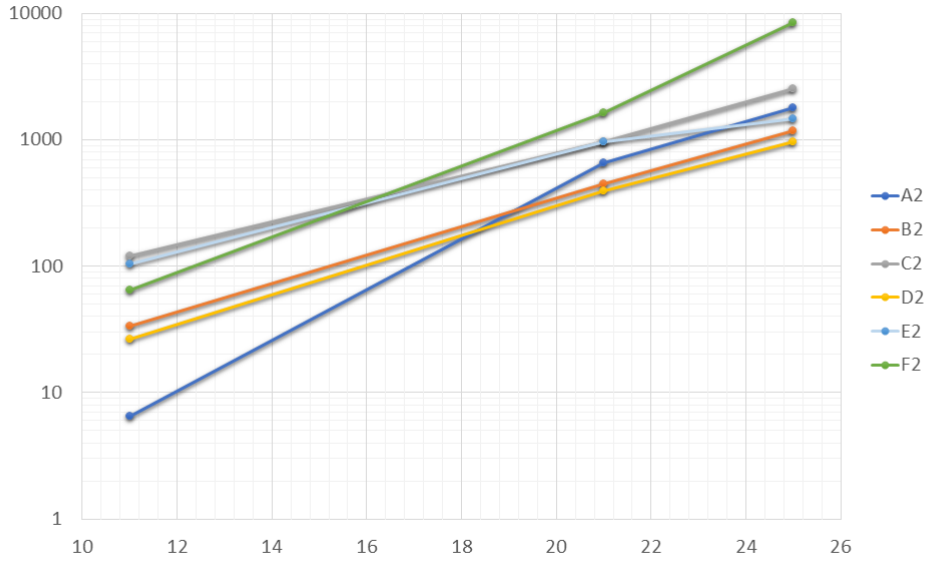

Figure 5.13: Visualization of time performance for the second test case on different interstitium discretization parameter.

5.3 Matrix Level Coarsening SAMG

As conclusion of our work we present the 4-level coarsening matrices arising from the application of an AMG algorith to the tissue Schur complement discretization, figure 5.14.

This matrices came from the Voronoi coupled problem of test case 2, with a discretization parameter of 1/11 for the tissue. They represent the four level coarsening of a V-cycle used to compute the residual system for the tissue pressure of test C_2. As we can see going deeper in coarsening we loose the diagonal shape and we reduce incredibly the size of our system, obtaining less sparse matrices. Going from level 1 to 2 the number became a quarter and even less on the other levels, until we reach the smallest size on level 4, where the system can be computed with a direct method.

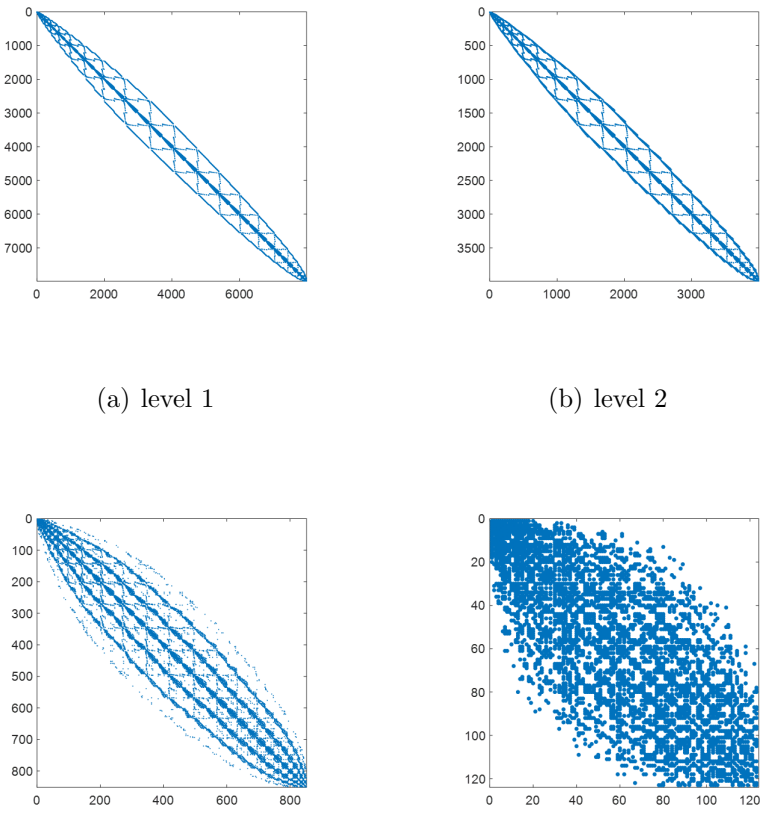

(a) level 1

(b) level 2

(c) level 3

(d) level 4

Figure 5.14: 4-level coarsening matrices arising from the application of an AMG algorith to the tissue Schur complement discretization

Conclusion

In this work we have consolidated an already existed two phase model for microcirculation from both modeling and numerical point of view. In particular we have developed a new iterative solver. A validation for both subjects has been made. For the validation of the new numerical solver we first restrict our problem on the 3D tissue domain and we have compared the results with an exact solution on a given non trivial source term. Later on, we discussed the comparison of the solution obtained from our solver with the one from the extensively verified SuperLU direct method.
After this first validation, we have moved to more complex simulations. Single Branch with possible curve configuration are studied in both Chapter 4 and 5. This test case was used to visualize the trend for pressure, velocity and hematocrit. As we saw, switching on the capillary permeability, we allow for plasma leakage from the capillary to the interstitial tissue. Therefore the flow and hematocrit profiles change in both vessel and tissue. We showed that the hematocrit variation is inverse to the velocity one and the viscosity is not constant anymore, due to the changes in hematocrit.
In addition, Y-Shape bifurcations were explored in Chapter 4, in order to visualize the Plasma skimming and Fahraeus-Lindqvist effects. As expected red blood cells hardly flow into the daughter branch with smaller radius. The behavior of viscosity is less apparent, but still in line with the model. All these considerations suggest that the interaction between radius, flow rate, hematocrit and viscosity is highly nonlinear and hardly predictable with simple models that do not take into account their combined effects. Finally, we apply the same considerations on a more complex geometry, that simulates a real capillary network at the end of Chapter 4.

After this first modeling considerations we move our attention to the construction of the Schur complement preconditioner for the GMRES iterative

method. We derive two different discretization of the Schur complement for tissue and vessel, since it strongly depends from the finite element space chosen. For the tissue Schur complement the discretization is a standard $P1$ Laplacian weak formulation, while for the tissue we introduced a special $P0$ Laplacian discretization. Both have been considered with the respective boundary conditions.

After the theoretical derivation of these preconditioners we have explored the performance in Chapter 5. A first simple approach was studied for an uncoupled single branch configuration. The results in time and iterations allow us to state that the preconditioner provided is an optimal preconditioner for this type of problem. Incomplete LU is still faster than SAMG, but both are performing better that the previous direct SuperLU method.

In the second part of Chapter 5, we move on a more realistic scenario, a coupled network voronoi problem. As we see from the matrices showed in Chapter 5, maintaining the same number of discretization in the tissue but moving from a single branch to a voronoi configuration, it increases drastically the computational cost of the problem. This is due to the presence of extra diagonal coupling and junction terms in the vessel problem. The tests effectuated for this problem show again that we constructed a good preconditioner. The solution obtained with SuperLU or GMRES/ILU for the vessel problem combined with an ILU factorization for the tissue are the fastest, while the GMRES non preconditioned is the slowest. For the moment SAMG is not the best solution for our preconditioner. This means that we did not reach an enough high complexity, where multigrid wins versus other standard one-level method.

As future perfective we will first try to improve the SAMG performance. Second we can combine this complex fluid model with the mass transport. This application is very interesting because it enables to apply the computational model to study drug delivery to organs.

Appendix A

AMG_interface and Darcy_preconditioner classes

We develop a C++ code, modifying an already existed code, wrote by Notaro [18] and Di Gregorio [10], using GetFEM++5.0, an open-source finite element library. The scheme of the features added is presented in figure A.1. The red parts represent the new section added. They basically consist in a first *Darcy_precoditioner* class which call a second *AMG_interface* class. Of the first one there exist three different versions: one for the only vessel, one for the only tissue and the last one for a coupled tissue-vessel monolithic preconditioner. The file problem3d1d has been modified with the new version of the GMRES implementation.

AMG_interface We now report the most important features of the class *AMG_interface*. It contains two main subroutines, one for converting the sparse matrix type in the special one require from SAMG and the second one to define all the special parameter to call the SAMG library. The both are reported below.

Listing A.1: Subroutines definition

```
1 // ========= generation af matrix
2 void convert_matrix(gmm::csr_matrix<scalar_type> A_csr);
3 // ========= solver of the class ======================
4 void solve(gmm::csr_matrix<scalar_type> A_csr,
5   std::vector<scalar_type> U, std::vector<scalar_type> B,
6   int solver_type );
```

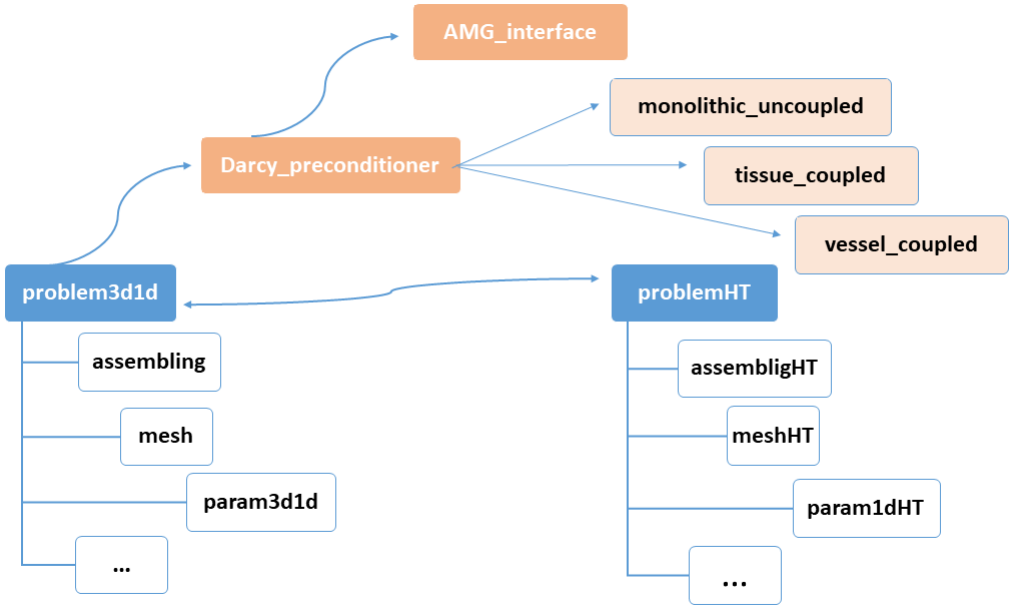

Figure A.1

Listing A.2: Convert_matrix

```
1  void AMG::convert_matrix(gmm::csr_matrix<scalar_type> A_csr)
2  {
3    std::cout<<" AMG::convert_matrix::Start building the matrix"<<std::endl;
4    std::cout<<"*** parameters SAMG matrix    "<<A_csr.nrows()<<std::endl;
5    std::cout<<"*** parameters SAMG matrix    "<<A_csr.ncols()<<std::endl;
6    nnu_=A_csr.nc; nna_=A_csr.pr.size();
7    a_samg_=new double[nna_];
8    ja_samg_=new APPL_INT[nna_];
9    ia_samg_=new APPL_INT[nnu_+1];
10   ia_samg_[0]=1;
11   unsigned int offset=0;
12   for(int ia=0;ia<nnu_+1-1;ia++){
13     unsigned int nonzero=A_csr.jc.at(ia+1)-A_csr.jc.at(ia);
14     ia_samg_[ia+1] = nonzero + ia_samg_[ia] ;
15     bool diag=true;
16     for (int innz=offset; innz<offset+nonzero; innz++ ){
17         if( ia == (int) A_csr.ir.at(innz))
18       {  //WARNING: not working for a matrix with zero on the diagonal
19          //  std::cout<<"diagonal term"<<std::endl;
20        if(fabs(A_csr.pr.at(innz))<1E-30)std::cout<<"***
21                        **diagonal zero"<<std::endl;
```

```
22          a_samg_[offset]=A_csr.pr.at(innz);
23          ja_samg_[offset]=A_csr.ir.at(innz)+1;
24          diag=false;
25        }
26    }
27      if (diag) {
28       std::cout<<"dsufhasdjkasdfasdf jhasdfasdfjkasdffasdfjkl"<<std::endl;
29       ia_samg_[ia+1] +=1;
30       a_samg_[offset]=1.0;
31       ja_samg_[offset]=ia_samg_[ia];
32    }
33    int shift=1;
34    for (int innz=offset; innz<offset+nonzero; innz++ )
35      if( ia != (int) A_csr.ir.at(innz))
36       {
37       if(fabs(A_csr.pr.at(innz))<1E-30) std::cout<<"**non diagonal zero"
38          <<A_csr.pr.at(innz)<<std::endl;
39       a_samg_[offset+shift]=A_csr.pr.at(innz);
40       ja_samg_[offset+shift]=A_csr.ir.at(innz)+1;
41       shift++;
42     }
43    //std::cout<<std::endl;
44    // std::cout<<"non zero in i "<<ia<<" are "<< nonzero<<std::endl;
45    offset+=nonzero;
46  }
47  std::cout<<" AMG::convert_matrix:: end matrix conversion "<< std::endl;
48  return;
49 }
```

The true call to the SAMG library is effectuated inside the solve subroutine as follows:

Listing A.3: Call to SAMG library

```
1       SAMG(&nnu_,&nna_,&nsys,&ia_samg_[0],&ja_samg_[0],
2       &a_samg_[0],
3       &B.front(), &U.front(),
4       //&b_samg[0], &u_samg[0],
5       &iu[0],&ndiu,
6       &ip[0],&ndip,&matrix,&iscale[0],
7       &res_in,&res_out,&ncyc_done,&ierr,
```

```
8       &nsolve,&ifirst,&eps,&ncyc,&iswtch,
9       &a_cmplx,&g_cmplx,&p_cmplx,&w_avrge,
10      &chktol,&idump,&iout);
```

We now consider separately the definition of all the parameter needed in the SAMG call, highlighting the most important one. For more detail we refer to the guide [11] for SAMG.

- `nnu`: number of variable. It is the number of solution components ui of the linear system Au=f to be solved. Variables are numbered as 1,2,...,nnu.
- `a`: the non-zero entries of the i-th row (1< i< nnu) are stored in a(j)
- `nna`: denotes the total number of matrix entries stored
- `nsys`: number of unknown variable. In our case it will be considered a variable approach, therefore nsys will be always consider equal to 1. The unknowns are numbered 1,2,...,nsys.
- `ia`: The entries of the matrix A, denoted by A(i,j). They are assumed to be stored in compressed row format (compressed row storage, CSR) in a vector a, row by row, each row starting with its diagonal element. While all diagonal entries have to be stored independent of whether or not they are zero, the off-diagonal entries need to be stored only if they are non-zero. Since the order in which the off-diagonal entries are stored in a is arbitrary, two integer pointer vectors ia and ja are required to identify each element in a.
- `ja`: this pointer is defined so that `ja`(j) (1<j<nna) equals the original matrix column index of a(j), this means that `a`(j) corresponds to the variable u(`ja`(j)). In particular, since `a`(`ja`(i)) contains the diagonal entry of row i, we have `ja`(`ia`(i))=i.
- `iu`: SAMG requires some additional information on the system, namely, the correspondence between variables and unknowns. This information has to be provided via an integer variable-to-unknown pointer vector `iu`.
- `eps`: The residual is fixed to 1.0e-12.

- `a_cmplx` = 2.2; `g_cmplx` = 1.7; `w_avrge` = 2.4; `p_cmplx` = 0.0; They are used to estimated dimensioning.

- `idump`: It controls the matrix dumping of SAMG, the options are: 1 Standard print output, no matrix dump; 2-6 Write matrices to disk: level 2 up to level `idump`; 7 Write matrices to disk: level 2 up to the coarsest level; 8 Write finest-level matrix to disk (incl. right hand side etc.); 9 Write all matrices to disk.

Darcy_precoditioner In order to use the SAMG library we need to include it inside our preconditioner class, namely:

Listing A.4: AMG_Interface inlusion

```
1 #include "AMG_Interface.hpp"
```

We report here an example of a *darcy_preconditioner* constructor for the case of the only tissue problem. To notice how the boundary conditions have to change in case of Dirichlet or Neumann type.

Listing A.5: Darcy_precond_tissue_coup

```
1  template <class MATRIX>
2  darcy_precond_tissue_coup<MATRIX>::darcy_precond_tissue_coup(
3    const MATRIX &A,
4    const MATRIX &Btt,
5    const getfem::mesh_fem mf_p,
6    const getfem::mesh_im mim)
7    : A_(A)
8    , pA_(A) ,Ct_(Btt)
9  #ifdef USE_SAMG
10   , amg_("Schur")
11 #endif
12 {
13     const getfem::size_type nb_dof_p = mf_p.nb_dof();
14     const getfem::mesh &mesh = mf_p.linked_mesh();
15     getfem::mesh_region inner_faces =
16               getfem::inner_faces_of_mesh(mesh);
```

```
17      getfem::mesh_region outer_faces;
18      getfem::outer_faces_of_mesh(mesh, outer_faces);
19      getfem::ga_workspace wp;
20
21      std::vector<double> p(nb_dof_p);
22      wp.add_fem_variable("p", mf_p, gmm::sub_interval(
23                                              0, nb_dof_p), p);
24
25      #ifdef USE_MP
26      wp.add_expression("p*Test_p",mim);
27      #else
28      wp.add_expression("Grad_p.Grad_Test_p", mim);
29      wp.add_expression("-0.5 * (Grad_p +
30            Interpolate(Grad_p, neighbour_elt)).Normal"
31          " * (Test_p - Interpolate(Test_p, neighbour_elt))"
32          "-0.5 * (Grad_Test_p +
33              Interpolate(Grad_Test_p, neighbour_elt)).Normal"
34          " * (p - Interpolate(p, neighbour_elt))"
35          "+2 / element_size * (p - Interpolate(p, neighbour_elt))"
36          " * (Test_p - Interpolate(Test_p, neighbour_elt))",
37          mim, inner_faces);
38      //to comment in case of mix/neumann conditions, for DIR type
39      //wp.add_expression("1/element_size*p*Test_p", mim, outer_faces);
40
41      wp.add_expression("0.01*p*Test_p", mim, outer_faces);
42
43      #endif
44      wp.assembly(2);
45
46      gmm::copy(wp.assembled_matrix(), S_);
47
48      #ifdef USE_SAMG
49      amg_.convert_matrix(S_);
50      #else
```

```
51        slu_.build_with(S_);
52        #endif
53  }
```

Bibliography

[1] D. M. Audet and W. L. Olbricht. The motion of model cells at capillary bifurcations. *Microvascular Research*, 33(3):377–396, 1987.

[2] Jared O. Barber, Jonathan P. Alberding, Juan M. Restrepo, and Timothy W. Secomb. Simulated two-dimensional red blood cell motion, deformation, and partitioning in microvessel bifurcations. *Annals of Biomedical Engineering*, 36(10):1690–1698, 2008.

[3] Michele Benzi, Gene H. Golub, and Jörg Liesen. Numerical solution of saddle point problems. *Acta Numer.*, 14:1–137, 2005.

[4] Franco Brezzi and Michel Fortin. *Mixed and hybrid finite element methods*, volume 15 of *Springer Series in Computational Mathematics*. Springer-Verlag, New York, 1991.

[5] William L. Briggs, Van Emden Henson, and Steve F. McCormick. *A multigrid tutorial*. Society for Industrial and Applied Mathematics (SIAM), Philadelphia, PA, second edition, 2000.

[6] William L. Briggs, Van Emden Henson, and Steve F. McCormick. *A multigrid tutorial*. Society for Industrial and Applied Mathematics (SIAM), Philadelphia, PA, second edition, 2000.

[7] Russell T Carr and Jewen Xiao. Plasma Skimming in Vascular Trees: Numerical Estimates of Symmetry Recovery Lengths. *Microcirculation*, 2(4):345–353, jan 1995.

[8] L. Cattaneo and P. Zunino. A computational model of drug delivery through microcirculation to compare different tumor treatments. *International Journal for Numerical Methods in Biomedical Engineering*, 30(11):1347–1371, 2014.

[9] L. Cattaneo and P. Zunino. Computational models for fluid exchange between microcirculation and tissue interstitium. *Networks and Heterogeneous Media*, 9(1):135–159, 2014.

[10] Simone Di Gregorio, Maria Laura Costantino, Luca Possenti, Giustina Casagrande, and Paolo Zunino. Modello matematico e numerico della fluidodinamica e del trasporto di eritrociti nella microcircolazione, 2017.

[11] Fraunhofer Institute for Algorithms and Scientific Computing (SCAI). Samg user's manual. samg release 26a1 serial and openmp parallel, 2017.

[12] Alan Gibbons. *Algorithmic graph theory*. Cambridge University Press, Cambridge, 1985.

[13] Sven Gross and Arnold Reusken. *Numerical methods for two-phase incompressible flows*, volume 40 of *Springer Series in Computational Mathematics*. Springer-Verlag, Berlin, 2011.

[14] Arthur C. Guyton and John E Hall. *Guyton and Hall Textbook of Medical Physiology 13th edition*. Number 1. Philadelphia, 13th edition, 2015.

[15] John M. Higgins, David T. Eddington, Sangeeta N. Bhatia, and L. Mahadevan. Statistical dynamics of flowing red blood cells by morphological image processing. *PLoS Computational Biology*, 5(2), 2009.

[16] J R Levick. Capillary filtration-absorption balance reconsidered in light of dynamic extravascular factors. *Experimental physiology*, 76:825–857, 1991.

[17] B J Mcguire and T W Secomb. Based on Maximal Oxygen Consumption Rates. 5051:2382–2391, 2003.

[18] Domenico Notaro, Laura Cattaneo, Luca Formaggia, Anna Scotti, and Paolo Zunino. A mixed finite element method for modeling the fluid exchange between microcirculation and tissue interstitium. Cham, 2016.

[19] Domenico Notaro, Laura Cattaneo, Luca Formaggia, Anna Scotti, and Paolo Zunino. A mixed finite element method for modeling the fluid exchange between microcirculation and tissue interstitium. In Giulio Ventura and Elena

Benvenuti, editors, *Advances in Discretization Methods: Discontinuities, Virtual Elements, Fictitious Domain Methods*, pages 3–25. Springer International Publishing, Cham, 2016.

[20] Nicola Parolini. Course notes, computational fluid dynamics.

[21] CS Charles S. Peskin. The immersed boundary method. *Acta Numerica*, 11(January 2002):479–517, 2002.

[22] D. Pinho, R. Lima, A. I. Pereira, and F. Gayubo. Tracking Red Blood Cells in Microchannels: A Comparative Study Between an Automatic and a Manual Method. pages 165–180. 2013.

[23] Catherine Elizabeth Powell and David Silvester. Optimal preconditioning for Raviart-Thomas mixed formulation of second-order elliptic problems. *SIAM J. Matrix Anal. Appl.*, 25(3):718–738, 2003.

[24] A R Pries and T W Secomb. Microvascular blood viscosity in vivo and the endothelial surface layer. *American journal of physiology. Heart and circulatory physiology*, 289(6):H2657–H2664, 2005.

[25] A R Pries, T W Secomb, T. Gessner, M B Sperandio, J F Gross, and P Gaehtgens. Resistance to blood flow in microvessels in vivo. *Circulation Research*, 75(5):904–915, nov 1994.

[26] A.R. Pries and T.W. Secomb. Microvascular blood viscosity in vivo and the endothelial surface layer. *American Journal of Physiology - Heart and Circulatory Physiology*, 289(6 58-6):H2657–H2664, 2005.

[27] Alfio Quarteroni. *Numerical models for differential problems*, volume 8 of *MS&A. Modeling, Simulation and Applications*. Springer, Milan, second edition, 2014. Translated from the fifth (2012) Italian edition by Silvia Quarteroni.

[28] Alfio Quarteroni and Alberto Valli. *Numerical approximation of partial differential equations*, volume 23 of *Springer Series in Computational Mathematics*. Springer-Verlag, Berlin, 1994.

[29] B. V. Rathish Kumar, Alfio Quateroni, Luca Formaggia, and Daniele Lamponi. On parallel computation of blood flow in human arterial network based on 1-D modelling. *Computing*, 71(4):321–351, 2003.

[30] Navid Safaeian and Tim David. A computational model of oxygen transport in the cerebrocapillary levels for normal and pathologic brain function. *Journal of cerebral blood flow and metabolism : official journal of the International Society of Cerebral Blood Flow and Metabolism*, 33(November 2012):1–9, 2013.

[31] Navid Safaeian, Mathieu Sellier, and Tim David. A computational model of hemodynamic parameters in cortical capillary networks. *Journal of Theoretical Biology*, 271(1):145–156, 2011.

[32] DU Silverthorn. *Human Physiology*. 2010.

[33] Klaus Stüben. Algebraic multigrid. an introduction with applications, german national research center for information technology (gmd), institute for algorithms and scientific computing (scai), 1999.

[34] Klaus Stüben. Algebraic multigrid (AMG): experiences and comparisons. *Appl. Math. Comput.*, 13(3-4):419–451, 1983.

[35] Klaus Stüben and Ulrich Trottenberg. Multigrid methods: fundamental algorithms, model problem analysis and applications. In *Multigrid methods (Cologne, 1981)*, volume 960 of *Lecture Notes in Math.*, pages 1–176. Springer, Berlin-New York, 1982.

[36] Melody A. Swartz and Mark E. Fleury. Interstitial Flow and Its Effects in Soft Tissues. *Annual Review of Biomedical Engineering*, 9(1):229–256, 2007.

[37] Michael Welter and Heiko Rieger. Interstitial Fluid Flow and Drug Delivery in Vascularized Tumors: A Computational Model. *PLoS ONE*, 8(8), 2013.